SCANNING TUNNELING MICROSCOPY AND SPECTROSCOPY STUDIES OF GRAPHENE

BY ADINA LUICAN-MAYER

A dissertation submitted to the
Graduate School—New Brunswick
Rutgers, The State University of New Jersey
in partial fulfillment of the requirements
for the degree of
Doctor of Philosophy
Graduate Program in Physics

Written under the direction of
Prof. Eva Y. Andrei
and approved by

_____

_____

_____

_____

New Brunswick, New Jersey

October, 2012

ABSTRACT OF THE DISSERTATION

Scanning Tunneling Microscopy and Spectroscopy studies of graphene

by Adina Luican-Mayer

Dissertation Director: Prof. Eva Y. Andrei

In the two-dimensional (2D) lattice of graphene, consisting of carbon atoms arranged in a honeycomb lattice, the charge carriers are described by a Dirac-Weyl Hamiltonian. Seeking to understand their unique nature, this thesis presents results of scanning tunneling microscopy (STM) and spectroscopy (STS) experiments at low temperatures and in magnetic field. These techniques give access, down to atomic scales, to structural information as well as to the electronic properties of graphene.

The main findings include the observation of quantized Landau levels (LL) in the presence of magnetic field, their dependence on carrier density and effects of charged impurities and other disorder on the LL spectrum.

Twisting graphene layers away from the equilibrium Bernal stacking leads to the formation of Moiré patterns that significantly alter the electronic properties of graphene stacks. The second part of the thesis discusses the effects of such rotations on the electronic properties as a function of twist angle.

Acknowledgements

I would like express my gratitude to my adviser Eva Andrei from which I have learned a lot during the graduate school years and to which I look up as a role model. Her enthusiasm and passion for Physics always made our discussions motivating and uplifting.

I would like to thank the postdocs in our group from which I have learned a great deal. Guohong Li and I worked together on many of the projects and I am grateful for all the discussions we had and for his "tough love". In the beginning of my PhD I am very lucky to have had Xu Du as a mentor for using the cleanroom and for fabricating graphene devices. I am thankful to Ivan Skachko for always offering a helping hand around the lab and for always being up for discussing a physics problem. I am thankful to our theory collaborator, Maxim Kharitonov, for taking the time to stop by the lab and discuss our data . Without the other graduate and undergraduate students: Chih-Pin, Fabian, Alem, Manuel, Justin, the atmosphere in the lab would certainly be less entertaining and enthusiastic.

Through fun trips and long lunch discussions my friends from Rutgers made the last 6 years a lot of fun. Chuck, John, Chioun, Senia, Sinisa, Deepak, Darakshan, Kshitij, Rebecca, Lucia, Marietta, thank you all for being great friends.

I would like to thank my husband, Daniel, for his infinite patience and support during long hours in the lab. I am indebted to my parents which have always been a phone call away for giving me advice and support and have always encouraged me to pursue the things that make me happy.

Dedication

To my family

Table of Contents

List of Figures

Chapter 1
Introduction

1.1 Introduction

Discovery of new materials has always resulted in advances in both our understanding of the physical world and in practical technological developments. This was the case of superconductors, magnetic materials, semiconductors and most recently of carbon allotropes such as fullerenes, nanotubes and graphene.

The experimental possibility of isolating graphene, a two dimensional (2D) crystal consisting of carbon atoms arranged in honeycomb lattice, was demonstrated in 2004 and awarded the 2010 Nobel Prize in physics. Since then, a plethora of scientific activity in this field has uncovered its extraordinary properties across disciplines ranging from intriguing new physical phenomena to applications in nanotechnology, biology, chemistry [1, 2] etc.

Its electronic spectrum, which is a direct consequence of the presence of only C atoms and the symmetries of the honeycomb lattice, makes graphene different from the conventional 2D condensed matter systems. For condensed matter physicists, one of the driving forces to study graphene is to uncover the unique properties that arise from the fact that at low energies its electrons have a conical band structure and are described by a relativistic Dirac-Weyl Hamiltonian rather than a Schrödinger Hamiltonian.

The two dimensionality of the electrons in graphene is perhaps one of the most remarkable properties. Being one atom thick ($\approx 0.3nm$) graphene comes closest to a truly 2D material having its wavefunctions extend outside of the plane in

the third dimension [3] only by $\approx 0.3nm$. Previously studied two dimensional electron systems (2D) are typically formed by carriers trapped at the interface between layers of semiconductors as well as electrons floating on helium [4] , metallic surface states [5], etc . The fact that the carries of the semiconductor heterostructures are buried at at interface makes it experimentally challenging to use local probes [6] and learn about their electronic properties down to the atomic scales.

In contrast, for graphene, the charge carriers reside at the surface and thus that opens up the possibility of employing surface experimental techniques as Scanning Tunneling Microscopy and Spectroscopy to learn about its properties. The work presented in this thesis is an effort to understand the electronic properties of graphene at nanometer lengthscales while tuning external parameters such as magnetic field or concentration of charge carriers. In particular one of the hallmarks of two dimensionality is the Quantum Hall effect [7, 8, 9] and this regime is the focus of the studies presented in this thesis.

The challenges that come along with studying fundamental properties of graphene are related to (1) the fact that graphene is typically placed on a supporting substrate and thus susceptible to extrinsic disorder and (2) the fact that the small typical size of high quality samples poses experimental challenges for scanning probes. Both these issues are are addressed in the experiments presented in the following chapters.

Furthermore, stacking graphene layers one on top of the other produces electronic properties that are completely new. Thus in a bilayer the charge carriers are massive chiral fermions for the low energies. The properties of graphene stacks depend on the coupling between layers. Interestingly rotation between two layers away from the equilibrium Bernal stacking can significantly alter the electronic properties of graphene bilayer. Elucidating the effect of rotation on graphene multilayers is one of the topics of this thesis.

1.2 Graphene and its physical properties

1.2.1 Tight binding / band structure

The carbon atoms in graphene are arranged in a honeycomb lattice. This is not a Bravais lattice, but it can be represented as a triangular lattice with 2 atoms per unite cell. Figure 1.1 (a) shows the graphene lattice in real space, together with a choice of unit cell spanned by the vectors $\vec{a_1}$ and $\vec{a_2}$, $|\vec{a_1}| = |\vec{a_2}| = a = 2.46A^{\circ}$.

$$\vec{a_1} = \frac{a}{2}\left(1, \sqrt{3}\right); \vec{a_2} = \frac{a}{2}\left(1, -\sqrt{3}\right) \tag{1.1}$$

In reciprocal space, the lattice is also triangular and the unit vectors can be found from $\vec{b_i}\vec{a_j} = 2\pi\delta_{ij}$.

$$\vec{b_1} = \frac{2\pi}{a\sqrt{3}}\left(\sqrt{3}, 1\right); \vec{b_2} = \frac{2\pi}{a\sqrt{3}}\left(\sqrt{3}, -1\right) \tag{1.2}$$

As indicated is Figure 1.1 (b), the Brillouin zone (BZ) is a hexagon. Only two of the six corners are inequivalent and these special points of the BZ are called K and K′: $K = \left(\frac{4\pi}{3a}, 0\right)$; $K'\left(-\frac{4\pi}{3a}, 0\right)$. The low energy electronic properties of graphene are governed by the band structure around these points.

The electronic configuration for C is: $1s^2 2s^2 2p^2$. In plane, 3 σ bonds hybridize in a sp^2 configuration, while the perpendicular $2p_z$ makes covalent π bonds.

Most of the electronic properties of graphene are captured in a simple tight binding (TB) model [10, 11, 12]. In order to set up the TB Hamiltonian we are going to consider that each C atom has a π orbital. The transfer integrals can be calculated from $H_{ij} = \langle \Phi_i | H | \Phi_j \rangle$, where i, j$\in$ {A,B} index the sublattice and $\Phi_{i,j}$ the Bloch functions for the two atomic sites. Taking into account the distances to the nearest neighbors it can be shown that the tight binding Hamiltonian is [13]:

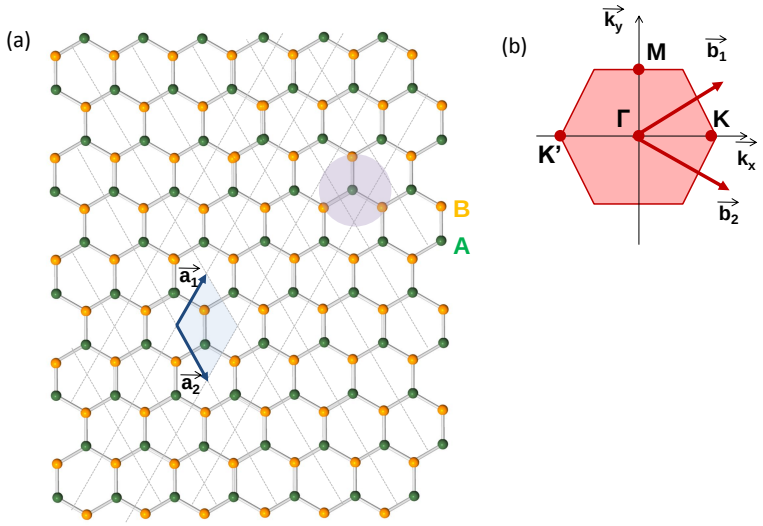

Figure 1.1: a) The honeycomb lattice of graphene with the two types of C atoms and the unit cell. b) The Brillouin zone of graphene.

$$H = \begin{pmatrix} H_{AA} & H_{AB} \\ H_{BA} & H_{BB} \end{pmatrix} = \begin{pmatrix} \epsilon_0 & tf\left(\vec{k}\right) \\ tf^*\left(\vec{k}\right) & \epsilon_0 \end{pmatrix} \tag{1.3}$$

where t is the nearest neighbor transfer integral, $\vec{\delta}_j$ are distances to the nearest neighbors, and $f(\vec{k})$:

$$f(\vec{k}) = \sum_{j=1}^{3} e^{i\vec{k}\vec{\delta}_j} = e^{i\frac{ak_y}{\sqrt{3}}} + e^{-\frac{iak_y}{2\sqrt{3}}} 2\cos\left(\frac{ak_x}{2}\right) \tag{1.4}$$

Similarly, the overlap matrix components are given by: $S_{ij} = \langle \Phi_i | \Phi_j \rangle$ and it is given by: $S = \begin{pmatrix} 1 & sf\left(\vec{k}\right) \\ sf^*\left(\vec{k}\right) & 1 \end{pmatrix}$

where s is the overlap integral.

In order to find the eigenstates and eigenvalues, we need to solve:

$$det\left|H - ES\right| = \begin{pmatrix} \epsilon_0 - E & tf\left(\vec{k}\right) - Esf\left(\vec{k}\right) \\ tf^*\left(\vec{k}\right) - Esf^*(\vec{k}) & \epsilon_0 - E \end{pmatrix} = 0$$

$$(E - \epsilon_0)^2 - (t - Es)^2 \left|f(\vec{k})\right| = 0 \tag{1.5}$$

$$E(\vec{k}) = \frac{\epsilon_0 \pm t\left|f(\vec{k})\right|}{1 \pm s\left|f(\vec{k})\right|} \tag{1.6}$$

When we assume $\epsilon_0 = s = 0$, the solution for the energy becomes:

$$E(k_x, k_y) = \pm t\sqrt{1 + 4\cos\left(\frac{ak_y\sqrt{3}}{2}\right)\cos\left(\frac{ak_x}{2}\right) + 4\cos^2\left(\frac{ak_x}{2}\right)} \tag{1.7}$$

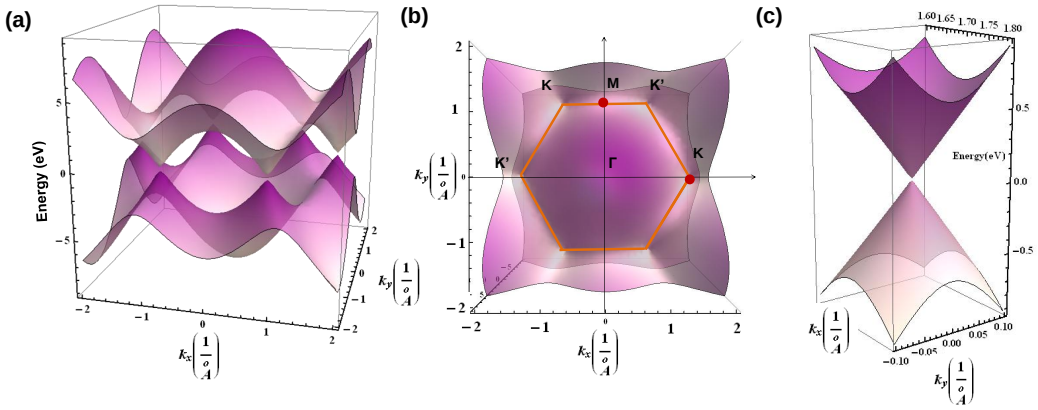

Figure 1.2: (a) The dispersion relation in graphene. (b) Top view highlighting the corners of the BZ. (c) A zoom into the dispersion close to one of the corners of the BZ.

This dispersion relation is plotted in Figure 1.2(a), where hoping parameter was taken to be $t = -3eV$. The BZ is highlighted in the top view, Figure 1.2(b).

The conduction and valence bands touch at the six corners of the BZ. Neutral graphene has one electron per C atom in the π band, hence taking the spin degree of freedom into account, the Fermi level is situated exactly at the K points. Therefore, at charge neutrality, the Fermi "surface" of graphene is represented by the six points which coincide with the corners of the Brillouin zone. We note that the electron and hole bands are symmetric. In this simple tight binding model only hopping to the nearest neighbor is taken into account. Models that take into

account hopping to the next nearest neighbors [14] show that such contributions can introduce electron-hole asymmetry.

Importantly, the absence of a gap at the K point is a direct consequence of the fact that in graphene the A and B sites are occupied by the same type of atom, C (so that $H_{AA} = H_{BB}$). A material with similar lattice structure but different species of atoms on the two sites is hexagonal boron nitride (BN). In this case because of the inequivalence of the A and B sites the system is an insulator and the band gap is 5.2eV.

1.2.2 Linear dispersion

Expanding the Hamiltonian around the K point one obtains: $\left(\vec{p} = \vec{k} - \left(\frac{4\pi}{3a}, 0\right)\right)$:

$$f_K = e^{i\frac{ap_y}{\sqrt{3}}} + e^{-\frac{iap_y}{2\sqrt{3}}} 2\cos\left(\frac{a\left(p_x + \frac{4\pi}{3a}\right)}{2}\right) \approx -a\frac{\sqrt{3}}{2}\left(p_x - ip_y\right) \tag{1.8}$$

This means that the dispersion is conical near the K points: $E = \pm ta\frac{\sqrt{3}}{2} \cdot |\vec{p}|$ as illustrated in Figure 1.2(c).

The electron velocity is given by $v = \frac{1}{\hbar}\left|\frac{dE}{dp}\right| = \frac{1}{\hbar}ta\frac{\sqrt{3}}{2}$. Because it is independent of momentum and thus equal to the velocity at the Fermi level, we will refer to it as v_F for the rest of the thesis.

The full Hamiltonian for both valleys combined in low energy approximation, becomes:

$$H = \hbar v_F \begin{pmatrix} H_K & 0 \\ 0 & H_{K'} \end{pmatrix} = \hbar v_F \begin{pmatrix} 0 & p_x - ip_y & 0 & 0 \\ p_x + ip_y & 0 & 0 & 0 \\ 0 & 0 & 0 & -p_x - ip_y \\ 0 & 0 & -p_x + ip_y & 0 \end{pmatrix} \tag{1.9}$$

The corresponding wavefunction has 4 components:

$$\Phi = \begin{pmatrix} \Phi_A^K \\ \Phi_B^K \\ \Phi_A^{K'} \\ \Phi_B^K \end{pmatrix} \tag{1.10}$$

In other words, near the Dirac points, the electrons in graphene obey a Dirac-Weyl Hamiltonian for massless particles:

$$H_K = \hbar v_F(\sigma_x p_x + \sigma_y p_y) = \hbar v_F \vec{\sigma} \cdot \vec{p} \tag{1.11}$$

where $\vec{\sigma_i}$ are the Pauli matrices,$\sigma_x = \begin{pmatrix} 0 & 1 \\ 1 & 0 \end{pmatrix}$ and $\sigma_y = \begin{pmatrix} 0 & -i \\ i & 0 \end{pmatrix}$.

In the case of graphene the spinor representation comes from the existence of two sub lattices, not from the real spin. The chirality operator, describing the the projection of $\vec{\sigma}$ onto the momentum $\vec{p}$, can be defined for graphene as $\frac{\vec{\sigma}\vec{p}}{|\vec{p}|}$. Because the Hamiltonian for electrons in graphene is $\hbar v_F \vec{\sigma} \cdot \vec{p}$, chirality commutes with it and thus it is a conserved quantity. The eigenvalues are for electrons and holes $+1$ and -1 respectively for one Dirac cone and the reverse for the second cone.

The fact that chirality is a conserved quantity has as consequence suppression of backscattering in graphene, which means that the electrons will transmit with probability 1 at normal incidence through a potential barrier [15].

1.2.3 Density of states in graphene

For a given crystal with a dispersion relation $E(\vec{p})$, in 3 dimensions, one can define the Density of States $DOS(E)$ which represents the number of energy states per unit energy range [16].

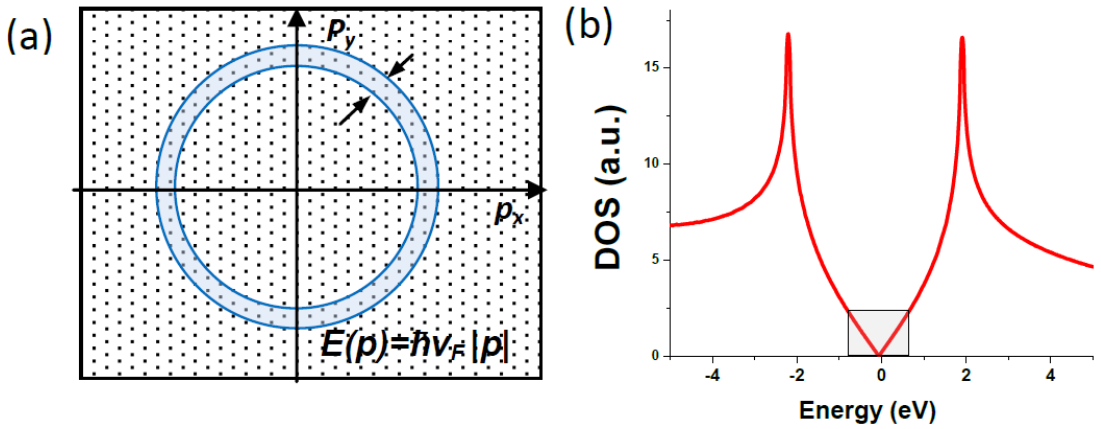

Figure 1.3: (a) Illustration of calculation of the DOS in the conical band structure at low energies in graphene. (a) DOS corresponding to Figure1.2(a).

$$DOS(E) = 2\int_{B.Z.} \frac{V}{(2\pi)^3}\delta\left(E(\vec{p}) - E\right) d\vec{p} = 2\int_{E(\vec{p})=E} \frac{V}{(2\pi)^3}\frac{dS}{|\nabla_{\vec{p}} E(\vec{p})|} \tag{1.12}$$

where $d\vec{p}$ is the volume element in momentum space and $V/(2\pi)^3$ is the density of allowed $\vec{p}$ vectors.

For graphene, at low energies where the dispersion can be considered conical (Figure1.3(a)) the expression for the density of states per unit area is $DOS = \frac{dN}{dE}$, where $N = \frac{\pi p^2}{(2\pi)^2}$ is the number of states within a circle of radius p (dN is the number of states enclosed by the blue area in Figure 1.3(a)):

$$DOS = 4 \times \frac{dN}{dE} = 4 \times \frac{E}{(2\pi)(\hbar v_F)^2} = \frac{2E}{\pi(\hbar v_F)^2} \tag{1.13}$$

The density of states in graphene for low energies is therefore linear and vanishes at the Dirac Point.

In general, if we look at Equation 1.12 we notice that critical points in the dispersion, for which $\nabla_{\vec{p}} E(\vec{p}) = 0$, will result in divergences in the density of states. These are called Van Hove singularities. It can be shown that in two dimensions maxima and minima of the bands result in jumps in the DOS while

a saddle point the DOS diverges logarithmically [17, 16].

Corresponding to the band structure plotted in Figure 1.2(a), the density of states is presented in Figure 1.3(b). In this case, the peaks in the DOS are Van hove singularities resulting from the saddle points in the graphene dispersion. The highlighted area in the low energy regime $E < 1eV$ is the regime in which the experimental results presented in this thesis are taken.

1.2.4 Graphene in magnetic field-Landau levels (LLs)

The energies of the LLs in graphene

In order to understand how electrons in graphene behave in a perpendicular magnetic field, **B**, we start from setting up a Hamiltonian that describes the massless Dirac electrons in the presence of a perpendicular field [18, 19, 20].

In finite field, the Hamiltonian is obtained by replacing the momentum p_i, $i = \{x, y\}$ with the canonical momentum $p_i \rightarrow p_i - eA_i$. Here **A** is the vector potential **B** $=\nabla \times$ **A**. One can already notice that the two valleys are decoupled. For example in the K valley $H_K \cdot \Phi = E \cdot \Phi$:

$$\hbar v_F \begin{pmatrix} 0 & p_x - ip_y \\ p_x + ip_y & 0 \end{pmatrix} \cdot \begin{pmatrix} \Phi_A \\ \Phi_B \end{pmatrix} = E \begin{pmatrix} \Phi_A \\ \Phi_B \end{pmatrix} \tag{1.14}$$

$$\begin{aligned} E \cdot \Phi_A &= \hbar v_F (p_x - ip_y) \Phi_B \\ E \cdot \Phi_B &= \hbar v_F (p_x + ip_y) \Phi_A \end{aligned} \tag{1.15}$$

$$\begin{aligned} E^2 \cdot \Phi_A &= \hbar v_F (p_x - ip_y) \cdot E \cdot \Phi_B = \hbar v_F (p_x - ip_y) \cdot \hbar v_F (p_x + ip_y) \Phi_A \\ E^2 \cdot \Phi_B &= \hbar v_F (p_x + ip_y) \cdot E \cdot \Phi_A = \hbar v_F (p_x + ip_y) \cdot \hbar v_F (p_x - ip_y) \Phi_B \end{aligned} \tag{1.16}$$

At this point we will substitute the canonical momentum. We have a freedom of gauge, meaning **A** is defined up to a ∇**A'** since $\nabla \times$ (**A** + ∇**A'**) = $\nabla \times$ **A** + $\nabla \times \nabla$**A'** = $\nabla \times$ **A** + 0. In the following we choose the Landau gauge in

which $\mathbf{A} = B(-y, 0, 0)$ (an alternative would have been the symmetric gauge $\mathbf{A} = B(-y, x, 0)$) In this case, $p_x \to p_x + eBy$, $p_y \to p_y$

$$\begin{aligned} E^2 \cdot \Phi_A = v_F(p_x + eBy - ip_y) \cdot \hbar v_F(p_x + \tfrac{e}{c}By + ip_y)\Phi_A \\ (\tfrac{E^2}{v_F^2} + eB\hbar) \cdot \Phi_A = ((p_x + eBy)^2 + p_y^2) \cdot \Phi_A \end{aligned} \tag{1.17}$$

To find the solution we can compare the form of the Hamiltonian with the harmonic oscillator and by analogy we can find the eigenenergies for the case of graphene.

For a Harmonic oscillator the energies and eigenvalues are:

$$\begin{aligned} H = \frac{\mathbf{p}_y^2}{2m} + \tfrac{1}{2}m\omega^2 \cdot \mathbf{y}^2 E_N = \hbar\omega(N + \tfrac{1}{2}), N \geq 0 \\ \Phi_N \propto e^{-\frac{m\omega y^2}{2\hbar}} \cdot H_N(\sqrt{\tfrac{m\omega}{\hbar}}y) \end{aligned} \tag{1.18}$$

Here, H_N are the Hermite polynomials.In analogy the energies and wavefunctions for the Landau levels in graphene are:

$$\begin{aligned} E_N = v_F\sqrt{2\hbar eBN}, N \geq 0 \\ \Phi_{A,N}(x, y) = e^{ik_x x}e^{-\frac{m\omega y^2}{2\hbar}} \cdot H_N(\sqrt{\tfrac{m\omega}{\hbar}}y) \end{aligned} \tag{1.19}$$

For the B sublattice, we obtain: $E_N = v_F\sqrt{2\hbar eBN}$ but $N \geq 1$ Notice that in this case the $N = 0$ index Landau level is missing meaning that for one valley this level is sublattice polarized. However, at the other valley it is polarized in the opposite way.

Thus, the dependence of the energies of the LLs in graphene on index and magnetic field is:

$$E_N = v_F\sqrt{2\hbar e \cdot B \cdot N} \tag{1.20}$$

This dependence is illustrated in Figure 1.4(a) where the energies of the LL (assuming $v_F = 10^6 m/s$) are plotted as a function of magnetic field.

The presence of the level $N = 0$ and the square root dependence in field and index are unique properties of graphene. In contrast, for conventional 2D electron

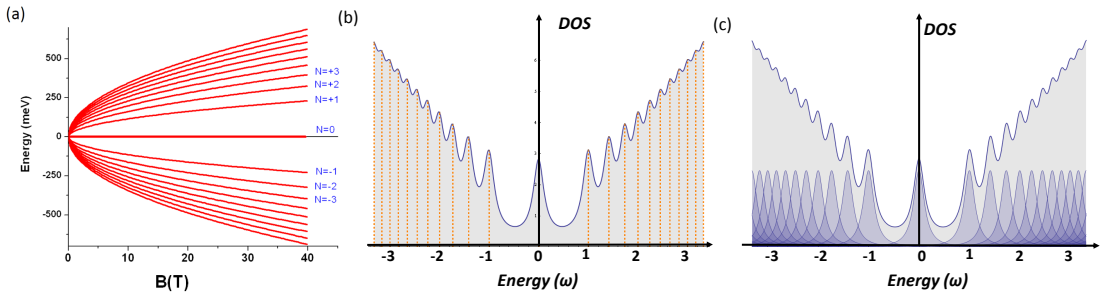

Figure 1.4: (a) Landau level energies for graphene as a function of magnetic field. (b) The delta function peaks of graphene broadened by disorder. (c) The overall background of the DOS arising due to summing up all the individual broadened LL peaks.

gas, the LL energies are equidistant, linear in magnetic field and there is no level at zero energy $E_N^{2DEG} = (\hbar eB)/(mc)(N+1/2), N \geq 0$, where m and e are effective electron mass and electron charge.

Degeneracy of the the Landau levels

In the Landau gauge description we notice that there are two quantum numbers that label the LL wavefunctions : the LL index N and k_x. Because the energies are independent of the second quantum number for an infinite sample the degeneracy of a LL is infinite. If we we consider a finite sample of area A, however, the degeneracy is $N_B = \frac{\Phi}{\Phi_0}$ where $\Phi = B \times A$ is the total magnetic flux threading the sample and Φ_0 is the elementary flux quantum. When taking into account the spin and valley degrees of freedom we need to multiply this degeneracy by a factor of 4.

A natural lengthscale for this system is the magnetic length, $l_B = \sqrt{\hbar/eB}$ which is roughly the spatial extend of the LL wavefunctions.

1.2.5 Connection with experimentally measured quantities

In some of the experiments presented in this thesis, the quantity that we measure with Scanning Tunneling Spectroscopy is proportional to the local density of

states at a position $\vec{r}$ in the sample plane and at a particular energy E. In the simplified case, this is a sum of contributions of amplitudes for the wavefunctions that are eigenstates of the system with energies E_s:

$$LDOS(\vec{r}, E) = \sum_s |\Phi_s(\vec{r})|^2 \delta(E - E_s) \tag{1.21}$$

Importantly, we note the gauge invariance of the measured quantities: while the wavefunctions corresponding the the Landau levels in graphene depend on the choice of gauge, the observables, such as the DOS are independent of the choice of gauge.

As pointed out before the electronic spectrum of graphene in the presence of a magnetic field consists of quantized energy levels. Each of the LLs with index N contributes a delta function peaked at its corresponding energy E_N to the density of states. As will be shown in more detail in Chapter 6, an in plane inhomogeneous electric field such as the one created by boundaries or disorder lifts the degeneracy of the LLs which can broaden them into a band. Figure 1.4(b) illustrates an example of such a spectrum with broadened levels where the dashed red lines indicate the energies of the LLs in units of cyclotron energy $\omega = v_F\sqrt{2e\hbar B}$.

To understand the overall shape of the density of states in Figure 1.4(b), one can plot a series of Lorenzian peaks with a finite width such as the ones in Figure 1.4(c). As demonstrated in the superposed plot of Figure 1.4(c), when summed up, because of their tails, the DOS will have broad peaks riding on top of a linear background.

In addition to unique electronic properties, the mechanical, thermal, optical, etc. properties of graphene are also notable [21, 22, 23, 1, 24]. Due to the strong in plane σ bonds, graphene is a very strong material, despite being one atom thick. Remarkably, the tensile strength ($10^6 MPa$) is superior to steel,

diamond and silicon and the stiffness (Young modulus $10^3 GPa$), while still smaller than diamond it is higher than that of steel [25, 26, 27]. Graphene sheets were also found to be impermeable to gases [28], a property that could be useful for applications in pressure sensors, barrier between different phases of matter etc. Graphene's thermal conductivity that can be as high as $5 \times 10^3 W/mK$ [29, 30] is the largest of any material measured.

Graphene is also chemically sensitive- it was shown that single molecules absorbed on graphene can result in measurable changes in the resistivity of a graphene device [31] which makes it a candidate for ultra sensitive chemical detectors.

Although it is one atom thick, graphene absorbs $\pi\alpha = \pi\frac{e^2}{\hbar c} \approx 2.3$ of incident light, where $\alpha = 1/137$ the fine structure constant. The fact that the absorption is significant makes it possible to see graphene. This is an interesting case where a property of a material depends solely on universal constants.

The combination all such remarkable properties makes graphene appealing not only to the condensed matter community but also to Chemistry, Biology, Engineering etc.

1.3 Overview of the thesis

The chapters of this thesis are structured in the following way:

Chapter 2 is an introduction to the experimental techniques and to the materials that were used in this thesis. The principle of operation of STM/STS, the experimental set-up and the nanofabrication methods of graphene devices are described. In the last section, the experimental technique and protocol that was developed and used for measuring micron size graphene samples on macroscopic substrates is described.

Chapter 3 discusses the STM/STS results for graphene samples in the absence of a magnetic field illustrating the effects of disorder on the electronic spectrum and topographic images. An introduction and experimental results are presented for tuning carrier concentration in graphene by electrostatic gating.

Studies of the electronic spectrum of graphene in the presence of a perpendicular magnetic field are presented in **Chapter 4** for samples of different disorder strength. In the case of a system where a top graphene layer is weakly coupled to tis graphite substrate, the effect of interlayer coupling on the LL spectrum is discussed.

In the presence of a magnetic field and a back-gate voltage STM/STS can probe the quantized LL spectrum in graphene and that is the topic of **Chapter 5**. The main features discussed are: the observation of a staircase pattern in the spectrum evolution with carrier density which is attributed to the discrete nature of the density of states in graphene in magnetic field and extrinsic features that appear in such spectra due to disorder. Using Landau level spectroscopy together with gating is used to obtain a direct measure of the different degeneracies for

single and a bilayer with large angle twist between layers. Furthermore **Chapter 5** contains a discussion connecting our results to the quantum Hall measurements in electronic transport.

Since trapped charges are the main source of disorder in graphene understanding their effect on the electronic spectrum is crucial. **Chapter 6** illustrates examples of the effect of isolated charges impurities on the LLs in graphene. We present the theoretical background and experimental evidence for spatial "'bending"' of the LLs for very weak potentials and lifting the orbital degeneracy of the LLs for stronger potential.

Chapter 7 is dedicated to the effect that introducing a twist between graphene layers has on the topography and electronic properties. The periodic pattern created in topographic images due to the rotation, called Moiré pattern is discussed. The main effect on the electronic spectrum that arises due to hybridization in momentum space of the two Dirac cones originating from the two layers is the presence of two saddle points that give rise to Van Hove singularities in the density of states. The angle dependence of this effect is discusses as well as the renormalization of the carrier velocity due to this change in the band structure.

The signatures that grain boundaries (periodic array of defects at the boundary between two graphene layers that are rotated with respect to each other) have on the properties of graphene are discussed in **Chapter 8** together with a comparison with theoretical *ab initio* calculations.

Chapter 9 is a summary of the main findings of the experiments presented in this thesis together with an outlook for future directions in which this work can be extended.

Chapter 2

Experimental Method - Scanning Tunneling Microscopy and Spectroscopy

2.1 Scanning Tunneling Microscopy and Spectroscopy

Parts of this chapter follow closely the text in [32, 33].

Scanning tunneling microscopy (STM) is a powerful technique used to study the surface morphology of materials as well as to learn about their electronic properties. The idea behind the operation of an STM, for which Gerd Binnig and Heinrich Rohrer were awarded the Nobel prize in 1986 [34] is conceptually simple. By bringing a sharp metallic tip atomically close ($\approx$ 1nm) to a conducting sample surface one can create a tunneling junction and when a bias voltage is applied between the two, a tunneling current will start flowing. Such a tunneling junction is depicted in Figure 2.1(a) where the sample and tip are separated by a vacuum barrier. The bias between tip and sample is V_B, the Fermi level of the sample is marked as E_F and the Fermi level of the tip is situated at an energy eV_B below it. The distance between tip and sample is d.

In this situation the electrons below the Fermi level of the sample will be tunneling into the tip, and therefore probe the filled electronic states of the sample. In the reverse situation, when the Fermi level of the tip is above that of the sample, the electrons are flowing out of the tip into the sample probing the empty states of the sample.

The current between the sample and the tip I_t can be calculated from a Fermi Golden rule expression which, for a finite temperature T, can be written

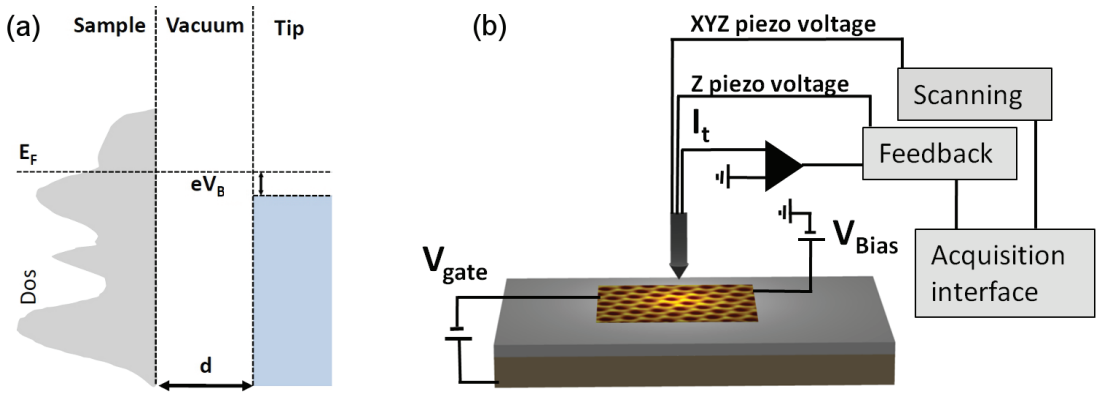

Figure 2.1: (a) Sketch of the tunneling junction between the tip and the sample in an STM experiment. The important quantities are indicated: the tip-sample separation d, the Fermi level E_F, the bias voltage V_B. The indicated DOS for the sample has an arbitrary shape and for the tip it is assumed constant.(b) Sketch of the STM set-up in which a graphene flake is placed on a Si/SiO_2 substrate. The main parts of an STM experiment are indicated: the scanning head, the feedback system, the data acquisition interface, the bias voltage and tunneling current. In addition, a gate voltage is applied between the graphene and the gate electrode (typically Si).

as [35, 36, 37, 38, 39]:

$$I \propto \frac{4\pi e}{\hbar} \int_{-\infty}^{+\infty} \left[f\left(E_F - eV_B + \epsilon\right) - f\left(E_F + \epsilon\right) \right] \times \rho_S\left(E_F - eV_B + \epsilon\right) \rho_T\left(E_F + \epsilon\right) |M|^2 \, d\epsilon \tag{2.1}$$

where $f(E) = \{1 + exp\left[\left(E - E_F\right)/k_B T\right]\}^{-1}$ is the Fermi distribution, ρ_S and ρ_T are the density of states (DOS) for the sample and tip respectively, m, e are electron mass and charge.

For measurements at 4K the thermal broadening $k_B T \approx 0.35 meV$, so if we assume low enough temperatures the Fermi function can be approximated as a step function so Equation 2.2 becomes:

$$I \propto \frac{4\pi e}{\hbar} \int_{0}^{eV_B} \rho_S\left(E_F - eV_B + \epsilon\right) \rho_T\left(E_F + \epsilon\right) |M|^2 \, d\epsilon \tag{2.2}$$

The origin of the matrix element is the the overlap of the wavefunctions of the sample and tip within the vacuum barrier. Therefore the explicit form depends

on the particular shape of the tip, but with the assumptions of a square tunnel barrier and wavefunctions exponentially decaying, the matrix element:

$$|M|^2 \propto e^{\frac{-2d}{\hbar}\sqrt{2m\Phi}} \tag{2.3}$$

Here, Φ is an effective height of the tunneling barrier which generally is a function of the work functions of the tip and sample.

Therefore, with all the discussed assumptions, the tunneling current reads:

$$I \propto e^{\frac{-2s}{\hbar}\sqrt{2m\Phi}} \int_0^{eV_B} \rho_S(E_F - eV_B + \epsilon)\rho_T(E_F + \epsilon)d\epsilon \tag{2.4}$$

Topography.

Using the STM to measure the topography of a sample is based on the condition that I_t is very sensitive to the tip-sample separation:

$$I \propto e^{\frac{-2d}{\hbar}} \tag{2.5}$$

The most commonly used measurement mode of STM is the constant current mode. In this mode initially a bias voltage is applied between the tip and sample and a tunneling current is set. The tip moves across the sample and it is raised or lowered by a feedback loop in order to keep the tunneling current constant. Tracing the contour made by the tip will therefore give information about the sample topography. It is such contours that we refer to as STM topographs. It is important to note however that the meaning of this contour of constant current is not simply the sample topography, but it can also reflect the contributions from the other terms in Equation 2.4 that related to the sample or tip density of states.

Spectroscopy.

If we assume that the tip density of states (DOS) is flat in the energy range of choice, by taking the derivative of I_t with respect to the V_B, we obtain:

$$\frac{dI_t}{dV_B} \propto \rho_S(eV) \tag{2.6}$$

Therefore, the STM can be used to learn about the density of states of the sample in scanning tunneling spectroscopy (STS) mode. For this, first the tunneling junction is set by applying a bias voltage and setting a tunneling current. Afterwards, the feedback loop is disabled and the tunneling current is recorded while varying the bias voltage. Typically this differential conductance is measured with a lock-in technique by applying a small ac. modulation to the bias voltage. Alternatively one could record the I-V curves and take a numerical derivate. Common materials used for the tip such as Pt/Ir, W, Au typically satisfy the condition of flat DOS for small enough voltages.

In this thesis maps of dI/dV as a function of spatial coordinates are presented. These are taken in the following way: an STS measurement is repeated on a grid of points across a chosen region. At a particular energy the value of the dI/dV in each point is mapped on the investigated region resulting in a dI/dV spatial map at that particular energy.

The main components of an STM experiment are sketched in Figure 2.1(b). In order to precisely position the tip on the sample and scan different areas, one uses piezoelectric materials for both fine scanning ($\approx$ nm-μm) and coarse movements ($\approx$ μm-mm). The feedback system allows for adjusting the tip vertical position in order to keep the tunneling current constant. In addition, for some of the samples studied in this thesis, a dc voltage is applied between the sample and the Si gate electrode using batteries.

2.2 Experimental set-up

The experiments described in this thesis were performed in a home built low temperature (4K), high magnetic field (12T) STM. The general set-up is such

that an insert having a the STM head at the end is placed in a liquid helium cryostat equipped with a 12T superconducting magnet (Cryomagnetics). The cryostat is supported by a vibration isolation table(TMC Laboratory Tables)(Figure 2.2(d)).

The key components of the STM insert are presented in Figure 2.2(a). The body of the head is made out of Ti, which is nonmagnetic. The sample stage, shown separately in Figure 2.2(a) contains a Au plated copper sample mount on top of a moving X-Y stage which is driven by piezo motors which are built based on the Pan design [40]. The sample holder makes contact with the wires by BeCu spring contacts. The scanning tube, in the inset of Figure 2.2(c) sits inside a sapphire prism which is moved by a coarse Z motor. The scanning piezo tube, which is what allows for the atomically small movements of tip has an outer part with 4 electrodes ($X_{\pm}$,$Y_{\pm}$) and an inner side (Z). In order to move the scanner one applies a dc voltage between the appropriate pair of electrodes depending on the desired direction.

The metallic tips used for thee experiments are made out of Pt-Ir, either commercially available or mechanically cut. The SEM image in Figure 2.3 (a) shows a typical example of a mechanically cut tip, which despite the irregular shape on large scales, becomes very sharp at the end (inset).

The samples showed in this thesis are graphene devices on Si/SiO_2 wafers which are particularly small in size for a standard STM experiment. An example of how the samples are mounted in the set-up is presented in Figure 2.3 (b). Typically the sample is glued onto a sapphire sample holder with rubber cement and the holder has a few Au contacts which are connected to the sample source/drain by wire bonding. The connection to the gate is done either by silver paint or wirebonding.

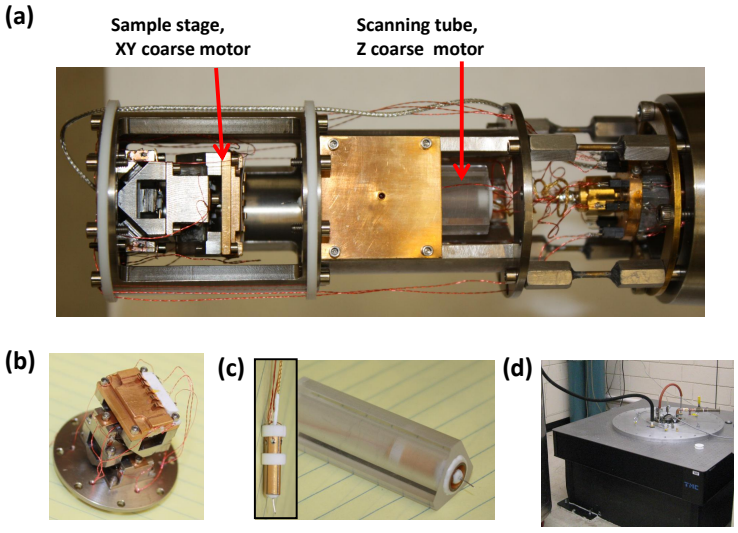

Figure 2.2: (a) Picture of the STM head. The main components are visible: sample stage on top of an XY coarse motor stage, scanning tube with Z coarse motor. (b) Sample stage detached from the scanning head. (c) Scanning head inside a sapphire prism. (d) Vibration isolation table supporting the cryostat in which the STM insert is operating.

2.3 Materials and Nanofabrication of graphene samples

Materials

The experiments on graphite crystals were done on commercial HOPG graphite (SPI). The graphene flakes for devices were exfoliated from either HOPG or natural graphite (Graphenium flakes from Graphit g.m.b.h.).

For some of the samples, hexagonal boron nitride (BN) was used as a substrate

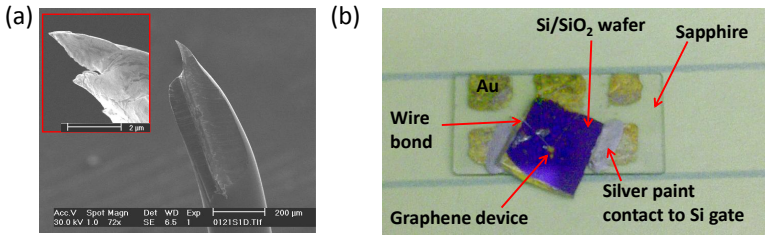

Figure 2.3: (a) SEM image of a freshly cut Pt-Ir tip. (b) A Si/SiO_2 wafer with a graphene device mounted on the STM sample holder.

for graphene. BN is an insulator with a hexagonal lattice structure similarly to graphene, but having the lattice constant larger by 1.7 %. The crystals used were grown and provided by the groups of Prof. K. Watanabe and Prof. T. Taniguchi.

Nanofabrication of graphene samples

In order to fabricate graphene devices one starts with a Si/SiO_2 wafer with thickness of $SiO_2 \approx 300$nm. As emphasized in the next chapter the oxide is crucial for the quality of the devices. We have found that devices produced with SiO_2 that was thermally grown and dry chlorinated (Nova Electronics) were of superior quality compared to the ones lacking the chlorination process.

The wafers are then patterned lithografically to have alignment grids so that the position of a a small graphene flake can be readily found under Scanning Electron Microscope (SEM) and optical microscope. To remove possible residues from the resist these substrates are then baked in a furnace at 230^oC in a forming gas atmosphere (H_2:Ar, 10%:90%).

The graphene flakes are obtained by so-called mechanical exfoliation. One starts from a piece of graphite and presses it onto a sticky tape (Ultron Tape) (Figure 2.4(b)) until thinner flakes of graphite are left on the tape. We then press the tape onto the Si/SiO_2 substrate so that islands of graphite with different thicknesses will be left (Figure 2.4(c)). In the next step, under optical microscope (Nikon Eclipse LV100) we identity those flakes which are a single layers graphene by their contrast in the optical image (Figure 2.4(d),(e)).

After a graphene flake was found on a substrate, metallic contacts are deposited with standard e-beam lithography (Figure 2.4(a)). The substrate is first coated with a resist, PMMA (poly methyl methacrylate) (MicroChem). Then the metallic leads are designed for the particular graphene flake using NPGS (Nano Pattern Generation System) and DesignCAD software followed by electron beam

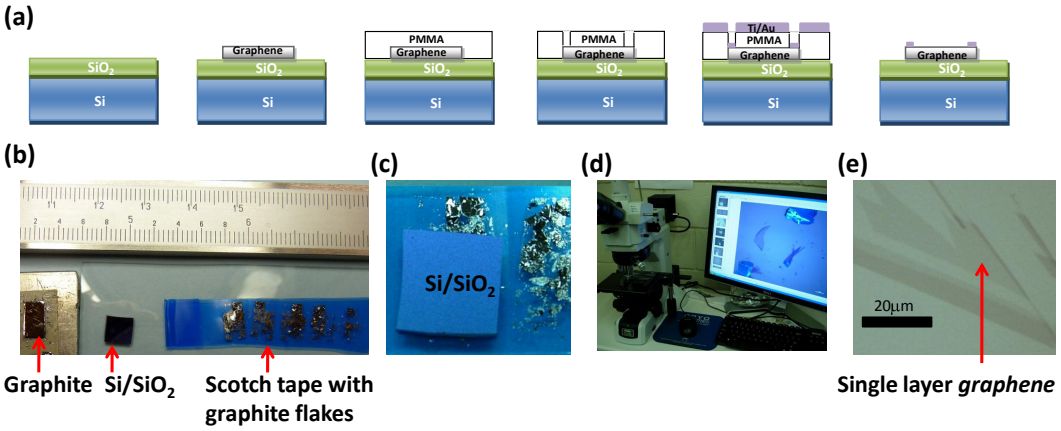

Figure 2.4: (a)Schematic of the lithography process to contact graphene. (b) Mechanical exfoliation of graphite using tape. (c) Transferring graphene/graphite onto the wafer by pressing the substrate into the tape. (d) Optical microscope is used for identifying graphene layers. (e) Optical microscope image of a single layer graphene.

writing (FEI Sirion). The pattern is developed using MIBK (Methyl isobutyl ketone) developer (1:3 MIBK:IPA). The metallic leads are deposited using electron beam evaporation (Thermionics 100-0030), using typically 1.5nm Ti and 30-60nm Au.

Examples of samples that were fabricated and measured in some of the STM experiments reported in this thesis are presented in Figure 2.5. In Figure 2.5(a) and (b) the optical micrograph of a sample having a graphene flake exfoliated onto SiO_2 is shown at different magnifications. A typical size of the graphene flake is 5-20μm. The choice for the shape of the metallic leads in Figure 2.5(b) is designed to facilitate finding such a small sample with an STM set-up as explained in the following section. Figure 2.5(c) shows the image of a similar device where graphene was transferred onto BN which was mechanically exfoliated onto SiO_2. In these samples a major challenge is the presence of trapped air bubbles from the fabrication procedure which need to be avoided while scanning the surface with the STM.

After lift-off in warm acetone and prior to measurement the samples are baked

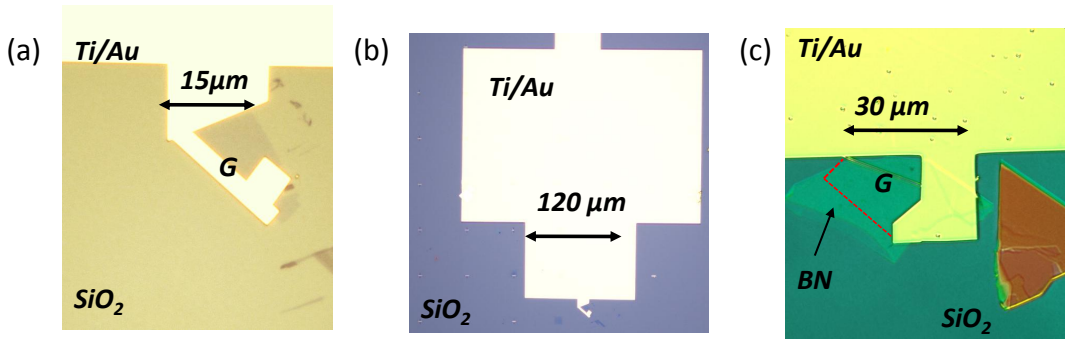

Figure 2.5: Optical microscope images of typical samples that were investigated. (a),(b) Two different magnifications illustrating a graphene flake deposited on SiO_2 patterned with Ti/Au contacts. (c) Sample having graphene transferred to BN and then patterned with Ti/Au contacts.

in a furnace at 230^{o}C in a forming gas atmosphere (H_2:Ar, 10%:90%).

Transfer procedure of graphene on a substrate

A major advance in sample preparation was demonstrated in [41] where Dean et al. develop a procedure to transfer mechanically exfoliated single layer graphene onto an arbitrary substrate, in particular onto BN. The method used for fabricating the samples in this thesis is a modified version of [41] and described in Figure 2.6.

In the first step one substrate is prepared by mechanically exfoliating BN flakes onto SiO_2 in a similar way to the exfoliation of graphene (Figure 2.6(a)). The selected BN flakes are typically $\approx$ 20nm thick and are inspected with the optical microscope to be free of large steps, defects etc.

Another substrate is prepared by first spin coating PVA (Polyvinyl alcohol)(Partall 10)(300rpm for 60s) and baking it for 5 min at 75^oC. On top of the PVA film an additional PMMA (A6) film is spin coated (1500 rpm for 60s) and baked for 5 min at 75^oC. On top of the two films one mechanically exfoliates single layer graphene (Figure 2.6(b)).

Such stack of PVA/PMMA allows peeling off the PMMA film with graphene

and depositing it on a support as shown in Figure 2.6(c),(d). Afterwards, the film is stuck to a glass slide under an optical microscope in such a way that the region with graphene is lifted above the plane of the film by placing a washer underneath as described by Figure 2.6(e). In the next step the graphene is brought above the BN deposited previously and using a micro-manipulator precisely aligned (Figure 2.6(f)). After pressing and heating up the BN substrate the PMMA film is released and it is stuck to the bottom substrate (Figure 2.6(g)).

The sample is then cleaned in warm acetone and baked in a furnace at 230°C in a forming gas atmosphere (H_2:Ar, 10%:90%). An example of a sample that was prepared in this way is presented in Figure 2.6(h).

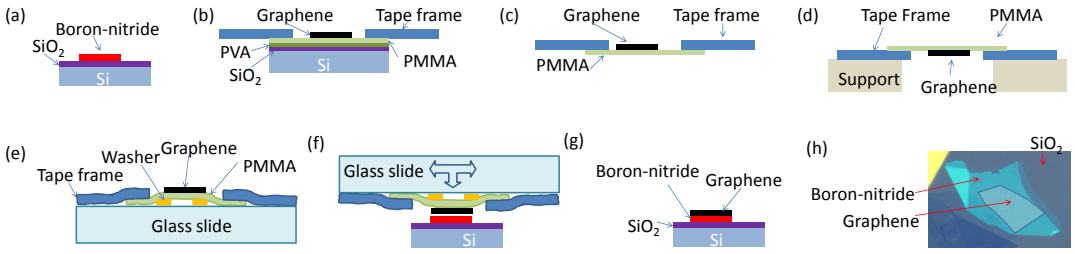

Figure 2.6: The steps of transferring graphene on BN. (a) Mechanical exfoliation of BN onto Si/SiO_2. (b) Mechanical exfoliation of graphene onto Si/SiO_2/PVA/PMMA with a tape frame for support. (c),(d) Graphene on PMMA is peeled off Si/SiO_2/PVA and put on a support. (e) The PMMA/graphene film on a glass slide with a washer placed in the area having graphene.(f) The glass slide is attached to a micromanipulator and under an optical microscope placed above the BN. (g) After applying pressure and heat the graphene is transferred onto BN. (h) Optical microscope image showing an area where graphene (the borders of graphene are guides to the eye) was transfered onto a BN flake. Image adapted from Alem-Mar Goncalves.

2.4 Method of measuring micron-size samples in a low temperature STM set-up

The discovery of graphene opened exciting opportunities to study a 2D system by surface probes. However, the fact that the samples obtained by exfoliation

are only a few microns in size poses technical challenges. The STM piezo-electric tube scanner can accurately control the position of the tip within angstroms, but the high resolution of this technique limits its field of view, which is typically smaller than 1μm. To move the tip across larger distances (microns-mm) coarse positioning X,Y,Z stages are sometimes used.

The challenge for studying graphene samples with STM is that the technique is nearsighted and it is difficult to locate micron size graphene flakes on macroscopic Si/SiO_2 substrates. The first idea would be to use the topographic images as a guide towards the sample [42, 43], but in practice this means taking and comparing many small size images. The scanning speed is typically very small due to the small working distance of the STM and the tip needs to be frequently retracted and approached for each scan since the piezo-electric scanner has a limited dynamic range ($\approx$ 100nm) making it likely to experience. This type of navigation guided by topographic features is therefore very slow and prone to frequent tip crashes. Moreover, in the case of the graphene devices, a large area around is insulating which makes it even more likely to have the STM tip crash before finding the sample.

Some set-ups are solving this problem by adding additional components: long range optical microscopes or scanning electron microscopes [44, 45]. However, most low temperature and magnetic field setups are lacking such tools because their addition complicates the design and stability. For this reason our group has developed a capacitive method in order to guide the STM tip towards micron size samples [32].

General set-up of the method

To measure STS one usually applies a small ac modulation to the sample bias voltage, $\tilde{V_s}$, so that there is an ac current, $\tilde{I}$, flowing through the STM tip:

$$\tilde{I} = G_t \cdot \tilde{V_s} + i\omega C\tilde{V_s} \tag{2.7}$$

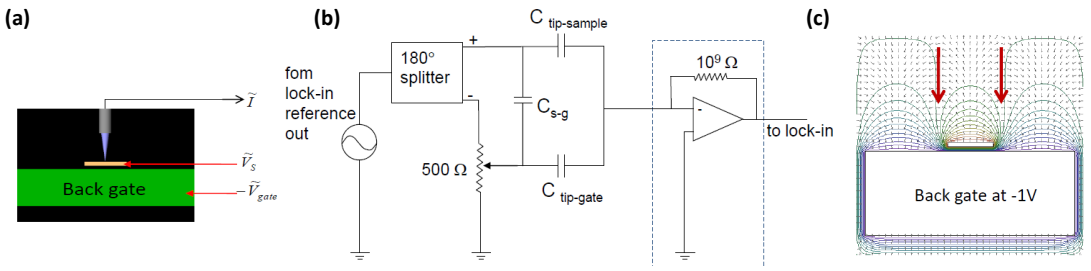

Figure 2.7: (a),(b) Schematic experimental setup and its electrical circuit. (c)Electric field distribution (Field Precision TC (educational 7.0)) near a conducting bar extending out of the paper. The strip is at 1 V, the back gate at -1V. The arrows indicate the sample edges.

, where G_t is the tunneling conductance and C is the tip-sample capacitance. The contributions to the ac current are from tunneling (first term) and from capacitive pickup (second term). The pick-up signal can be used to resolve small structures when the tip is far from the surface and it is not in the tunneling regime. When the tip moves across the sample at a typical height of 3 μm in the X,Y place there is a capacitance change, however its typical magnitude $\approx 30aF$ /(for movements of $5\mu m$) is much smaller than the typical background pickup which is $6fF$. That is why, in order to use the capacitance signal to identify features on the surface, the background pickup needs to be minimized. This is achieved using a set-up described in Figure 2.7(b).

The output voltage from the reference channel of a lock-in amplifier is split into two with 180^o phase shift. One of the signals (+) is applied to the sample directly as $\tilde{V_s}$, the other (-) is applied to the gate $-\tilde{V_{gate}}$ through a pot resistor to adjust the amplitude. The capacitive pickup current measured from the tip is $\tilde{I}$.

One key aspect of the procedure is tuning the voltage applied to the back gate in order to minimize the background pick-up current. To qualitatively illustrate the sensitivity of this method in detecting sample edges, Figure 2.7 (c) shows the electric field lines around the sample, when $V_s = 1V$ and $V_{gate} = -1V$, highlighting the presence of steep potential lines at the edges of the sample.

Finding the edge of a sample

The measured capacitive current across one of the $200\mu m$ Au pads of is shown in Figure 2.8. For the case of Figure 2.8(a) the tip was 60 μm away and for Figure 2.8(b) 200 μm away. The vertical left axis is the measured current and the horizontal axis is the position on the pad.

The signal is higher when the tip is above the pad and smaller when it is off the pad, riding on top of an overall background signal. In the derivative of this current with respect to position (right side axis) the edges of the pad can be identified as two sharp kinks when the tip is closer to the surface. The derivative is very effective in identifying the edges since, as can be see from the figures, although the background can be different for different heights, when the derivative is taken, the edges are readily identified. These two features become less pronounced as the tip is raised further away. This is seen in Figure 2.8(c), where the spatial derivative of the capacitive currents is plotted for different heights. The signal at the center of the sample, however is always the same.

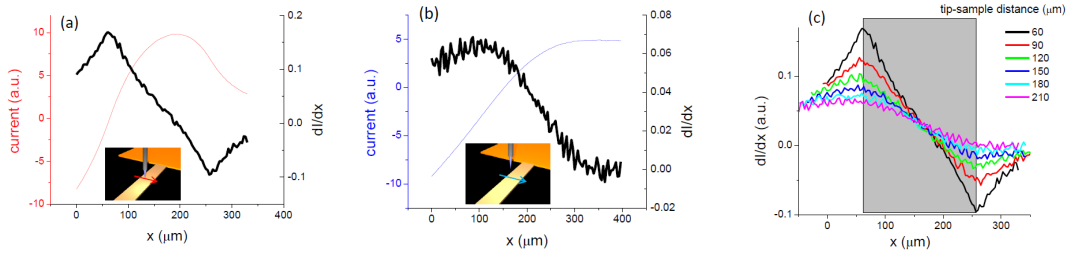

Figure 2.8: (a) Dependence of the capacitive currents as the STM tip moves above a thin metallic pad. The tip is 60 μm above a 200 μm wide film. Thin line: pickup current. Thick line: spatial derivative dI/dx. Insert: schematic diagram of tip-sample geometry. (b) Same as (a) but with tip-sample distance of 210 μm (c) Spatial derivative dI/dx for various tip-sample distances. Data are centered relative to the shaded area that shows the 200 μm wide sample.

This measurement was repeated for Au pads with different dimensions as described in Figure 2.9(a), where this method reliably identifies the edges of structures down to 1μm.

Protocol of finding a sample

Another novel and crucial component for reliably finding a small graphene sample is the design of the metallic lead. This lead is made of connected pads which are becoming smaller in size closer to the sample, as illustrated in Figure 2.9(a). This contact pad geometry makes it possible to locate small (micron size) samples on large (mm size) substrates with an STM tip alone, without the aid of complicated optical microscopy setups.

The procedure for finding a graphene sample is:

We start from room temperature and position the tip above the largest pad. When the STM is transfered into the cryostat and cooled to 4K, the tip could drift $\approx 100\mu$m away.

With the tip far away from the sample and above the largest pad (which is usually $\approx 200\ \mu\text{m} \times 200\ \mu\text{m}$, we use the derivative of the capacitive current to locate the center of the pad where we land the tip in the STM mode. At this time the large ac modulation is turned off.

The tip is then retracted to a height corresponding to an aspect ratio relative to the size of the pad of $\approx$0.3 so for the next scan across the pad in the capacitance mode the edges can be much better resolved.

Then one needs to move to the smaller pad. That is usually done by crossing the lower boundary of the larger pad as seen in Figure 2.9(b) right panel.

The procedure is repeated until the smallest pad and sample are found. The sensitivity of this method is sufficient for finding samples of a few microns as demonstrated in [46].

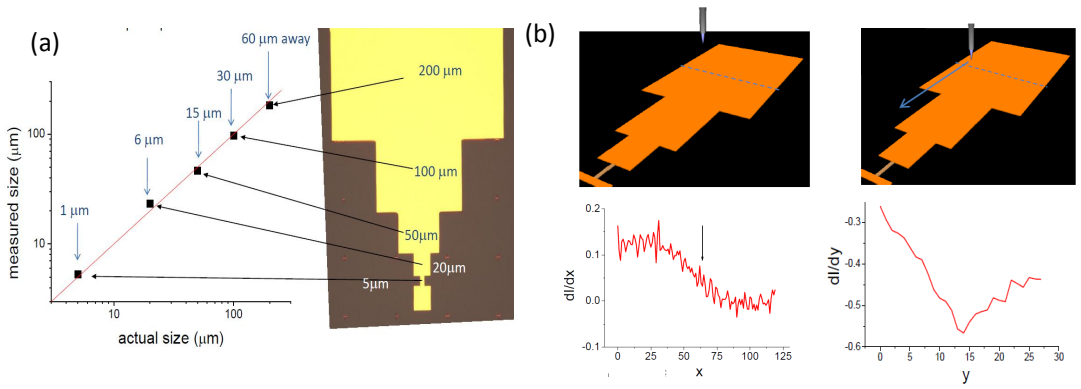

Figure 2.9: (a)Sample widths measured by the capacitance method. Measured size versus actual size. Tip-sample distances adjusted for sharp edge resolution, corresponding to aspect ratios of 0.3 or less. Thin line is a guide to the eye through the values of the measured widths (b)Left: Possible drift of tip position after transferring and cooling down and derivative of capacitive currents along the dashed line. Right:Tip near one edge ready to search for the lower boundary of the pad and derivative of capacitive currents along the dashed line.

Chapter 3
From disordered graphene to ideal graphene

Graphene on SiO_2. Graphene was initially isolated by mechanical exfoliation from graphite (Highly Oriented Pyrolitic Graphite (HOPG) or natural graphite) onto Si wafers capped with SiO_2 [47, 48]. In order to fabricate devices from these flakes, metallic contacts are added using standard e-beam lithography. This sample configuration allows using the highly doped Si as a back gate so that by applying a voltage between the flake and the back gate one can tune the carrier density in graphene. Much of the experimental work and in particular transport experiments have used this type of sample, but they are far from ideal.

Firstly, the nanofarbrication procedure can result in disorder that can reside either between the graphene and the SiO_2 or on the surface of graphene. Secondly, graphene will conform to the surface of SiO_2 and it will therefore be rippled. An illustration of this situation is presented in Figure 3.3. As a consequence of the disorder, the Fermi level of neutral graphene will not coincide with the Dirac point, meaning graphene is doped [49, 50]. The doping varies on the surface of graphene creating puddles of different carrier density (electron-hole puddles)[49, 50].

One of the main sources of the electron-hole puddles in graphene is the random potential induced by the substrate. For the standard SiO_2 substrates which are routinely used in graphene devices this is particularly problematic due to the presence of trapped charges and dangling bonds [51]. Improving the quality of the SiO_2 substrates by dry-chlorination leads to a significant reduction in the random potential. The use of these substrates gave access to the intrinsic properties of

graphene allowing the observation of Landau levels as detailed in a later section [46].

Graphene on hexagonal boron nitride (BN), mica etc. More recently, experimental methods were developed to manipulate other 2D materials from layered structures (e.g. BN)[47, 41]. In order to minimize the disorder due to the underlying substrate while still preserving the possibility of gating, graphene was placed on thin flakes of BN which in turn, were previously exfoliated on Si/SiO_2. The quality improvement by using BN as a substrate was significant; the mobilities for devices were above 100000 cm^2/Vs which is an order of magnitude higher than typical graphene devices on SiO_2 [41]. In very high magnetic fields the fractional quantum hall effect was also observed in such samples [52]. Another substrate demonstrated to be suitable for obtaining flat graphene is mica [53, 54].

Graphene flakes on graphite. After cleavage of a graphite crystal, one often finds graphene flakes on the surface which are decoupled from the bulk graphite underneath. These flakes provide the most favorable conditions for accessing the intrinsic electronic properties of graphene as detailed in the following sections [44, 55, 56].

Epitaxial graphene, graphene obtained by chemical vapor deposition etc. Other avenues of producing graphene are epitaxial growth on SiC crystals [57, 58, 59] and chemical vapor deposition (CVD) [60, 61, 62]. In the epitaxial growth one starts with a SiC crystal terminated in Si or C and annealing to temperatures above 1500 ^{o}C leads to the formation of graphene layers at the surface. Often the layers are misoriented with respect to each other thereby forming Moiré patterns. For the CVD growth, a metallic substrate that plays the role of a catalyst is placed in a hot furnace in a flow of gaseous carbon source.

As a result, carbon is absorbed into the metal surfaces at high temperatures and precipitated out to form graphene during cool down [63]. Other metallic substrates used for growing graphene films include Ru [64, 65], Ir [66, 67] and Pt [68].

Parts of this chapter follow closely the text in [33, 46, 69].

3.1 Surface topography of graphene

The discussion about the morphology of a graphene surface is important because the stability of a 2D membrane in a 3D world is closely related to the tendency toward crumpling or rippling [70, 71]. The degree of rippling also influences the quality of the electronic properties [72]. The morphology of the graphene surface depends strongly on the type of substrate (or lack of substrate) underneath.

Transmission Electron Microscope (TEM) experiments performed on graphene films placed on TEM grids show that there is an intrinsic rippling of the suspended graphene membrane with deformations of up to 1nm [73]. However, when deposited on a flat surface such as mica [53], BN [74, 75], or HOPG [69] the height corrugations become as small as 20-30pm. On the surface of SiO_2 the Van der Waals forces will make graphene conform to the rough surface and typical values reported for the corrugations are 0.5nm in height and a few nm in the lateral dimension [44, 76, 50, 46, 77].

The first STM experiments on graphene deposited on SiO_2 showed that the lattice is indeed hexagonal with almost no defects [43]. Moreover, they also showed the importance of sample cleaning in order to access the pristine graphene surface [45]. A more extensive analysis of the correlation between the substrate roughness and intrinsic graphene roughness [44] suggested that in areas where the graphene does not conform to the oxide surface and it is suspended over the high points, one can find an additional intrinsic corrugation on smaller length scales

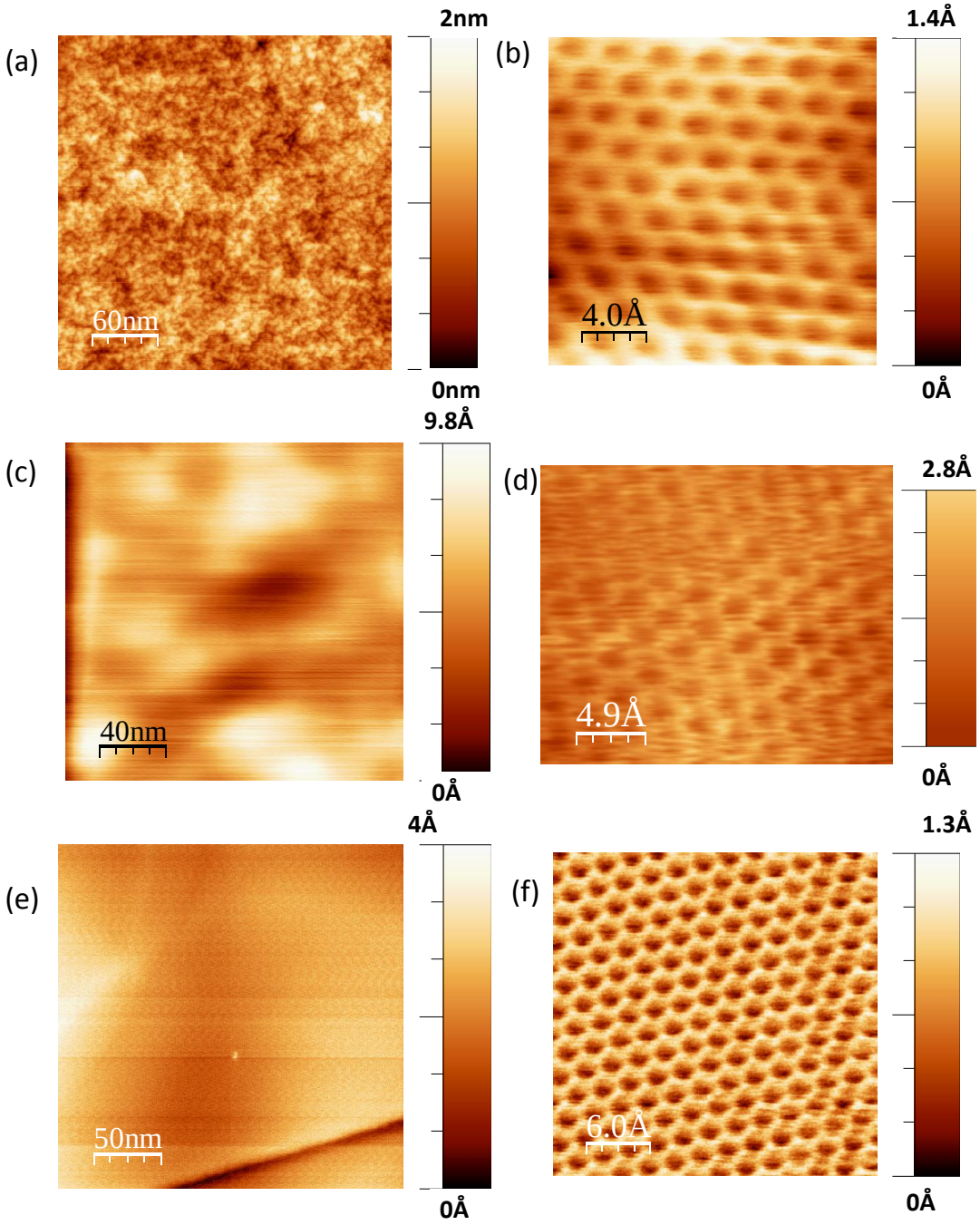

Figure 3.1: (a) Topography of typical area of graphene on SiO_2. (b) Atomic resolution taken of graphene on SiO_2. (c) Topography of typical area of graphene on BN. (d) Atomic resolution of graphene on BN. (c) Topography of typical area of graphene on graphite. (d) Atomic resolution of graphene on graphite. Tunneling conditions: V_b=300mV, I_t=20pA.

consistent with TEM studies [73].

A comparison between typical STM data for graphene on SiO_2, graphene on BN and decoupled graphene flakes on HOPG is presented in Figure 3.1. In Figure 3.1(a) the topography of a graphene area on SiO_2 shows a rippled surface. In contrast, graphene on BN is much flatter as seen in the topography map in Figure 3.1(c). The corresponding atomic resolution data demonstrates that despite the corrugation of the surface of graphene, the honeycomb lattice is continuous across the hills and valleys (Figure 3.1 (b),(d)). A comparison between the surface morphology for areas of graphene on SiO_2 and on BN shows that, when placed on BN, graphene is one order of magnitude smoother than on SiO_2. On such samples STM/STS experiments report Moiré patterns that arise because of the lattice mismatch and rotation between graphene and the BN [74, 75]. Furthermore, the random potential fluctuation measured by scanning tunneling spectroscopy appears sometimes smaller than on graphene samples exfoliated on SiO_2 [74, 75]. Interestingly, as it will be discussed in a later chapter, the electronic spectrum in magnetic field is not greatly improved, but rather comparable to the one on SiO_2.

For the case of graphene flakes decoupled on graphite surface the large area is also rippled-free (Figure 3.1(e)) and shows a hexagonal lattice in the atomic resolution images Figure 3.1(f). Remarkably, in all cases the graphene lattice is defect-free over areas as large as hundreds of nanometers.

3.2 Tunneling spectroscopy of graphene

One of the reasons why graphene has attracted so much interest is its unique electronic band structure. In the low energy regime the charge carriers obey a Dirac-Weyl Hamiltonian and have a conical dispersion. To the first approximation, it is possible to obtain a closed analytical form for the density of states at

low energy [10]:

$$\rho(E) = \frac{2A_c}{\pi}\frac{|E|}{v_F^2} \tag{3.1}$$

where, A_c is the unit cell area of graphene lattice.

The DOS in graphene differs qualitatively from that in non-relativistic 2D electron systems leading to important experimental consequences. It is linear in energy, electron-hole symmetric and vanishes at the Dirac point (DP) - as opposed to a constant value in the non-relativistic case. This makes it easy to dope graphene with an externally applied gate voltage. At zero doping, the lower half of the band is filled exactly up to the Dirac points. Applying a voltage to the graphene relative to the gate electrode (when graphene is on Si/SiO_2, the highly doped Si is the back gate) induces a nonzero charge. This is equivalent to injecting, depending on the sign of the voltage, electrons in the upper half of Dirac cones or holes in the lower half. Due to electron-hole symmetry the gating is ambipolar [78].

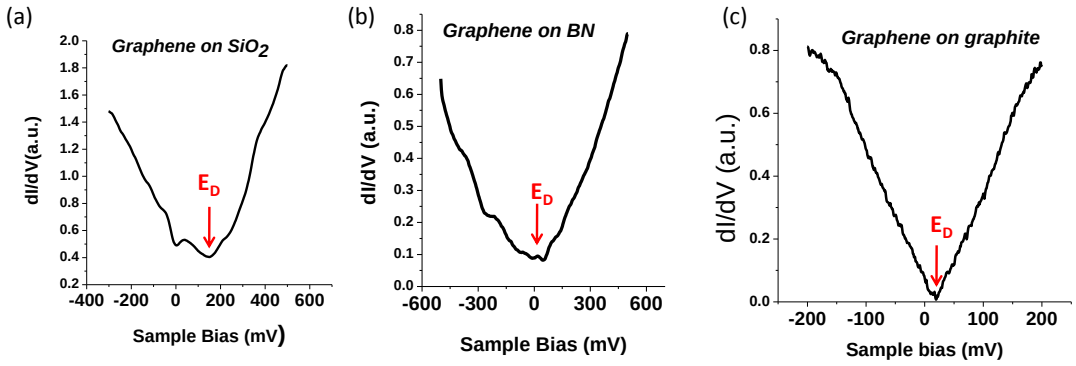

Figure 3.2: (a) STS spectrum of graphene on SiO_2. The Dirac Point is marked as E_D. (b) STS spectrum of graphene on BN. (c) STS spectrum of graphene on graphite.

However, when disorder introduces a random potential, as is the case for the graphene on SiO_2, the spectrum deviates from the ideal V-shape [77, 79, 80, 81, 76]. Some of the measured features in the spectra were attributed to strain and

ripples [81], others to local doping due to impurities. A typical spectrum is presented in Figure 3.2(a)[46]. In this case, the Dirac point is shifted from the Fermi energy by $\approx 200meV$ corresponding to a carrier concentration $n = 2 \times 10^{12} cm^{-2}$. Some STM experiments on graphene exfoliated on SiO_2 reported a gap at the Fermi level which was attributed to inelastic tunneling into graphene (via phonon scattering) [80]. In other experiments though, the gap is seen only above certain tunneling currents [79]. In most cases a dip at the Fermi level is observed in the tunneling spectra of graphene on SiO_2 [77, 46] which can be attributed to a zero bias anomaly.

The case of graphene on BN is similar to SiO_2 in the sense that the spectrum also deviated from a V-shape, however in this case, the majority of the samples have a Dirac Point that is close to the Fermi level, as illustrated in Figure 3.2(b). For graphene on graphite the measured density of states is linear and vanishes at the Dirac point (Figure 3.2(f)) as expected from theory. For the data shown in Figure 3.2(c), the Fermi level is slightly shifted away from the Dirac point ($\approx$ 16meV) corresponding to hole doping with a surface density $n = 2 \times 10^{10} cm^{-2}$.

3.3 Carrier concentration in graphene

3.3.1 Charge carrier inhomogeneity

Theoretically, in neutral graphene the Fermi level should coincide with the Dirac point. However, it is observed that graphene is often doped such that there is an energy difference between the Dirac point energy (E_D) and the Fermi energy (E_F). To find the dopant concentration, the carrier density can be calculated as follows:

$$n = \frac{N}{A} = 4\frac{\pi k_F^2}{(2\pi)^2} = \frac{k_F^2}{\pi} = \frac{1}{\pi}\frac{E_F^2}{\hbar^2 v_F^2} \tag{3.2}$$

Here the Fermi velocity is $v_F = 10^6 m/s$ and taking $E_F = 1meV$ we get $n \approx 10^8/cm^2$.

The origin of this doping is not yet well understood. However, the most likely causes are trapped charges and absorbed species at edges/defects etc. Recent STM experiments using graphene films doped on purpose with nitrogen (N) were aimed at characterizing at atomic scales the electronic structure modifications due to individual dopants [82]. It was found that N, which bonds with the carbon in the lattice, can contribute to the total number of mobile carriers in graphene resulting in a shift of the Dirac point. Moreover, the electronic properties of graphene are modified around an individual N dopant on length scales of only a few atomic spacings [82].

The existence of electron-hole puddles was first pointed out by single electron transistor studies with a spatial resolution of a hundred nm [49]. Higher resolution studies of the spatial fluctuations of the carrier distribution using STM showed even finer density fluctuations on nm scales [50]. The typical variation in Dirac point of graphene deposited on SiO_2 was found to be 30-50meV corresponding to carrier densities of $(2 \times 10^{11} - 4 \times 10^{11}) cm^{-2}$ [50, 49, 46].

Figure 3.4 qualitatively illustrates the electrostatic potential created by random trapped charges that electrons in graphene see on the supported devices. To simulate the effect of trapped charges in the substrate, 3000 point charges of magnitude $\pm$1e,$\pm$2e were randomly distributed in a volume 1μx1μx20nm and for each point in space and the resulting electrostatic potential was calculated.

Planes at different height were considered and the potential on those planes was calculated. The resulting maps for 3 different heights 1nm, 15nm, 30nm are shown in Figure 3.4(a), (b) and (c) respectively. This illustrates how on a plane that is close to the impurities the variation of the electrostatic potential in the XY direction is very large and on short length scales. For planes at larger distances vertically from the impurities, the potential becomes weaker and varies smoothly.

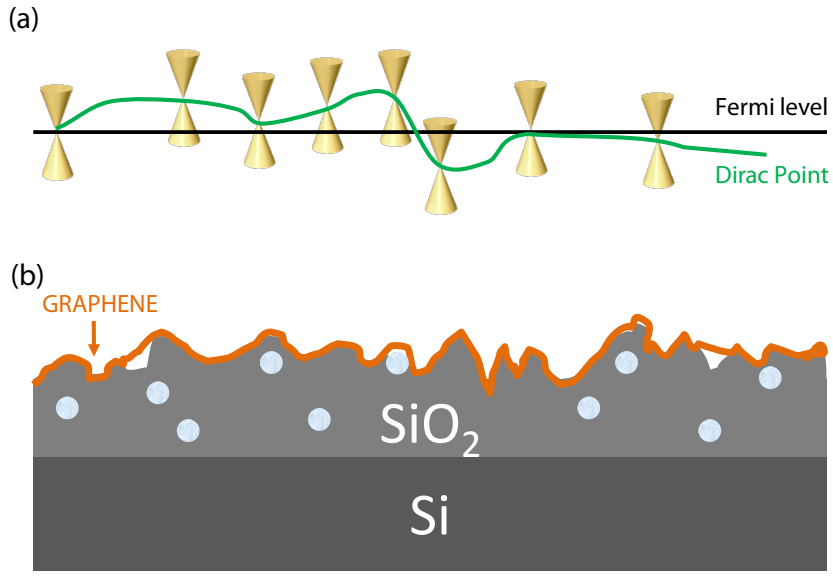

Figure 3.3: (a) Illustration of the varying carrier concentration across a graphene sample due to the random potential underneath. The Fermi level and the Dirac point are shown by the black and green lines respectively. (b) Sketch of how graphene (the orange line) deposited on the surface of SiO_2 will have a roughness comparable to the substrate [44]. The light gray dots illustrate trapped charges.

Therefore, the idea of using a spacer between the SiO_2 and graphene such as a single crystal insulator, BN, is justified, provided of course, that the BN itself carriers no trapped charges.

The electronic wave functions of the carriers in graphene can, in the presence of scatters, interfere and form standing wave patterns observed by measuring the spatial dependence of dI/dV. From the Fourier transform of such pattern one can obtain information about the momentum of the quasiparticles and thus learn about the band structure. [83].

The inhomogeneous carrier density is also visible in the in the local density of state map shown in Figure 3.5(b), which corresponds to the region for which the topography is shown in Figure 3.5(b). From such maps we estimate that the typical legthscale of the charge inhomogeneity, the so called puddle size is d≈20

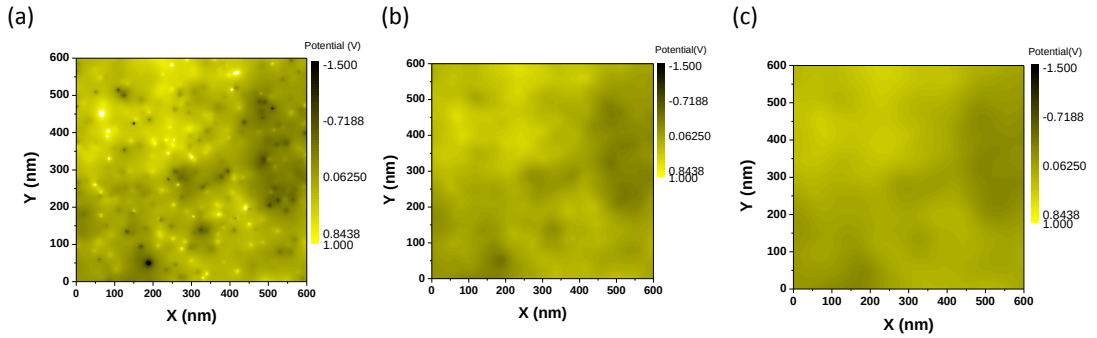

Figure 3.4: (a) Intensity map of the electrostatic potential created at 1nm above a box of size 1μx1μx20nm containing 3000 randomly distributed charges. (b),(c) Same as (a) at distances 15nm and 30nm.

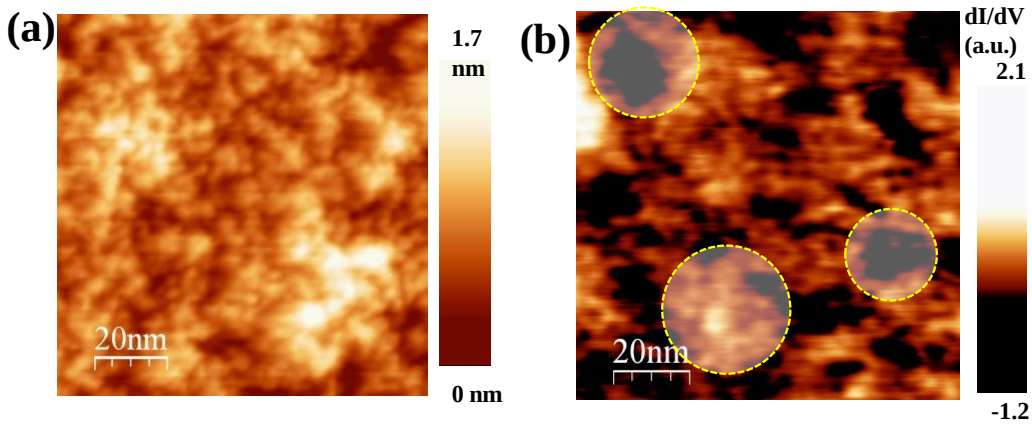

Figure 3.5: (a)Topography image corresponding to the local density of states (LDOS) map in (b) (I_t=20pA, V_b=140mV). LDOS map taken at E = 140 meV showing doping inhomogeneity in graphene. The highlighted area are example of puddles of doping inhomogeneity.

nm.

In contrast to graphene on SiO_2, graphene on graphite shows very little variation of the Dirac point ($\approx$ 5meV) across hundreds of nm [55, 69]. This is illustrated in a later chapter by the spatial map of the distance between the Dirac point and the Fermi level as measured in the presence of a magnetic field. The value of the Dirac point was extracted by fitting the Landau level sequence. Further demonstration of the homogeneity of the graphene flakes on graphite is given by the Fermi velocity which is found to vary by less than 5% across the same area.

Similarly, the fluctuations of the local charge density in graphene on h-BN were recently found to smaller, up to an order of magnitude, than on SiO_2 [74, 75].

3.3.2 Electrostatic gating

By applying a voltage between graphene and a back-gate electrode, Si, one can induce a surplus of electrons or holes in graphene (Figure 3.6)(a). The relationship between the number of carriers induced can be derived from a capacitance formula:

$$V_g = \frac{n \cdot e}{c} \tag{3.3}$$

Here V_g is the gate voltage, e is the elementary charge, n is the carrier concentration and c is the capacitance per unit area between the graphene and the gate. This value can be estimated from geometrical considerations:

$$c = \frac{\epsilon_0 \times \epsilon_r}{d} \tag{3.4}$$

where $\epsilon_0 \approx 1.854 \times 10^{-12} F/m$ is the vacuum permittivity, ϵ_r is the dielectric constant of the insulator that separates graphene from the gate and d is the distance between graphene and Si. For typical values, ϵ_{SiO_2}=3.9 and $d \approx 300nm$, we obtain a value of $c = 115 \times 10^{-6} F/m^2$, or $c = 115 \times aF/(\mu m)^2$

Given this value of the capacitance, applying 1V of gate voltage will introduce $n = 7 \times 10^{10} cm^{-2}$ carriers in the graphene sample.

From Equations 3.2 and 3.3 the relationship between the gate voltage and distance between Dirac point and Fermi level reads:

$$|E_F - E_D| = \hbar v_F \sqrt{\frac{\pi c |V_g|}{e}} \tag{3.5}$$

Experimentally this was checked by measuring the STS spectra and following the Dirac Point while changing the gate voltage. An example of spectra taken

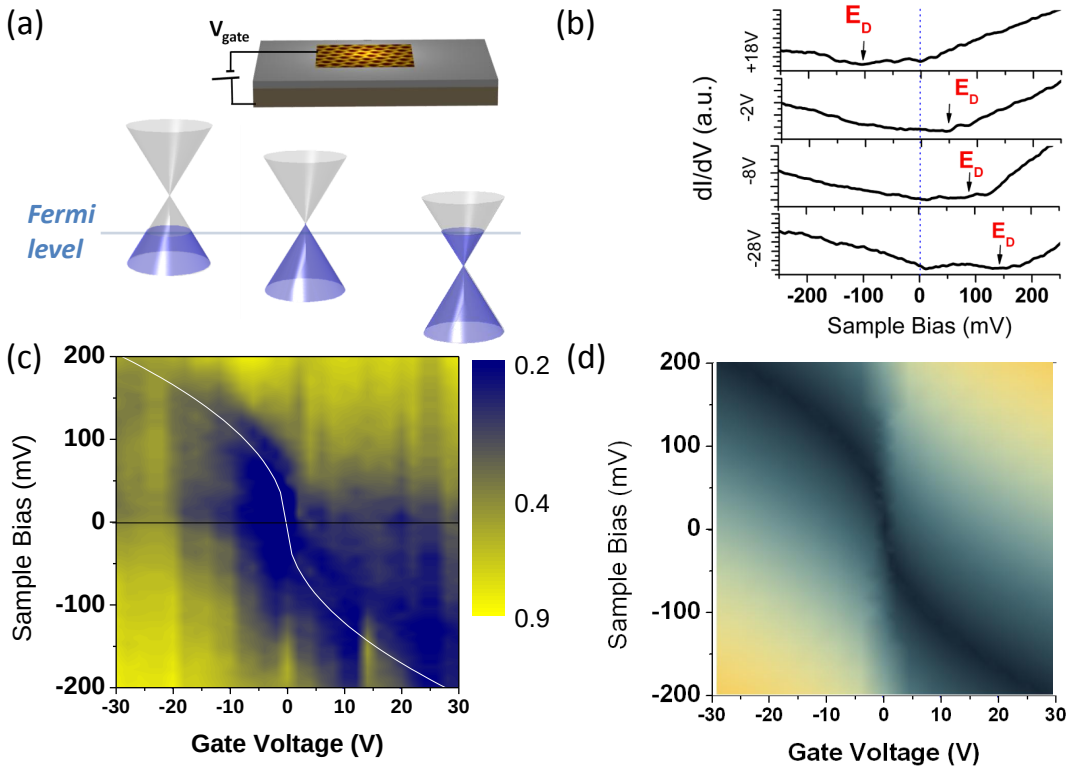

Figure 3.6: (a)Schematic of electrostatic gating in graphene devices. By applying a gate voltage V_g between the sample and Si back-gate one can induce charge carriers in graphene and move the Dirac Point relative to the Fermi level. (b) STS spectra of graphene on BN at different gate voltages. The Dirac Point indicated by E_D moved relative to the Fermi level (vertical blue line). (c) Intensity map of STS spectra taken at different gate voltages. The black horizontal line indicates the Fermi level. The white curved line represents the theoretical fit to the position of the Dirac Point. (d) Simulation of the expected STS map as a function of gate voltage, assuming that the spectrum is V-shaped.

at gate voltages $V_g = -28V, V_g = -8V, V_g = -2V, V_g = +18V$ is presented in Figure 3.6(b). While at the negative gate voltages The Dirac Point was at positive sample bias, meaning the sample is hole doped, at positive gate voltages the Dirac point is at negative sample bias, below the Fermi level which means the sample is electron doped.

Such spectra were taken at gate voltages between -30V and 30V and plotted as a map where the intensity represents the value of dI/dV as shown in Figure 3.6(c). Theoretically the Dirac Point according to Equation 3.5 would be found

on the white line superposed with the plot. A region of low values of dI/dV does follow the white line indicating that the Dirac Point does indeed move with respect to the Fermi level(black line) as gate voltage is applied to the sample. A simulation of this situation assuming each spectrum is a V-shape line (modeled as f(x)=$|x|$) is presented in Figure 3.6(d), in agreement with the experimental map in (c).

Chapter 4
Landau levels in graphene

In the presence of a magnetic field, B, normal to the plane, the energy spectrum of a 2D electron systems breaks up into a sequence of discrete Landau levels (LL). For the non-relativistic case realized for example in the 2D electron system on helium [4] or in semiconductor heterostructures [84], the Landau level sequence consists of a series of equally spaced levels similar to that of a harmonic oscillator: $E = \hbar\omega_c(N + 1/2)$ with the cyclotron frequency $\omega_c = eB/m^*$, a finite energy offset of $1/2\hbar\omega_c$, and an effective mass m^*. In graphene, as a result of the linear dispersion and Berry phase of π, the Landau level spectrum is different:

$$E_n = \pm\hbar\omega_G\sqrt{|N|}, \omega_G = \frac{\sqrt{2}v_F}{l_B} \tag{4.1}$$

Here, $N = ... - 2, -1, 0, +1, +2...$ is the index of the Landau level, ω_G is the cyclotron energy for graphene and $l_B = \sqrt{\frac{\hbar}{eB}}$ is the magnetic length.

Compared to the non-relativistic case the energy levels are no longer equally spaced, the field dependence is no longer linear and the sequence contains a level exactly at zero energy, $N = 0$, which is a direct manifestation of the Berry phase in graphene [19]. We note that the LLs are highly degenerate, the degeneracy per unit area being equal to $4B/\phi_0$. Here B/ϕ_0 is the orbital degeneracy with $\phi_0 = h/e$ the flux quantum and $4 = g_s \cdot g_v$, where g_s and g_v (g_s=g_v=2) are the spin and valley degeneracy, respectively.

In Figure 4.1 an illustration of the quantized LL is presented. The conical dispersion of graphene in the absence of a magnetic field is transformed into a

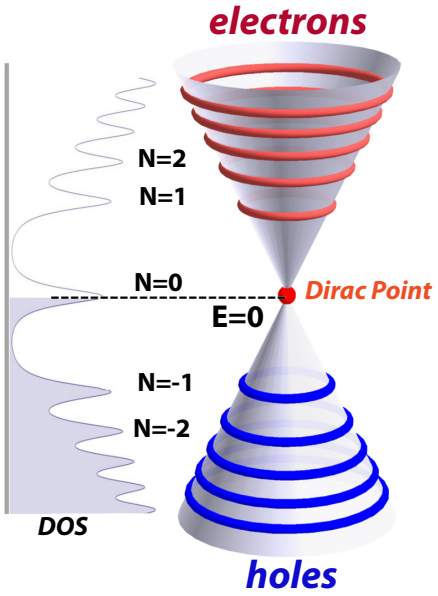

Figure 4.1: Illustration of quantized energy levels in graphene and their signature in the density of states. Right side: Dirac cone which in a magnetic field no longer has a continuum energy, but discrete levels: red rings for electrons, blue rings for holes. Left side: the vertical axis is energy; the horizontal axis is the density of states. For each Landau level there is a peak in the density of states which is broadened by electron-electron interactions in ideal systems. In the presence of disorder, the LL are further broadened. The indexes of the LLs are N=0 for the one at the Dirac point and N=+1,+2,+3... for the electron side and N=-1,-2,-3,... for the hole side.

sequence of levels corresponding to electron carriers above the Dirac point (DP) and holes below it. In the density of states, represented on the left side, a LL corresponds to a peak in the DOS. The indexes of the LLs are indicated as $N < 0$ for holes and $N > 0$ for electrons. Assuming that the Fermi level is exactly at the DP (the case of neutral graphene) the gray area in Figure 4.1 represents electronic states that are already filled.

This quantization is responsible for interesting physical phenomena such as the integer [48, 85, 86] or fractional quantum hall effect [87, 88, 89].

Experimentally, a direct way to study the quantized Landau levels is through STS as was demonstrated in early studies on HOPG [90, 91] and adsorbate-induced two dimensional electron gases (2DEGs) formed by depositing Cs atoms on an n-InSb(110)surface [92].

An alternative, though less direct, method of accessing the LLs is to probe the allowed optical transitions between the LLs by using cyclotron resonance measurements. This was done on exfoliated graphene on SiO_2 [93, 94], epitaxial graphene [95] and graphite [56]. Other indirect methods include scanning electron transistor or similar capacitive techniques [96, 97].

Landau level spectroscopy from STS measurements can be used to obtain the Fermi velocity of Dirac fermions, the quasiparticle lifetime, the electron phonon coupling, and the degree of coupling to the substrate [55, 98]. This technique was adopted and successfully implemented to probe massless Dirac fermions in other systems including graphene on SiO_2 [46], epitaxial graphene on SiC [99], graphene on Pt [100] and topological insulators [101, 102].

In this chapter we describe Landau level spectroscopy on graphene systems with different degree of disorder. We start from early attempts of investigating the LL on graphene deposited on standard SiO_2 and then describe improved experiments on graphene on graphite, chlorinated SiO_2 and graphene on BN which give access to measuring the LL sequence specific to electrons in single layer

graphene. Parts of this chapter follow closely the text in [33, 46, 69, 55].

4.1 Landau Levels in graphene on disordered SiO_2

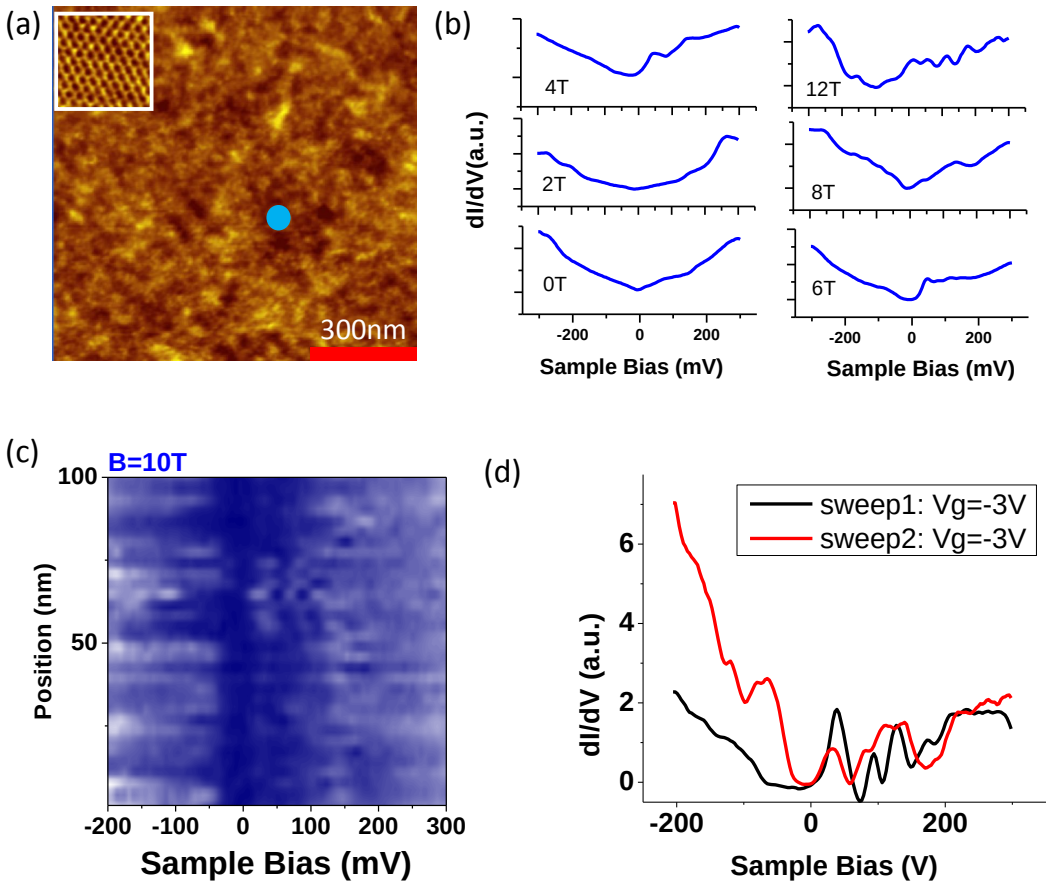

Figure 4.2: (a) STM topograph of graphene on standard SiO_2. Inset: atomic resolution image showing the hexagonal structure specific to single layer graphene. (b) STS spectra taken at the position indicated by the blue dot, for magnetic fields B=0T to B=12T. (c) STS map along a vertical line crossing the center of (a) at 10T. The intensity is dI/dV. (d) Illustration of the hysteresis when changing gate voltage. STS spectra at 10T and $V_g = -3V$ before and after sweeping the gate voltage to more negative values.

The quality of the substrates that supports graphene is crucial for the behavior of the charge carriers. Many of the initial STM experiments on graphene placed on regular thermally grown SiO_2 do show the expected honeycomb structure for graphene as discussed in the previous chapter, however the electronic properties

are strongly affected by the substrate. This is the case also when graphene is placed in a magnetic field. If the disorder is too strong the Landau levels will broaden significantly and overlap such that one cannot distinguish a sequence specific to single layer graphene.

This was the case for the samples investigated on thermally grown SiO_2 and a typical situation is presented in Figure 4.2. The topography of the investigated area is presented in Figure 4.2(a) where the inset shows typical atomic resolution image in that region, confirming the presence of a single layer graphene. Furthermore, spectroscopy data was recorded at the position indicated by the blue dot. The field dependence of the spectrum is shown in Figure 4.2(b). One can observe peaks that develop once the field is increased. However it is not possible to identify a single layer graphene sequence not even when the field is B=12T. To illustrate how the spectrum varies for different positions, Figure 4.2(c) shows a map of the spectra taken on a vertical line crossing the center of the image in Figure 4.2(a) for B-10T. The bright color corresponds to high value of the dI/dV and the dark color to low values. The lack on discrete levels (peaks in the spectrum) and the spatial inhomogeneity along the 60nm line across the sample further illustrates the effect of disorder on the LL sequence.

Another characteristic of the poor quality samples is the gate hysteresis, meaning that a spectrum taken at the same gate voltage in the same position will not remain the same if the gate voltage was changed in between. Such a situation is illustrated in Figure 4.2(d), where the black curve was taken first at $V_g = 3V$ followed by ramping the gate voltage to more negative values and then returning at $V_g = -3V$, the obtained spectrum is the red curve. Such hysteresis is also present in transport experiments [103] and usually explained as charges (from either fabrication residues, substrate, leads) being attracted/repelled from graphene while sweeping the gate. Similar data to the one presented in this section was reported in [79].

4.2 Landau Levels in graphene on improved quality SiO_2

As the potential found on standard SiO_2 substrates was too large to allow observation of LLs by STS even in the highest magnetic fields, further improvement of the substrate was needed. One procedure that was demonstrated to dramatically improve sample quality is to remove the SiO_2 substrate under the graphene which becomes suspended [104, 105, 87, 88]. However, such samples are fragile and small, so studying them using scanning probes is challenging. In addition, in these samples, in the absence of Van der Waals forces between the graphene and substrate, the electrostatic and Van der Waals forces between tip and sample can induce vibrations in the graphene membrane and this can lead to unstable STM junction [106]. To prevent strong tip sample interaction and minimize vibrations of the suspended graphene, we designed small devices ($< 1\mu m$) with triangular shape as shown in Figure 4.3. For such triangles, at room temperature, it was possible to obtain STM topographic maps such as the one presented Figure 4.3(b).

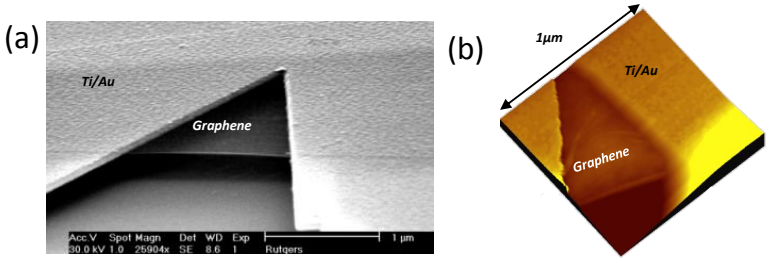

Figure 4.3: (a) SEM image of a suspended graphene triangle. (b) Room temperature STM image of the same suspended device.

Therefore, exploring ways to improve the substrate is of interest. In the semiconductor industry it is known that the quality of SiO_2 can be greatly improved using dry oxidation in the presence of chlorine. This process reduces the number of trapped charges in the oxide, improving the uniformity and quality of the insulator [107, 108, 109, 110]. When using such substrates treated by chlorination, the STM and STS measurements show that it is possible to see well defined quantized levels for high enough magnetic fields [46]. While these samples allow

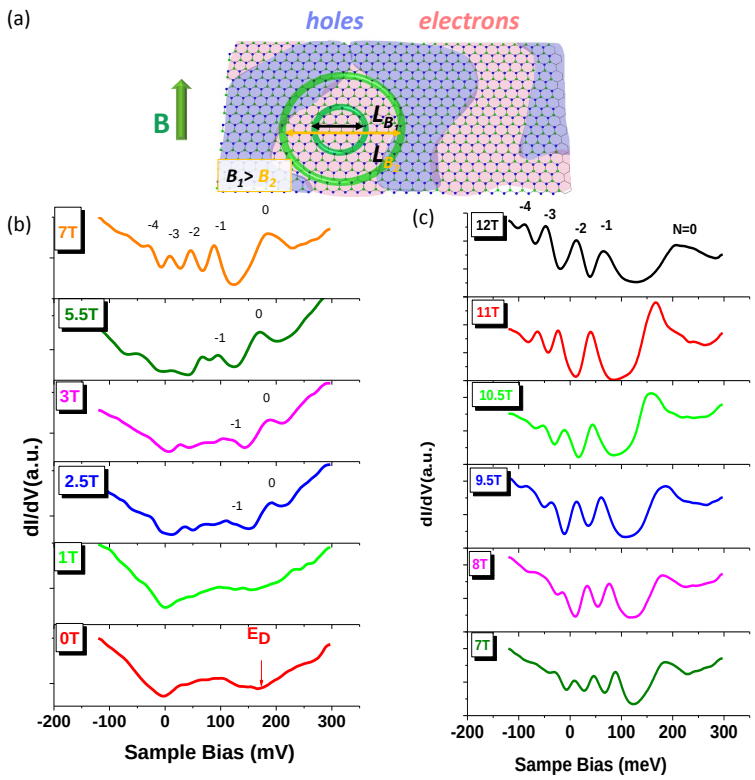

Figure 4.4: (a) Illustration of the competition between the two length scales: electron-hole puddles (disorder) and magnetic length. For a low field B_2 the magnetic length will probe both electron and hole areas, but when the field is higher B_1 the magnetic length will become smaller than the size of a puddle. (b) STS at different magnetic fields for graphene on chlorinated SiO_2.

observation of one of the hallmarks of single layer graphene, the unique sequence of LL and with a level at the Dirac point, given the broadening of the LLs and the deviation from V-shaped zero-field density of states these samples are not yet ideal.

STS in zero field was used to give an estimate of the average length scale of disorder, the electron-hole puddle size, $d \approx 20nm$ [46]. In order to observe well defined levels, the magnetic length should be at most $(d/2) \approx 10nm$, corresponding to a magnetic field $B = 6T$. This idea is illustrated by Figure 4.4(a) where a semi-classical cyclotron orbit of size l_B is shown for two different magnetic fields, $B_1 > B_2$ so that in the case of the larger field it becomes smaller than the typical size of the disorder puddle.

In Figure 4.4(b) the STS data taken for graphene on chlorinated SiO_2 is plotted as a function of magnetic field. It shows how indeed, for smaller fields, below 6T, the levels are not well defined, while above 6T they become clearly defined. The presence of the $N = 0$ Landau level at energies $\approx 200meV$ confirms the fact that the origin of the dip observed in the absence of magnetic field and marked as E_D in Figure 4.4(b) is the Dirac Point. The slight variation in the position of $N = 0$ LL could be due to changes of the position of the tip after changing the field (estimated within a few nm), but it can also be an effect of pinning of a LL at the Fermi level as it will be explained in detail in Chapter 5.

From the measured sequence of LLs one can extract the Fermi velocity of the carriers in the following way: according to Equation 4.1 the energies of the levels depend linearly on the product $sgn(N)\sqrt{|N|B}$. We consider all the LL peaks for all fields and indexes and we plot them versus $sgn(N)\sqrt{|N|B}$ and thus from the slope of the linear fit we can directly extract the Fermi velocity.

The Fermi velocity obtained in such a way from the data presented in Figure 4.4 is $v_F = (1.07 \pm 0.02) \cdot 10^6 m/s$ (Figure 4.5(a)) and varies by $5-10\%$ depending on the position on the sample. This value is consistent with other measurements of the Fermi velocity in graphene on SiO_2.

In such samples it is expected that the levels are broadened by disorder [111, 112, 113]. The measured width of the levels is typically $\gamma \approx 20 - 30meV$ (Figure 4.5(b)). Compared to the results obtained for graphene on the surface of graphite [69] and for epitaxial graphene on SiC [99] the levels are broader and their width varies with position, suggesting a shorter carrier lifetime due to extrinsic scattering mechanisms such as trapped charges, ripples, etc. The typical linewidth for LLs with $N \neq 0$, $\gamma \approx 20 - 30meV$, corresponds to the carrier lifetimes $\tau \approx \frac{\hbar}{\Delta E} \approx 22-32fs$ which is consistent with values found by other methods in nonsuspended graphene samples [93, 96, 97].

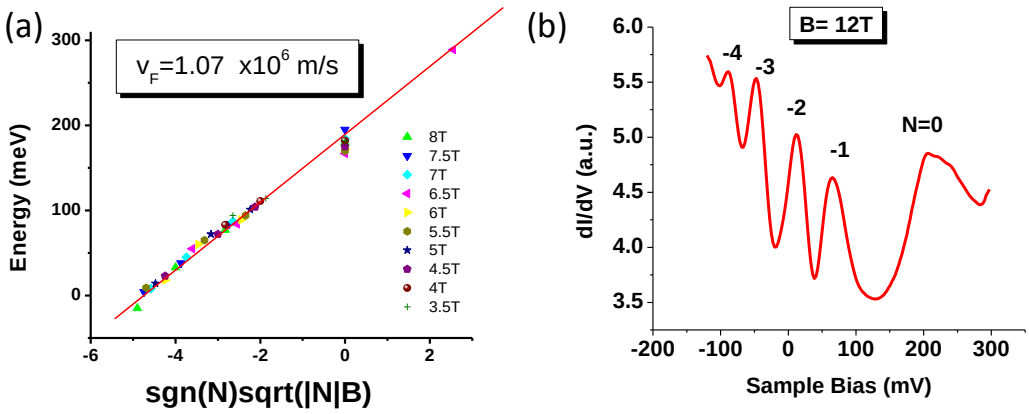

Figure 4.5: (a) Energies of the LL peaks for the data in Figure 4.4 plotted versus $sgn(N)\sqrt{(|N|B)}$. The straight line fit gives the Fermi velocity $v_F = 1.07 \times 10^6$. (b) Example of a STS spectrum taken at $B = 12T$ showing the N=0 at $\approx$ 200meV followed by the hole side of the spectrum $N = \pm 1, \pm 2....$

4.3 Landau Levels in almost ideal graphene

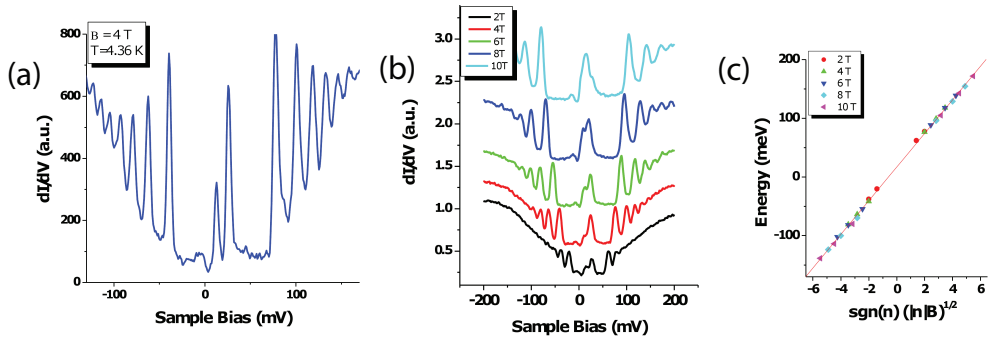

Figure 4.6: (a) STS spectrum of graphene on graphite showing the presence of Landau levels. (b) The evolution of the LL with magnetic field. (c) The energy dependence of the LL on the reduced parameter $sgn(N)\sqrt{|N|\,B}$ [69].

Graphite provides a much better substrate for STM studies of graphene in the sense that it is metallic and therefore can screen the charge inhomogeneities. On the surface of graphite it is possible to identify graphene flakes that are, due to underlying defects of the crystal, mechanically and electronically decoupled from the underlying graphite layers [69, 90].

The measured LLs in magnetic field in such a sample [69] are indeed very

sharp at already low fields attesting to the quality of such samples.

Figure 4.6(a) shows the STS spectrum on a graphene flake decoupled on the surface of graphite, in $B = 4T$, having very sharp LL peaks. their field dependence is presented in Figure 4.6(b). The dependence on the scaling parameter is in Figure 4.6(c).

Comparing to Equation (4.1), the slope of the line gives a direct measure of the Fermi velocity, $v_F = 0.79 \cdot 10^6 m/s$. This value is 20% less than expected from single particle calculations and, as discussed below , the reduction can be attributed to electron-phonon interactions.

Electron-phonon interaction and velocity renormalization. The basic physics of graphene is captured by the simple tight-binding model, but many-body effects are often not negligible. Theoretical calculations show that the electron-phonon (e-ph) interactions can introduce additional features in the electron self-energy, leading to a renormalized velocity at the Fermi energy [114].

Landau level linewidth and electron-electron interactions The line-shapes of the LLs for the case of graphene on graphite were found to be Lorentzian rather than Gaussian [69], suggesting that the linewidth reflects the intrinsic lifetime rather than disorder broadening. Furthermore, looking closer at the linewidth of the LLs in Figure 4.6(c), it is found that the width increases linearly with energy. This dependence is consistent with the theoretical predictions that graphene displays a marginal Fermi liquid behavior: $\tau \propto E^{-1} \approx 9ps$ [115]. Lifting of the LL degeneracy was observed in quantum Hall effect measurements on the highest quality suspended graphene devices [87, 88] and in STM experiments on epitaxial graphene on SiC [116].

To further illustrate the fact that such graphene flakes on graphite samples are very homogeneous one can analyze the variation of the Dirac Point and of the Fermi velocity across the graphene flake presented in Figure 4.8 (a). STS spectra were recorded on a grid of 64 $\times$ 64 points in region G and from a fit

similar to Figure 4.6 (c) the Fermi velocity and the position of the Dirac point with respect to the Fermi level were extracted. The results are presented in Figure 4.7. In Figure 4.7(a) each pixel represents the value of the shift of the DP and the corresponding histogram is shown in Figure 4.7(b). With the exception of a few scattered points (where the noise in spectrum prevented the fit of the LL) the plot distribution centered around the value $|E_D - E_F| \approx 22\ meV$ with a spread $\pm 5meV$ that is comparable to the error bar from the fit.

The Fermi velocity distribution across the sample is shown in Figure 4.7(c) and the corresponding histogram in 4.7(d). In this case, similarly to the Dirac Point, the variation in the Fermi velocity across the sample is within the error bar.

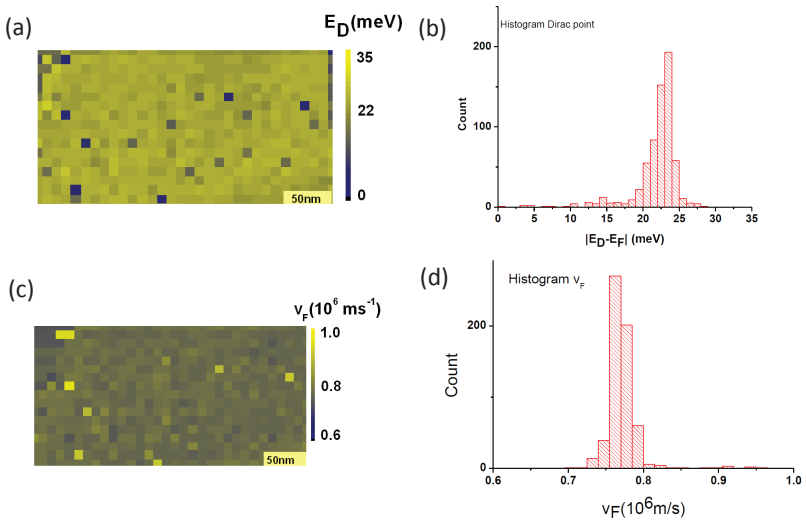

Figure 4.7: (a) Map of the Dirac point on graphene on graphite [55]. (b) Histogram of the values of Dirac point in (a). (c) Map of the Fermi velocity on graphene on a graphite substrate [55]. (d) Histogram of the velocities in (c).

4.4 Effects of interlayer coupling

For graphene flakes on graphite one can also address the effect of interlayer coupling in regions where the graphene flakes are weakly coupled to the substrate. It was found that the LL spectrum of graphene which is weakly coupled to a

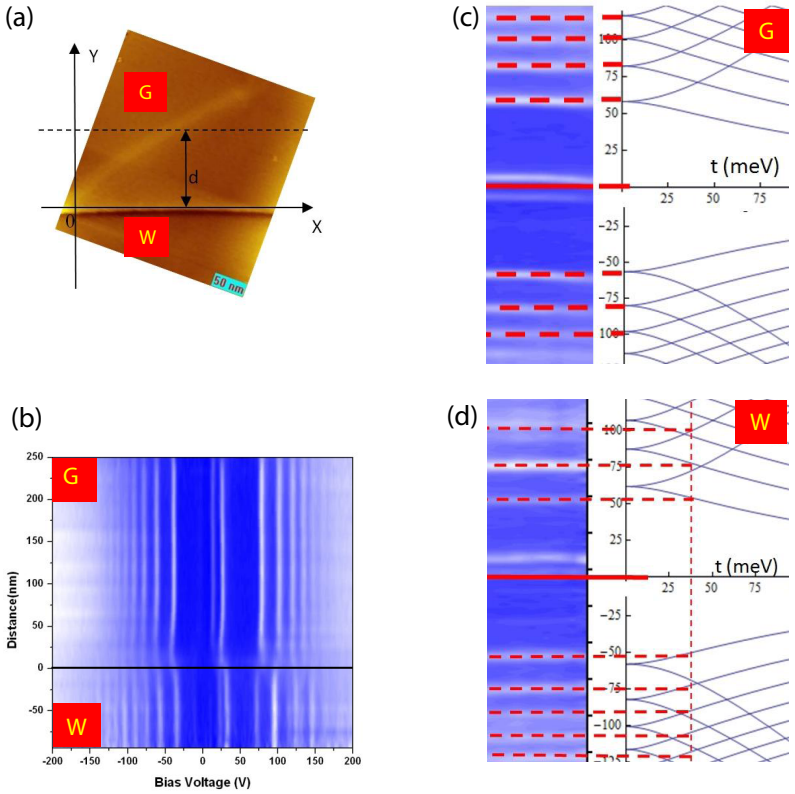

Figure 4.8: (a) STM image showing two distinct regions: G- where the graphene flake is decoupled from graphite; W- where the graphene flake is weakly coupled to the graphite substrate. (b) The evolution of the Landau levels from region G to region W. The vertical axis is the position where the spectrum is measured indicated by d in (a); the horizontal axis is the sample bias. (c),(d) Fits of the LLs in (b) to the theoretical model [98] for no coupling (c) and weak coupling (d) [55].

graphite substrate strongly depends on the degree of coupling [55].

In Figure 4.8(a) the topography image shows two regions: G, where the top layer is decoupled and displays signatures of a single layer graphene and below it, a different region, W, where there is weak coupling to the underlying graphite substrate. We chose a coordinate system (Figure 4.8(a)) with the abscissa coinciding with the ridge and the ordinate representing the distance from it. In this representation all the points in region G are above the x axis and points in region W are below it. We followed the spatial evolution of the Landau level sequence

across the flake, from region G to region W as shown in Figure 4.8(b). The spectral features in region B below the ridge show neither characteristics of single layer graphene nor those of graphite, but as we show below, they are consistent with a very weakly coupled layer.

The Landau levels in region G correspond to decoupled single layer graphene [69], as discussed above. In contrast the Landau levels in region W are slightly shifted towards the Dirac point and their level index dependence is not the one expected for either bilayer or multilayer graphene.

To understand the behavior of the level sequence in region W we compare to calculations by Pereira et al.[98], showing the evolution of the Landau level sequence of a bilayer as a function of interlayer coupling strength. They find that as the coupling strength is increased the spectrum evolves from that of a single uncoupled graphene layer into a sequence where each Landau level (except $N = 0$) splits as the twofold degeneracy is lifted with increasing coupling strength. For any given coupling strength this gives rise to a unique Landau level sequence. We used this model to interpret the Landau level sequence in region W. In Figure 4.8(c) and (d) we compare the experimental data to predictions from this model. Here the vertical axis is energy and the horizontal axis on the right is the interlayer coupling, t. In [98], the evolution of Landau level energies with interlayer coupling depends on the Fermi velocity and on the magnetic field.

In this data the magnetic field was 4 T and the Fermi velocity and coupling constant were adjusted to obtain the best fit between the measured Landau level sequence and the model. Figure 4.8(c), we show that the Landau level sequence in region G matches that of a decoupled layer (or zero coupling in the model) and Fermi velocity of $v_F \approx 0.8 \times 10^6 m/s$. In Fig. 4(d) the sequence in region B is shown to match the theoretical model for interlayer coupling $t = (40 \pm 5) meV$, one order of magnitude smaller than the coupling constant in graphite. The Fermi velocity used was $v_F \approx 0.8 \times 10^6 m/s$. We therefore conclude that the anomalous

Landau level sequence in region B reflects a small but finite interlayer coupling.

Chapter 5
Carrier density dependence of the LL spectrum

Due to its band structure, in particular the electron-hole symmetry, graphene shows an ambipolar electric field effect. The evolution of the electronic spectrum with carrier density is therefore accessible for STS experiments on graphene flakes deposited on the insulating SiO_2 surface. Studying this dependence in the presence of a magnetic field is closely related to quantum Hall physics. The ability of STS to access both electron and hole states beyond the states close to the Fermi level makes it a particularly powerful technique, complementary to electrical transport, for gaining a deeper understanding the physical properties that govern the two dimensional electron system in the quantum Hall regime.

Figure 5.1 illustrates the main characteristics of the data discussed in this chapter and represents a guide for understanding the presentation of the experimental results. Figure 5.1(a)-(f) shows a sequence of simulated DOS $\propto dI/dV$ spectra for a fixed energy range as the number of carriers in the system is changed using a back gate. In this particular case the parameters were chosen such that $B = 12T$,$v_F = 1.2 \times 10^6$, $c = 115aF/(\mu m)^2$. The horizontal line at E=0 meV is the Fermi level which is at $V_b = 0V$ in an STM experiment. For each of the spectra, the region that was shaded in gray highlights the fact that they are below the Fermi level, thus they are filled electronic states.

Figure 5.1(g) is an intensity map having as vertical axis the energy, as horizontal axis the bias voltage applied and as intensity the value of dI/dV. Such a map traces the evolution of the Landau levels which are bright lines (peaks

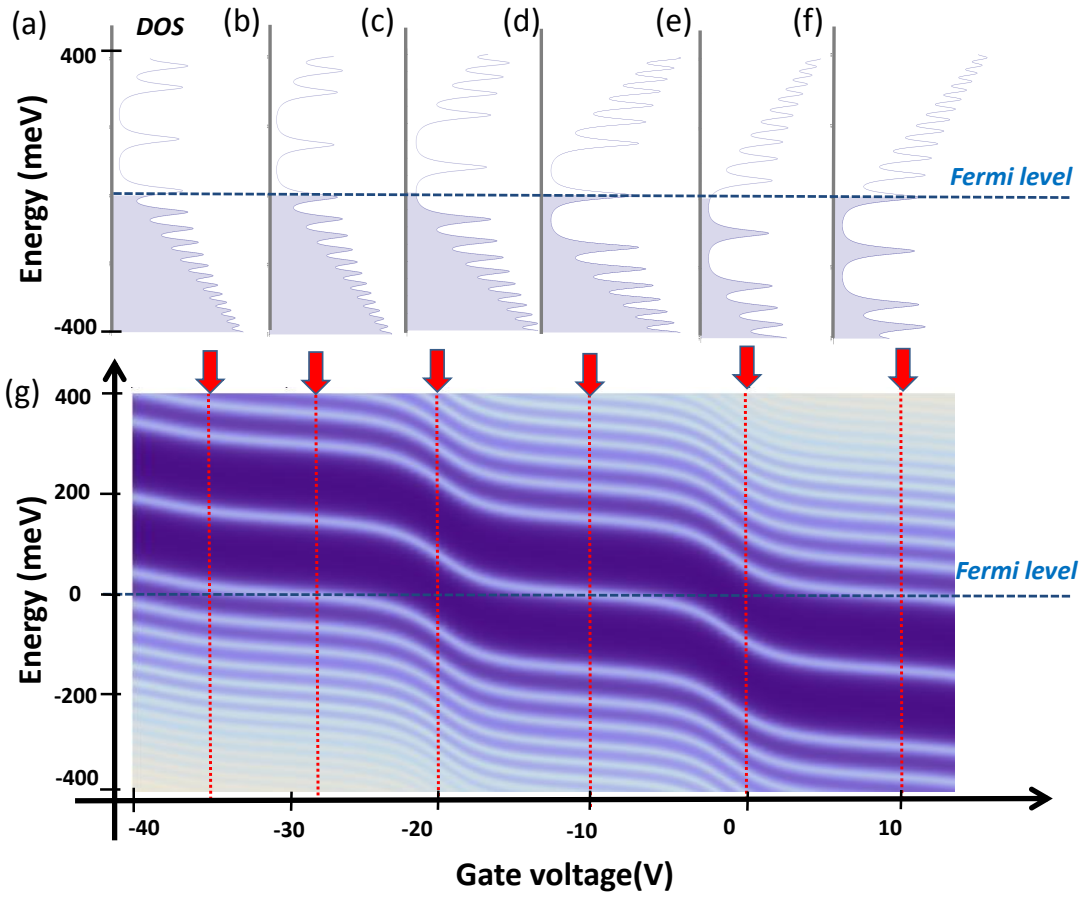

Figure 5.1: Schematic of Landau level spectrum behavior as a function of carrier density. (a)-(f) Simulated DOS versus energy spectra for different gate voltages. The horizontal line indicated the Fermi level. The shaded gray area shows the filled states of the spectrum while the upper part are the unfilled states. (g)Intensity map of DOS plots at different gate voltages. The particular spectra chosen for (a)-(f) are marked by vertical red dashed lines.

in an individual spectrum) with the change in the carrier concentration. Again as above, the Fermi level is indicated by a horizontal dashed line. The vertical dashed lines are the particular spectra that were plotted in the top panel.

Previous such measurements were done in GaAs samples by a complex spectroscopy technique: time domain capacitance spectroscopy [6]. In those experiments, on very high mobility samples, the equidistant LL spectrum of a 2DEG was observed as well as signatures of many-body interactions. Also, in graphene exfoliated on SiO_2, Jung et al. [77] reported gate mapping measurements of the

tunneling spectroscopy in disorder dominated samples.

In this chapter the results obtained by tracing the LLs with changing the carrier concentration for graphene on both SiO_2 and BN are discussed. Parts of this chapter follow closely the text in [33, 46, 69, 55].

5.1 The staircase-like pattern

Qualitatively, one can understand the overall step-like features in the map of Figure 5.1(g) (plateaus followed by abrupt changes in slope) as follows: the LL spectrum contains peaks, corresponding to high DOS, separated by regions of low DOS. It takes a large change in the charge carrier density to fill the higher DOS regions - therefore plateaus appear; at this point the Fermi level is pinned to the particular Landau level being filled. On the other hand, filling the regions of low DOS in between the LLs does not require much change in carrier density - therefore an abrupt change in slope appears. For broad Landau levels the DOS in between the peaks is larger, thus smearing the step-like pattern.

This is readily illustrated by looking at Figure 5.1(a)-(f). Figure 5.1(a),(b) correspond to the plateau region of Figure 5.1(g) when the LL $N = +1$ is being filled. Figure 5.1(c) represents filling the states between the $N = +1$ and $N = 0$ which gives rise to the abrupt jump in Figure 5.1(g). Figure 5.1(d) illustrates the doping level at which the N=0 LL is exactly half filed and it is in the middle of the plateau in the map. In Figure 5.1(e) the states between $N = 0$ and $N = -1$ LL are just finish being filled and $N = -1$ LL is starting to be filled.

In this chapter the simulations done to understand the expected pattern of the LL evolution as the carrier concentration is changed was following the general idea presented below. Each Landau Level is assumed to be a Lorenzian with lineshape γ centered at energy positions given by graphene LL sequence (in units of cyclotron energy $\omega = \hbar\frac{\sqrt{2}v_F}{l_B} = v_F\sqrt{2e\hbar B}$): $E_i = Sgn(i)\sqrt{|i|}$. The density of

states (DOS) is a sum of all the Lorenzians (for numerical calculation purposes a cutoff was chosen at i=50)

$$DOS(x) = \sum_{i=-50}^{+50} \frac{2}{\pi\sqrt{3}} \frac{1}{\gamma} \left[1 + \frac{4}{3} \left(\frac{x - E_i}{\gamma} \right)^2 \right]^{-1} \tag{5.1}$$

The number of electrons one can accommodate in a Landau Level is the degeneracy of each state times the total number of states (area under the Lorenzians). Therefore the number of electrons up to an energy is

$$n(x) = \frac{4}{\pi} \left(arctan \left(\frac{2}{\sqrt{3}} \frac{x - E_i}{\gamma} \right) - arctan \left(\frac{2}{\sqrt{3}} \frac{0 - E_i}{\gamma} \right) \right) \tag{5.2}$$

The reverse question is: given a certain electron density , n, what is new position of the Fermi level, μ? This can be answered by numerically solving the reverse of the equation above: $\mu(n) = x$ where x is a solution of $n(x) = n$.

5.2 Evolution of the LL spectrum with carrier concentration

On the samples with graphene flakes on the surface of chlorinated SiO_2, where one could identify a sequence of LLs and which did not show gate hysteresis it was possible to measure the dI/dV spectrum as a function of gate voltage. The procedure for such measurement was: the STM tip was raised above the surface by $\approx 1\mu$. Then, a particular gate voltage was applied between the Si back gate and graphene and after a few minuted the STM tip was lowered again. This procedure minimized the chance for electrostatic interaction between tip and sample [117] which could lead to a fatal tip crash.

Figure 5.2(a) shows the map of STS data taken at B=12T as a function of gate voltage. As described above, each vertical line is a spectrum at a particular gate voltage V_G and the intensity of the plot represents the value of the dI/dV. The lighter color corresponds to the peaks in the spectrum. The vertical axis

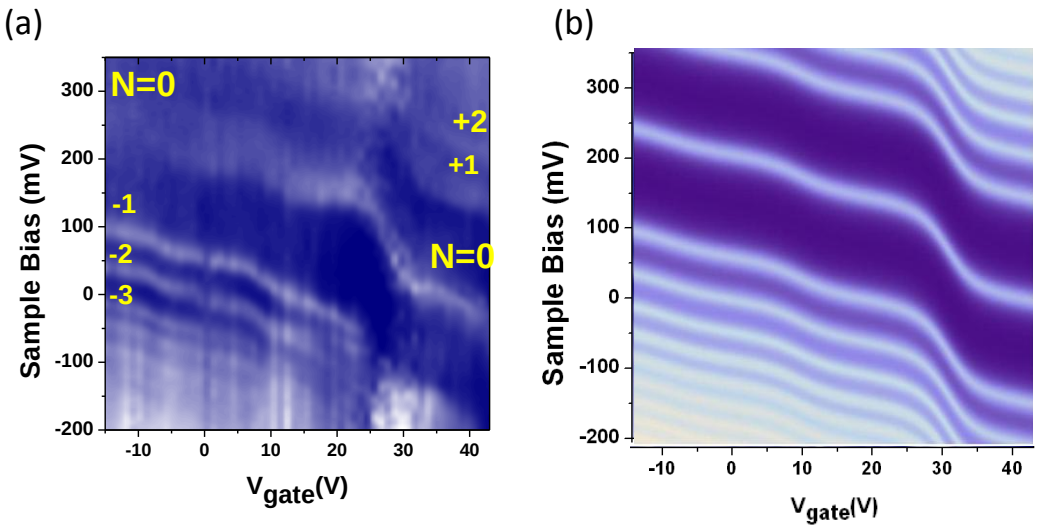

Figure 5.2: (a) Map of the dI/dV spectra as a function of gate voltage at $B = 12T$. The respective LLs are marked as $N = 0, \pm 1, \pm 2, etc.$. (b)Simulation of the data in (a).

is the sample bias and the horizontal axis is the gate voltage. The gate voltage was varied in the range $-15V < V_G < +43V$ corresponding to carrier densities: $3 \times 10^{12} cm^{-2} > n_c > -0.5 \times 10^{12} cm^{-2}$. In the spectrum taken at V_G=-15V a very faint N=0 level is seen at $\approx 240meV$. Because the sample was hole doped at neutral gate voltage already, in the energy range that we probe, we only measure the Landau levels corresponding to hole states: $N = -1, -2, -3....$ At higher gate voltages though, for $V_G > 40V$ the levels corresponding to electron states $N = +1, +2, +3...$ also become visible. The plateaus in the map, where the LLs are pinned to the Fermi level are visible, especially the one corresponding to $N = 0$. The others are slightly smeared because of the broadening of the LLs.

A simulation considering the LL broadening and using v_F =(1.16 $\pm$ 0.02)x10^6 m/s is plotted in Figure 5.2(b) and shows good agreement with the measured data in Figure 5.2(a) within the gate voltage range measured.

Probing the shape of the Dirac cone

In contrast to electrical transport measurements that typically probe states near the Fermi surface, and Angle-resolved photoemission spectroscopy(ARPES)

which only probes filled states, STS can access both filled and empty states. Therefore, in a magnetic field, through LL spectroscopy one can, in principle, probe the full shape of the Dirac cone in the measured energy range. For that ideally at already low magnetic fields, the LLs would be well separated so that many of them can be resolved and from their separation in energy the shape of the Dirac cone can be constructed.

In our experiments we typically need high fields to resolve LLs up to index $N = \pm 4$. Thus we cannot resolve the shape on the cone in energy, but if we assume the dispersion is conical we can probe the slope of the cone. This way we investigated the slope as a function of carrier concentration by measuring the Fermi velocity from the LL sequence as a function of doping. Within the investigated range of charge carrier density ($3 \times 10^{12} cm^{-2} > n_c > -0.5 \times 10^{12} cm^{-2}$), we found that closer to the Dirac point, the velocity increases by $\approx 25\%$ as seen in Figure 5.3(a).

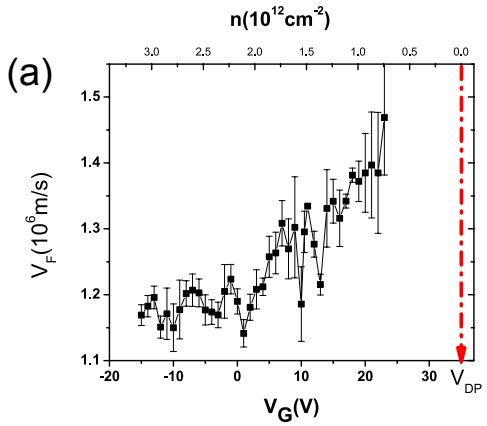

Figure 5.3: (a) Dependence of the Fermi velocity on the gate voltage as extracted from Figure 5.2 (a). The Dirac Point is marked by the red dashed line.

At low carrier density the effects of electron-electron interactions and reduced screening on the quasiparticle spectrum are expected to become important. The observed increase in the Fermi velocity is consistent with a renormalization of the Dirac cone close to the neutrality point due to electron-electron interactions [118, 119]. If the random potential is further reduced such that LL can be observed

already in small fields, the fact that the spacing between the levels is smaller will make it possible to probe the reshaping of the cone with higher accuracy.

A similar result was obtained by Elias et al. on suspended graphene samples by measuring the amplitude of the Shubnikov de Haas oscillations as a function of temperature [120]. We point out that this is a slightly different measurement in that the carriers probed are always at the Fermi level.

5.3 Connection to the quantum Hall effect

As described before, STS in magnetic field and in the presence of a back-gate probes the Landau level spectrum as a function of carrier density. The integer quantum Hall effect (IQHE) measured in electrical transport experiments in two dimensional electron systems in the presence of a magnetic field has its origin in the existence of the LL spectrum with its peaks and valleys. So what is the connection between the two?

A typical IQHE measurement in a hall bar configuration [86], as sketched in Figure 5.4(b) top, measures the Hall (transverse) resistance R_{xy} and the longitudinal resistance R_{xx} while varying the filling factor, ν.

$$\nu = \frac{n \cdot h}{e \cdot B} \tag{5.3}$$

where n is the the carrier density, B the magnetic field, h the Planck constant and e the electron charge.

The data in Figure 5.4(b) shows the IQH measurement with a 4-lead configuration on a device that was prepared by transferring graphene on BN. The mobility of this particular device at room temperature was $\mu > 50 \times 10^3 cm^2 (Vs)^{-1}$ which is approximately an order of magnitude higher than on typical graphene on SiO_2 devices. It is because of such high mobility that in a magnetic field as low as $B = 2T$, for which the LL separation is $\approx 50meV$, one can observe quantized

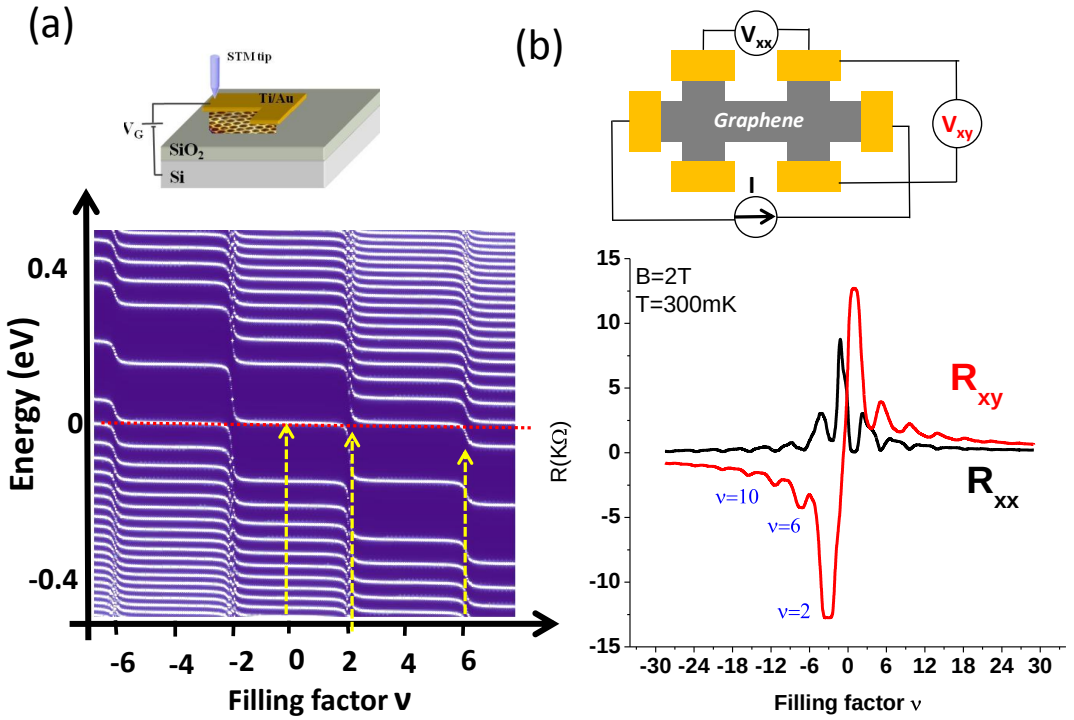

Figure 5.4: . (a) Top: Schematic of an STS experiment in the presence of a back gate. Bottom: Simulated map of the STS spectra as a function of filling factor ($B = 12T$). The arrow point to examples of spectra at different filling factors that are often seen in transport experiments. (b) Top: Schematic of a typical Hall bar configuration in a 4-lead electrical transport measurement probing the IHQ effect in graphene. With a current source a current I is passed through the graphene sample the transverse resistance is R_{xy} and the longitudinal resistance is R_{xx} are obtained from the respective voltages $R_{xy} = \frac{V_{xy}}{I}, R_{xx} = \frac{V_{xx}}{I}$. Bottom: IQH measurement at $B = 2T$ and $T = 300mK$. The plateaus in R_{xy} corresponding to $\nu = 2, 6, 10$ are highlighted.

plateaus.

In connection to the LL measured by an STS experiment, qualitatively one can understand the features measured in the transport experiments as follows:

When the filling is such that the Fermi level lies in between two LLs - corresponding to the abrupt jumps in the STS spectra as indicated by the yellow arrow at, for example $\nu = 2$, in Figure 5.4(a), the electrons are trapped in the localized states around the impurities and they do not play any role in the conduction. At this point $R_{xx} = 0$ and R_{xy} is quantized.

When the Fermi level is at a peak of a Landau level - corresponding to the plateaus in the STS spectra in Figure 5.4(a) , the electrons occupy the percolating state across the sample so R_{xx} is finite and R_{xy} increases making the transition between the quantized plateaus of the resistance in the electrical transport experiment.

It is important to note the crucial difference between the two measurements: while the electrical transport probes the states that are close to the Fermi level for any given filling, the STS experiments give access to the full LL spectrum.

Probing electron correlation gaps in STS measurements

When the magnetic field is sufficiently high and the temperature is low, the effect of Coulomb interactions is expected to affect the electronic spectrum the two dimensional electron system.

In the best samples of GaAs the presence of correlated electron states was reported as gaps opening in the LL spectrum as a function of filling factor using time domain capacitance spectroscopy [121]. In epitaxially grown graphene samples on the surface of SiC STS experiments [116] found that the $N = 0$ level can be split into 4 levels and this was attributed to lifting of the valley and spin degeneracy. In those experiments, however the filling factor was changed only by changing the magnetic field and the lack of possibility for gating prevented the unambiguous identification of correlated electron states.

Single electron transistor experiments that measure local electronic compressibility in high quality suspended graphene samples found signatures of fractional quantum Hall states.

It is expected that for STS experiments provided that the samples are clean enough so that the LL are not significantly broadened by disorder, one can observe features of many body interactions. If we compare the numbers obtained from transport experiments for the gaps of some of the typical states, say $\nu = 1$ [52], they can be as low as a few meV, which is much lower than the typical $30 -$

$50meV$broadening of the LLs dues to disorder. Therefore, further improvement of the samples is necessary. Suspended graphene samples are one possibility as well as placing graphene on very clean BN.

5.4 From single layer to large angle twisted double layer graphene

Graphene layers stack to form graphite in the so-called Bernal stacking. If we name the two inequivalent atomic sites in the graphene lattice A and B, the top layer will have B atoms sitting directly on top of A atoms of the bottom layer and A atoms of the top layer sit above the centers of the hexagons of the graphene underneath. A system consisting of two layers of graphene in Bernal stacking, bilayer graphene, is characterized by a hyperbolic energy dispersion of its massive chiral fermions.

Bernal-stacked bilayer graphene

In the presence of a magnetic field the LL sequence for an ideal Bernal-stacked bilayer graphene is given by: $E_n = (\frac{e\hbar B}{m^*})\sqrt{N(N-1)}$ where m^* is the effective mass of the carriers, B is the magnetic field, e is the electron charge, $\hbar$ is Planck's constant and N=0,1,2,3,... . The eight fold degeneracy occurring for $N = 0, N = 1$ can be broken either by an applied electric field or by electron-electron interactions [122, 123, 124]. Experimentally, magneto-transport measurements of high quality suspended bilayer samples have revealed the presence of interaction-induced broken symmetry states [125, 126, 127].

In order to directly probe massive chiral fermions in bilayer graphene, STM/STS were performed on mechanically exfoliated graphene placed on insulating SiO_2 [128, 129]. It was found that the measured LL spectrum was dominated by effects of the disorder potential due to the substrate. The random potential creates an electric field between the two layers which results in locally breaking the LL

degeneracy and a LL spectrum that is spatially nonuniform [129]. Therefore, in order to access the intrinsic properties of bilayer graphene, an improvement of samples that can be measured by STM/STS is necessary .

Twisted graphene stacks

As will be discuss in detail in Chapter 7, because the coupling between graphene layers has a great influence on their electronic properties, twisting bilayer graphene away from the Bernal stacking can change its electronic properties dramatically. For large angles the system can maintain the electronic properties of single layer graphene, while Fermi velocity renormalization and other effects can occur for smaller rotation angles. With the new sample fabrication advances of transferring layers on graphene individually and positioning them in the desired spot on the sample it is possible to experimentally explore the electronic properties of stacks of graphene layers.

We have prepared graphene samples that have the following configuration (Figure 5.5(a)): flakes of BN were mechanically exfoliated onto a $Si/Si0_2$ wafer. Then one layer of graphene was transfered on top (G_1) and an additional one was then transfered on the first one (G_2). The optical microscope image together with the corresponding sketch are shown in Figure 5.5(b),(a). The data presented here were taken on the two layers G_1+G_2 on the BN, marked by the red rectangle *Position 1* and on the single layer G_2 on BN, marked by the blue rectangle *Position 2*. In both regions, in the presence of a perpendicular magnetic field $B = 10T$, one can measure quantized Landau levels and by tuning the gate voltage the dependence of these levels with carrier concentration was studied.

Figure 5.5(b) shows the map obtained for the case of *Position 1*. The Fermi level is indicated by the horizontal black line. Interestingly, in this region the LL sequence is the one expected for a single layer graphene with a Fermi velocity that is $v_F = 1.2 \times 10^6 m/s$. However, within the gate voltage range (-20V,30V) only the LL $N = 0$ and the localized states around it are filled. In order to reproduce this

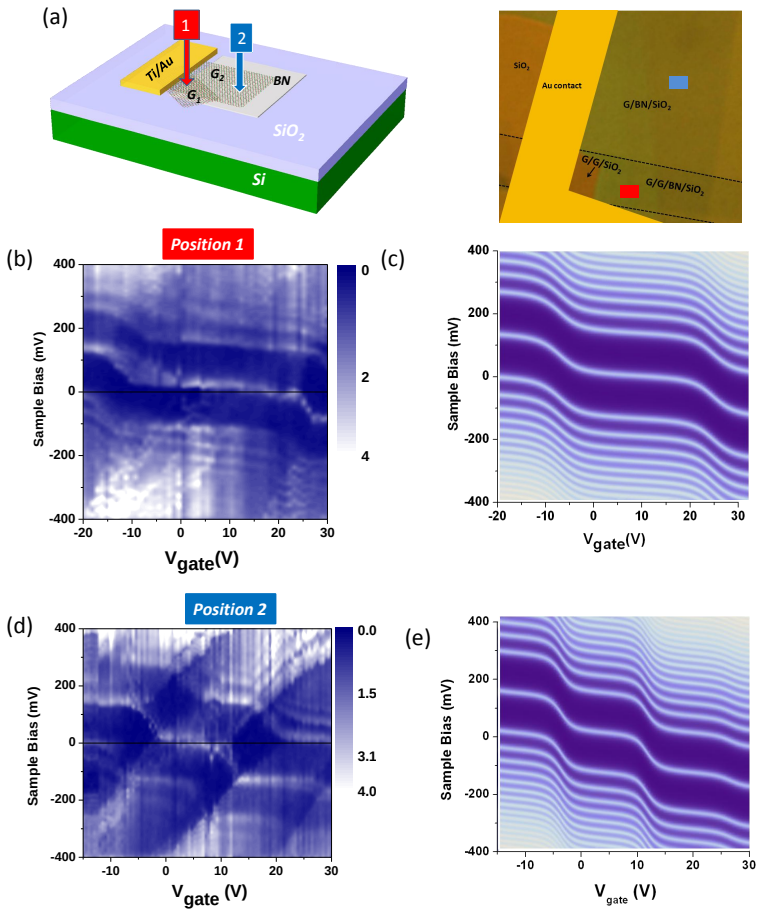

Figure 5.5: (a) Left: Schematic of the sample investigated together with the two cases discussed: Position 1- bilayer graphene G1+G2 and Position 2 - single layer graphene G2. Right: Optical microscope image of the sample. (b),(c) Gate dependence of the LL spectrum for Position 1. and its simulation . (d),(e) Gate dependence of the LL spectrum for Position 2 and its simulation.

in the simulation one can assume a single layer graphene on the substrate but use a value for an effective capacitance to the gate that is precisely half the value of the one calculated from geometrical considerations. In the simulation presented in Figure 5.5(c) the value used to reproduce the gating map was $c = 57aF/(\mu m)^2$.

Similarly to *Position*1 in region *Position*2 where a single layer graphene is placed on BN, the LL sequence is characteristic of a single layer graphene. In contrast, within the same range of gate voltage, much more of the electronic spectrum is filled. This is confirmed by the simulation which closely resembles

the data for a capacitance value $c = 115aF/(\mu m)^2$.

What this different in the effective capacitances reflects is the different degeneracies of the two systems. On one hand, in the bilayer case there are Landau levels in each layer to be filled and therefore for each LL the degeneracy becomes 4x2=8. For the single layer the LLs have the usual degeneracy 4.

Similar systems have recently been probed by electrical transport experiments [130, 131, 132]. It was found that the two layers contribute independently to the magnetoresistance. The properties of each layer could also be addressed by using both top and bottom gates [130].

5.5 Extrinsic features in the LL spectrum due to disorder

Exploring different samples and different positions within the same sample it was found that the maps of STS spectra as a function of gate voltage can show extrinsic features and thus differ from the simple model simulation previously discussed. A few examples of data taken on different samples are presented in Figure 5.6 together with corresponding simulations that reproduce the main features.

Figure 5.6(a) is a map of the STS spectrum as a function of gate voltage taken at $B = 12T$. At gate voltages $V_g < 0V$ the LL with indices $N < 0$ are being filled, followed by $N = 0$ at gate voltages $V_g > 0V$. The simulation in Figure 5.6(b) is in good agreement with the data.

The map in Figure 5.6(b) was also taken at $B = 12T$ and aside from the expected staircase patter it shows two additional features : first the $N = 0$ LL is split for all ranges of gate voltage and second a sequence of strong peaks are present in the spectrum and they cross the LL spectrum at gate voltages where the states in between the LL are being filled. The general features observed for these peaks is discussed in the next chapter. The reason for $N = 0$ being split could be related to the presence of a charged impurity as it will be discussed in the next

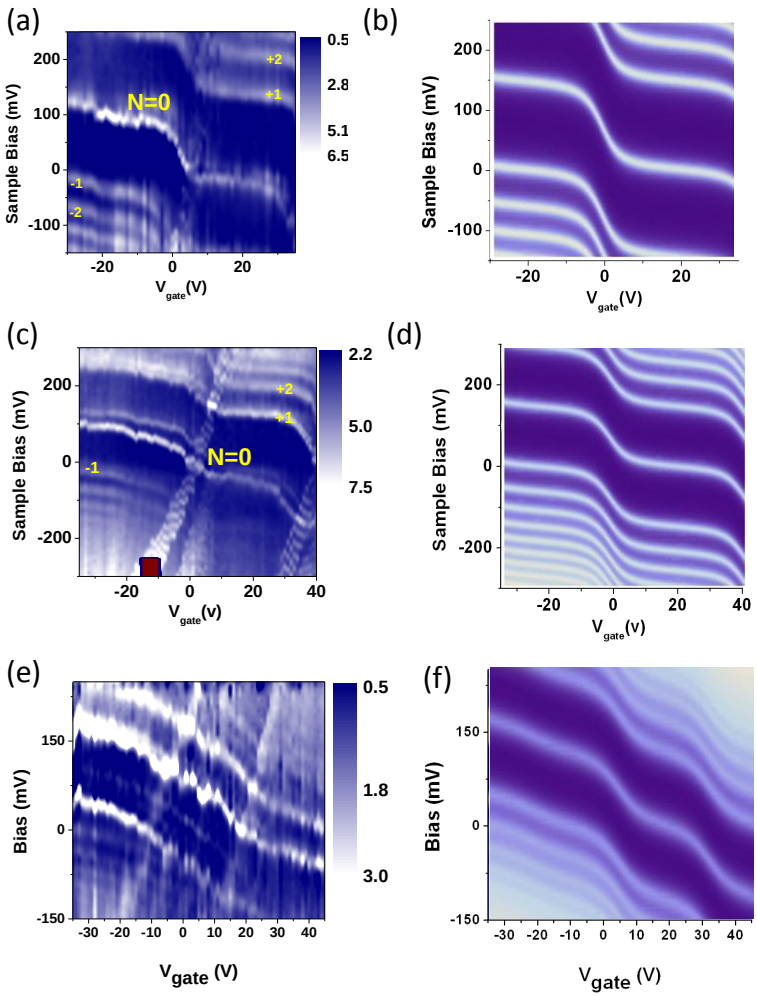

Figure 5.6: (a),(c),(e) STS maps as a function of gate voltage for magnetic fields $B = 12T$,$B = 12T$ and $B = 7T$ respectively. (b),(d),(f) Simulations for (a),(c) and (e) respectively.

chapter, although in this scenario the degree of splitting is expected to depend of the filling of the LLs because of screening. Another possibility could be related to correlations induced gap, however in this case one would also expect that these features would appear at particular fillings rather than for the entire range of carrier density that is investigated. The simulation in Figure 5.6(d) agrees well with the general staircase pattern, but cannot reproduce the discussed gap in the $N = 0$ LL and presence of the 4-peaks.

Figure 5.6(e) shows the spectra taken at a lower field, $B = 7T$ where the

degeneracy of the LL is smaller and as also presented in the simulations the jumps are less abrupt. The simulation for this case in Figure 5.6(f) is in good agreement with the data.

Chapter 6

Effects of charged impurities and other disorder of the electronic spectrum in the quantum Hall regime

Disorder plays a fundamental role in two-dimensional (2D) electron-systems, dramatically affecting their physical properties. Understanding the effects of disorder at the atomic scale is crucial for understanding 2D electron systems. The dominant source of scattering and disorder in 2D electron systems [3] are charged impurities. They can produce a spatially localized signature in the density of states (DOS) which, for impurities located at the sample surface, is readily observed with scanning tunneling microscopy and spectroscopy (STS/STM) [133].

In this respect graphene is ideally suited system for elucidating the effect of impurities[134, 135, 136, 50, 137, 138, 139, 140, 141]. [10, 142, 143], being a two dimensional (2D) material with its electronic states at the surface.

Previous experiments that report the spectrum of a 2D electron system with spatial resolution in the QH regime [92, 144, 145, 96, 146, 147] appeared to support a picture of bent Landau levels (LLs), whose energies continuously change in space, adjusting to the local disorder potential $U(\mathbf{r})$. This behavior can be fully understood within the semi-classical framework, where electrons follow classical drift trajectories along the equipotential lines of $U(\mathbf{r})$. In this picture, LLs are broadened into bands with a continuous spectrum within. It is physically clear, however, that since the drift orbits around impurities are closed and finite in size, the true quantum-mechanical spectrum within each LL is, in fact, discrete as

illustrated in Figure 6.1(a).

In this chapter we discuss spatially resolved scanning tunneling spectroscopy and microscopy experiments that reveal the influence of an isolated impurity on the electronic spectrum of graphene in the QH regime and demonstrate that its strength can be controlled by gate voltage. We find that the impurity-potential is strongest above half filling (weak screening) causing the Landau-levels to split into discrete localized sublevels that are purely orbital in nature. By tuning the gate voltage below half-filling, the impurity becomes almost invisible. These results shed new light on the electronic properties in the QH regime and on the prospect of realizing tunable nanoscale quantum-dots in graphene. Furthermore progress in elucidating other disorder effects that are extrinsic to graphene are presented.

Parts of this chapter follow closely the text in [33, 148].

6.1 The LL spectrum of graphene in the presence of a charged impurity

6.1.1 Lifting of the orbital degeneracy and screening of an impurity

The low energy spectrum of pristine graphene consists of two electron-hole symmetric Dirac cones. This gives rise to a linear density of states, which vanishes at the charge neutrality point (CNP), also known as the Dirac point. In the presence of a magnetic field B, the spectrum becomes quantized in a sequence of LLs with energies:

$$E_N = \pm\frac{\hbar v_F}{l_B}\sqrt{2|N|} = \pm v_F\sqrt{2e\hbar|N|B}, N = 0, \pm1, \pm2, \ldots, \tag{6.1}$$

where v_F is the Fermi velocity, $l_B = \sqrt{\hbar/eB}$ the magnetic length, e the electron charge, $\hbar$ the reduced Planck constant, and $+(-)$ refers to electron (hole) states

$N > 0 (N < 0)$.

Seeking to investigate the effect of an impurity potential on the LL spectrum, we used STM/STS to locate an impurity and characterize its properties. We used samples of exfoliated graphene deposited on a highly doped Si back-gate capped by $300nm$ of chlorinated SiO_2. In order to achieve high quality samples, for this experiment we used two graphene layers twisted by a large angle [46, 149]. The fact that the rotation angle is large ensures that the spectrum of single layer graphene is preserved, however the level degeneracy is doubled [149, 130, 131]. The STM topography image of such an impurity is shown in Figure 6.1(b).

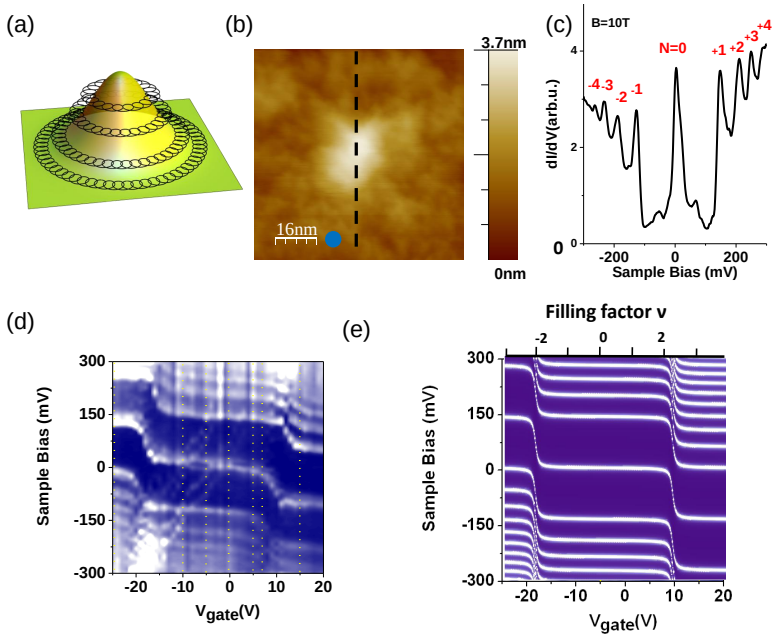

Figure 6.1: (a) Schematic illustration of drift orbits around a charged impurity. (b) STM topography image showing an isolated impurity in graphene (bias voltage $V = 250mV$ and tunneling current $I_t = 20pA$). The spectrum in (c) and map in (d) were taken at the position indicated by the blue dot and the tunneling spectra in Figure 2(b) were taken along the dashed line. (c) STS in $B = 10T$ shows quantized LLs corresponding to $N = 0, \pm1, \pm2, \pm3, \pm4$ (d) Intensity map of tunneling spectra as a function of gate voltage. (e) Schematic DOS and corresponding LL sequence in graphene. The gray area below the Fermi level, chosen to coincide with the Dirac point represents filled states, and above it are empty states.

The differential tunneling conductance dI/dV measured in STM/STS is proportional to the local single-particle DOS, $D(E, \mathbf{r})$, at the tip position $\mathbf{r}$ with the bias voltage $V = (E - E_F)/e$ corresponding to an energy E relative to the Fermi level E_F. A typical dI/dV spectrum taken far from the impurity in the presence of a magnetic field is shown in Figure 6.1(c). The peaks in the spectrum correspond to the LLs [69, 90] and the level index is readily obtained by fitting to Equation 6.1. The LLs are well resolved up to $N = 4$ in both electron and hole sectors attesting to good sample quality. Fitting the field and level index dependence to Equation 6.1 we confirm that the spectrum corresponds to single layer graphene with $v_F = 1.2 \times 10^6 ms$, a value consistent with other measurements on similar samples. In pristine graphene the CNP coincides with the Fermi energy, but this is not the case in most samples due to the inevitable presence of charged impurities. For the sample in Figure 6.1 the CNP is very close to the Fermi energy ($18meV$) attesting to a low intrinsic doping level ($n \approx 3 \times 10^{10} cm^{-2}$), which again is consistent with good sample quality [143].

By tuning the back-gate voltage we change the carrier concentration in graphene to explore its influence on the electronic spectrum. Keeping the tip position fixed we obtain the spectrum for each carrier concentration, shown in Figure 6.1(d). The vertical and horizontal axis represent the sample bias (or energy) and the back-gate voltage respectively, with the bias origin chosen to coincide with the Fermi energy. For the sample geometry used here the carrier density is given by $n \approx 7 \times 10^{10} V_g[V] cm^{-2}$, where V_g is the back-gate voltage. Bright lines correspond to the LLs and the step-like pattern reflects their discreteness and degeneracy [6, 46]. Since the energy of the LLs is independent of the Fermi energy the bright lines are nearly horizontal for gate voltages corresponding to partially filled levels. Once a LL is filled, a further increase in gate voltage starts populating the next LL and the simultaneous jump in Fermi energy produces a shift in the spectrum

which gives rise to the steps in Figure 6.1(d). The simulated map in Figure6.1(e) is in good agreement with the experimental map.

We now focus on the influence of the impurity on the spectrum. To this end, we first present dI/dV maps at fixed energies over the area in Figure 6.1(b). In Figure 6.2(a) we show a typical spectrum around $N = 0$ LL together with energies at which the dI/dV maps in Figure 6.2(b) were taken. The maps are roughly radially symmetric, consistent with a charged impurity at the center. In addition, the stronger intensity (bright spots) at negative energies corresponds to a down-shift of the LL energies, as explicitly seen in Figure 6.2(c). This downshift is indicative of a positively charged impurity, which thus breaks the electron-hole symmetry of the LL spectrum.

We study this effect quantitatively by measuring spectra along the line cut shown in Figure 6.1(b). The resulting map shown in Figure 6.2(c) was taken at $V_g = 7V$ where the effect is strongest as discussed later. The horizontal axis refers to the spatial position along the cut. We note that upon approaching the impurity the energy of the LLs shifts downwards (toward negative energies) reaching its minimum value right at the impurity, consistent with the maps in Figure 6.2(b). Remarkably, in the immediate vicinity of the impurity the $N = 0$ LL does not shift smoothly, but rather splits into a series of well resolved discrete spectral lines. This is clearly demonstrated in Figure 6.2(d) where we plot the spectra at the positions indicated by the yellow dashed lines A, B, and C.

The origin of these discrete states can be understood by considering the quantum-mechanical electron motion in graphene in the presence of a magnetic field and a single charged impurity. For simplicity, we assume a weak, radially and valley symmetric potential $U(r)$ of an impurity located at point $r = 0$, $r = |\mathbf{r}|$.

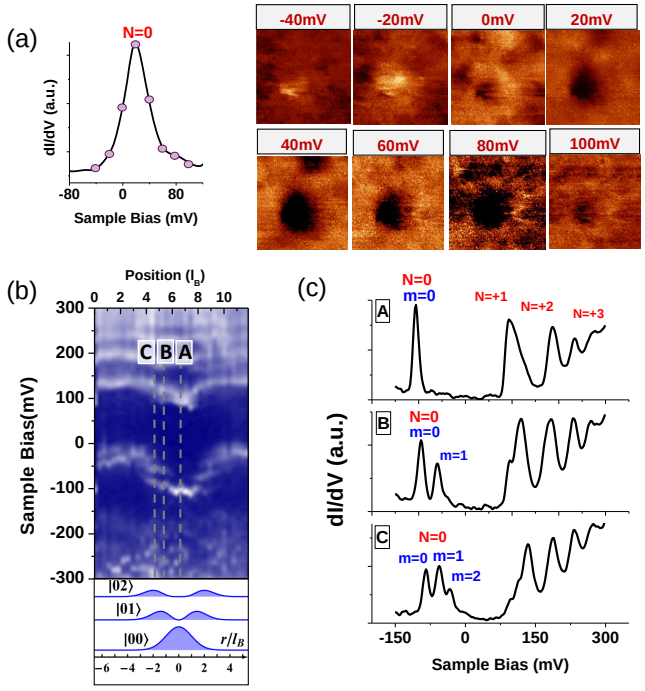

Figure 6.2: (a) dI/dV spectrum far from the impurity together with the energies at which the maps in (b) were taken. (b) Spatial dI/dV maps near the impurity for $V_g = 0V$ and $B = 10T$. The scale bar for all maps is the magnetic length $l_B = 8.2nm$. (c) STS for $V_g = 7V$ and $B = 10T$ taken along the vertical line shown in Figure 6.1(b) with the origin at the top. The blue lines in the bottom part show the probability densities $\psi^\dagger_{0m}(\mathbf{r})\psi_{0m}(\mathbf{r})$ of the states $|0m\rangle$ with angular momenta $m = 0, 1, 2$ which agree with spatial distribution of the resolved discrete spectral lines. (d) dI/dV spectra representing cuts in the map in (c) at positions indicated by the dashed lines A, B, and C.

We also neglect the Zeeman effect.

Under these assumptions, in each valley, K or K', and for each spin projection, $\uparrow$ or $\downarrow$, the electron wave-function $\psi(\mathbf{r})$ satisfies an effective Dirac equation:

$$\hat{H}\psi = E\psi, \hat{H} = \hat{H}_0 + U(r), \hat{H}_0 = \hbar v_F \sigma(\mathbf{p} - e\mathbf{A}). \tag{6.2}$$

Here σ represents Pauli matrices and $\mathbf{A}$ is the vector potential. The wave-function $\psi(\mathbf{r}) = (\psi_A(\mathbf{r}), \psi_B(\mathbf{r}))^t$ is a two-component spinor in the AB sublattice space. $\hat{H}_0$ describes electron motion in the magnetic field $\mathbf{B} = (0, 0, B)$ in the absence of the impurity. The solutions to the eigenvalue problem $\hat{H}_0\psi_{Nm}(\mathbf{r}) = E_N\psi_{Nm}(\mathbf{r})$ yield

the unperturbed LL sequence in Equation 6.1 and the wave functions $\psi_{Nm}(\mathbf{r})$ of the eigenstates $|Nm\rangle$. In the symmetric gauge $\mathbf{A} = \frac{1}{2}[\mathbf{B} \times \mathbf{r}]$, $|Nm\rangle$ are labeled by the LL index N and an integer orbital momentum $m \geq -|N|$ (Figure 6.3(a)). Importantly, since the energies E_N are independent of m, the LLs have an infinite orbital degeneracy (for an infinite sample).

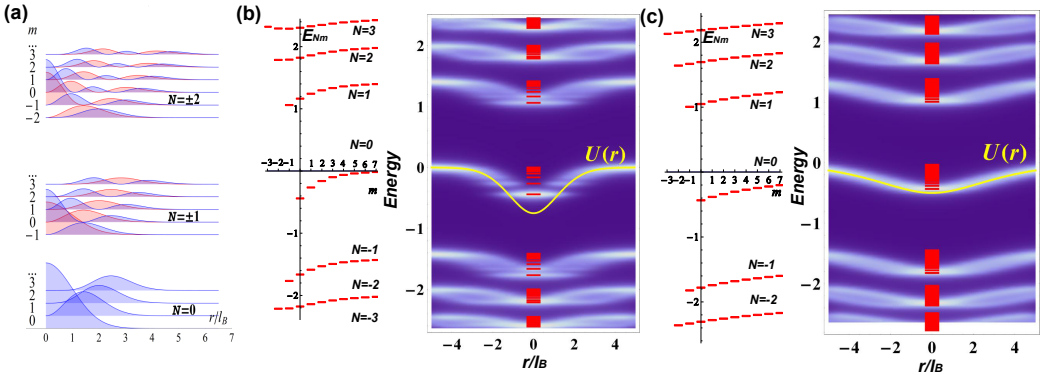

Figure 6.3: (a) Probability densities $|\psi_{NmA}(r,\varphi)|^2$ and $|\psi_{NmB}(r,\varphi)|^2$ on A (blue) and B (red) sublattices, respectively, of the wave-functions in graphene in a magnetic field in the absence of an impurity. The plots are for one valley, for the other valley the sublattices would be interchanged, $A \leftrightarrow B$. (b) and (c) Simulated spectra E_{Nm}(left) and tunneling DOS $D(E,\mathbf{r})$ (right) in graphene in the QH regime in the presence of an impurity, calculated according to Equation (3) for a model potential $U(r) = U_0 \exp(-r^2/b^2)/\sqrt{r^2+a^2}$ (yellow line) with linewidth $\gamma = 0.05\hbar v_F/l_B$. (b) The case of a sufficiently sharp impurity potential with $a = 2l_B$, $b = 2l_B$, $U_0 = 1.5\hbar v_F/l_B$, for which $\gamma < \Delta E_{Nm}$ and the discreteness of the spectrum around an impurity is resolved for lower LLs, $N = 0, \pm 1$. (c) The case of a smooth impurity potential with $a = 3l_B$, $b = 6l_B$, $U_0 = 1.5\hbar v_F/l_B$, for which $\gamma > \Delta E_{Nm}$ and the discreteness cannot be resolved.

For a sufficiently weak impurity potential, when first-order perturbation theory holds, the LL spectrum acquires an m-dependent correction $U_{Nm} = \langle Nm|U(r)|Nm\rangle$ resulting in the spectrum $E_{Nm} \approx E_N + U_{Nm}$. The impurity may be treated as a perturbation provided $U_{Nm} \ll E_N$. Thus, the impurity lifts the orbital degeneracy of the LLs and splits them into series of discrete sublevels. For a given LL index N, the level spacing $\Delta E_{Nm} = E_{N,m+1} - E_{Nm}$ is largest for $\psi_{Nm}(\mathbf{r})$ localized in the immediate vicinity of the impurity, i.e., for lower m. For larger m, the wave

functions spread out away from the impurity and the energy levels get denser, approaching the values of the unperturbed LLs: $U_{Nm} \to 0$ and $E_{Nm} \to E_N$ as $m \to +\infty$. The level spacing grows with the overall magnitude of the potential $U(r)$ and decreases with increasing its spatial extent; similarly it decreases with increasing N, as the spatial extent of the wave-function $\psi_{Nm}(\mathbf{r})$ grows. These general properties are illustrated in Figure 6.3.

In the ideal single-particle case, each discrete level E_{Nm} contributes an infinitely narrow delta-function peak $\delta(E - E_{Nm})$ to the DOS. The energy levels measured by STS/STM via the dI/dV spectrum, however, always possess some finite linewidth γ. The linewidth may represent the natural finite lifetime of an electron state due to inelastic processes or could be limited by instrumental resolution. This level broadening can be taken into account phenomenologically by modeling the tunneling DOS by the expression

$$D(E, \mathbf{r}) = 4 \sum_{Nm} \delta_\gamma(E - E_{Nm}) \psi^\dagger_{Nm}(\mathbf{r}) \psi_{Nm}(\mathbf{r}), \tag{6.3}$$

where $\delta_\gamma(E) = \gamma/[\pi(E^2+\gamma^2)]$ are Lorentzians of width γ (the factor 4 comes from the valley and spin degeneracy in single layer graphene). The ideal single-particle DOS is obtained in the limit $\gamma \to 0$, when the Lorentizian becomes a delta function, $\delta_\gamma(E) \to \delta(E)$.

The intensity of the broadened peaks $\delta_\gamma(E - E_{Nm})$ is position-dependent and determined by the probability density $\psi^\dagger_{Nm}(\mathbf{r})\psi_{Nm}(\mathbf{r})$ in a given state $|Nm\rangle$. The discreteness of the spectrum E_{Nm} around a given m can be resolved in the experimental $D(E, \mathbf{r})$ if the linewidth γ is smaller than the level spacing ΔE_{Nm}. If however $\gamma > \Delta E_{Nm}$, then for a given LL N, the broadened peaks $\delta_\gamma(E - E_{Nm})\psi^\dagger_{Nm}(\mathbf{r})\psi_{Nm}(\mathbf{r})$ of adjacent (in space and energy) states overlap in the sum over m and merge into a broadened continuous line. Thus, even if the spectrum is discrete, but the resolution is insufficient, the measured $D(E, \mathbf{r})$ will

still display "bent" LLs, whose energies seemingly adjust to the local value of the impurity potential $U(r)$, as illustrated in Figure 6.3(c).

Our data in Figure 6.2 are fully consistent with the above theoretical considerations. As clearly seen in Figures 6.2(c),(d) upon approaching the impurity the $N = 0$ LL splits into three well resolved discrete spectral lines, which we are able to attribute to specific impurity states. To lowest order in perturbation theory, one may use the wave-functions $\psi_{Nm}(\mathbf{r})$ unperturbed by the impurity, which are known, see Figure 6.3(a), and solely determined by one parameter, the magnetic length l_B. Using Equation 6.3, we find that the spatial distribution of the three discrete lines is in good agreement with the probability densities $\psi^{\dagger}_{0m}(\mathbf{r})\psi_{0m}(\mathbf{r})$ of the states $|0m\rangle$ with $m = 0, 1, 2$, as shown in Figure 6.2(c). The states $|0m\rangle$ with $m \geq 3$, however, are less affected by the impurity potential and their contributions to $D(E, \mathbf{r})$ merge into a single continuous line. The discreteness of the spectrum is also not resolved for higher index LLs, $N \neq 0$, consistent with the weaker impurity effect predicted by the theory. Finally, we mention that the theoretically simulated DOS for a model potential shown in Figure 6.3(b), very closely resembles the experimental map in Figure 6.2(c).

We now turn to the effect of the electron density on the strength of the impurity potential. The evolution of the LL spectrum close to the impurity shows a surprisingly strong dependence on gate voltage as illustrated in Figure 6.4(a). In the range of gate voltages corresponding to filling of the $N = 0$ LL, $-15V < V_g < 9V$, the impurity strength monotonically grows with increasing V_g (i.e., the filling fraction and E_F): the distortion of the $N = 0$ LL is weak, moderate, and strong for $V_g = -10V, 5V$, $V_g = 0V$, and $V_g = 7V$, respectively. We note that the impurity can shift the energy levels by as much as 0.1 eV, indicating that the effect would survive at room temperature. Also, for $V_g = -25V$, corresponding to a more than

half-filled $N = -1$ LL, the effect is strong, while for $V_g = 15V$, corresponding to less than half-filled $N = 1$ LL, it is nearly absent. This suggests that the same monotonic growth of the impurity effect with gate voltage would be present for filling other LLs, as well.

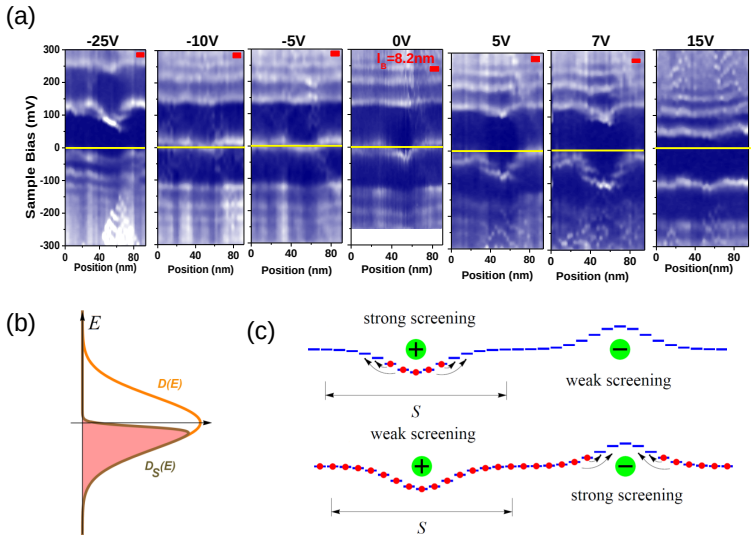

Figure 6.4: (a) Maps of the tunneling spectra versus position across the impurity for indicated gate voltages. The Fermi level is highlighted by the yellow line. (b) and (c) Schematic picture of the local screening properties, responsible for the variation of the impurity strength as function of doping. (b) The particle-hole asymmetry of the local screening properties is reflected in the local DOS $D_S(E)$ averaged over a finite-size region of area S around a positively charged impurity. (c) Top: Below half-filling of a given LL, virtual electron transitions (indicated by arrows) between the filled and empty states (red dots represent electrons) occur in the vicinity of positively charged impurities and away from negatively changed impurities; hence, their potentials are strongly and weakly screened, respectively. Bottom: above half-filling, the situation is particle-hole reversed.

We attribute the observed variation in the strength of the impurity potential with gate voltage to the screening properties of the electron system. Our argument is illustrated schematically in Figures 6.4(b) and 6.4(c). For a positively charged impurity and less than half filled LLs, empty states necessary for virtual electron transitions to occur, are available in the vicinity of the impurity, which leads to substantial screening. For more than half-filled LLs, empty states are

available only far away from the impurity, which renders local screening inefficient. For a negatively charged impurity, the situation would be particle-hole reversed within a given LL: its potential would be screened (unscreened) roughly above (below) half-filling. These properties are readily derived by examining the local DOS, $D_S(E) = \int d^2\mathbf{r}\, D(E, \mathbf{r})/S$, averaged over the finite-size region of area S around the impurity. Unlike the DOS averaged over the whole sample, such local DOS is manifestly particle-hole asymmetric within a given Landau level, which translates to the particle-hole asymmetry of the local screening.

For gate voltages $V_g = -5V, 0V$ in Figure 6.4(a), where the impurity potential is screened, the level splitting is not visible and the $N = 0$ LL appears as a continuous distorted line, similar to earlier observations [92, 145, 146]. This reflects the fact that at these gate voltages the splitting between the impurity sublevels is reduced below the linewidth, giving an appearance of a "bent" LL, as illustrated in Figure 6.3(c). The capability to tune the strength of the impurity potential by the gate voltage thus allows us to trace the evolution between the discrete and the quasi-continuous regimes of the impurity spectrum.

An isolated impurity in the QH regime thus behaves as a multi-level tunable quantum dot. Graphene-based quantum dots are highly desirable as building blocks for single electron transistors, detectors, memory and spin qubit devices [150, 151], owing to unique properties such as two-dimensional structure, mechanical robustness, and long spin coherence times. Realizations of such devices, tens of nanometer in size[152, 153, 154, 155], achieved by lithographic techniques are inherently limited by the difficulty to control the edge structure and size. The findings reported here demonstrate a mechanism for realizing tunable nanoscale quantum dots in graphene, which circumvents the need for nanosculpting. Furthermore, realization of gate controlled energy level shifts of $0.1eV$ opens

the door to room-temperature graphene-based nanoelectronics.

6.1.2 Strategy for finding isolated impurities

We find that the most efficient way to identify isolated impurities is by using Landau level spectroscopy. The reason is that the position of the LLs for certain range of filling is very sensitive to the local potential (as discussed in the previous section), much more so than the typically very broad V-shaped spectrum taken in the absence of magnetic field.

Figure 6.5(a) shows an STM image over a large area on the sample studied. The first step towards finding impurities is to take the tunneling spectra along a line such as the one indicated. We then plot the tunneling spectra as a function of position along the line and the resulting map is shown in Figure 6.5(b). We can clearly see that the energies of the LLs, strongest for N=0 (for reasons explained in the main text), shift with position reflecting the presence of a potential created by charged impurities. N=0 moves towards both negative and positive energies suggesting the presence of both positive and negative impurities. We then look for an area that shows a minimal number of impurities such as the one indicated by the red arrow in Figure 6.5(a), where the data in the main text were taken.

6.1.3 Typical effects of close-together impurities in a single layer graphene on SiO_2

To illustrate an example of studying impurities on single layer graphene on SiO_2, Figure 6.6(a) shows the topography of an area affected by multiple impurities. The typical spectrum averaged over the entire area is shown in Figure 6.6(b) at magnetic field B=12T. In this case we can resolve N=0, N=+1, etc.

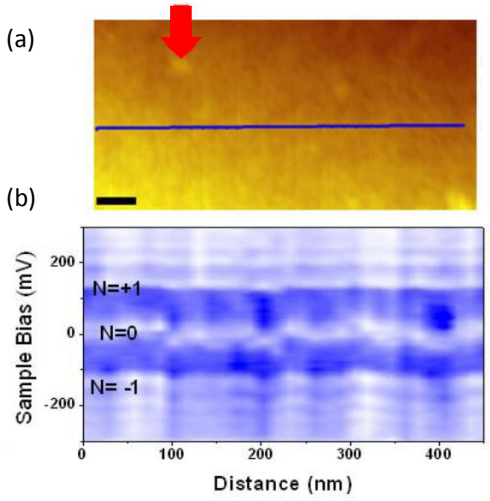

Figure 6.5: (a) STM topography of the graphene sample. Scale bar: 50nm. (b) dI/dV line map along the blue line in (a).

Figure 6.6 shows the dI/dV maps across the region in Figure 6.6(a), at bias voltage indicated in Figure 6.6(b) by E (0V) and L(55V). The light color represents large DOS, while the dark color is low DOS. Therefore, we can identify several impurities located in the area. To see the effect of these impurities we take a line cut across the direction indicated in Figure 6.6(a) and the result is presented in Figure 6.6(d). In this case we see two features: one is the fact that the LLs "bend" around the impurities, but it is hard to distinguish the effect of a single impurity. The second feature is the split of the N=0 is several bands, which are a result of the presence of the 4-peaks mentioned above.

More examples of the effect of charged impurities on the LL spectrum is shown in Figure 6.7. Figure 6.7 (a) is a topographic image on the area of the twisted bilayer sample where we identify 3 charged impurities. Notice that in this case they have no distinct signature in the topographic image. The typical dI/dV spectrum away from impurity is shown in Figure 6.7(b) and blue circles show the energies at which the maps in Figure 6.7(c) are taken. The dI/dV spatial maps in Figure 6.7(c) clearly show the presence of three independent impurities and

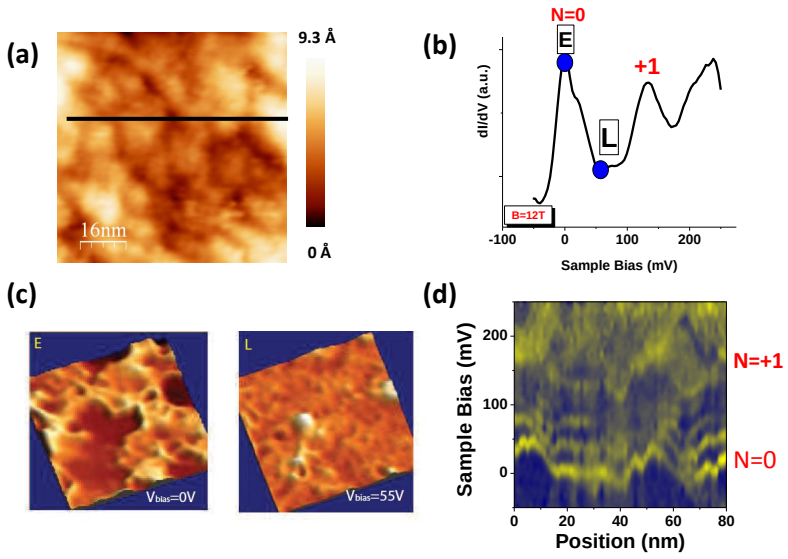

Figure 6.6: (a) Topography of graphene on SiO_2. (b) STS spectrum at $B = 12$T averaged over the area in (a). (c) dI/dV maps at energies indicated by E and L in (b). (d) Dependence of the STS on position along the line in (a).

the high intensity at $-30meV$ indicated that in this case too we have positive impurities shifting the LL towards negative values.

The tunneling spectra around these impurities, distinguished as $1, 2, 3$ in Figure 6.8(a) are shown in Figure 6.8(b),(c) and (d). Similar to the data presented in the previous chapter, the LL sequence in the graphene region is that of a single layer and the LL appear "bent" around the impurity. In the case of impurity 1 there is even a hint of splitting of the N=0 around the impurity suggesting that this particular impurity was strong enough to provide a large potential that would lift the orbital degeneracy if the LL around it.

6.2 Towards elucidating the origin of extrinsic peaks in the LL spectrum

In order to understand more the origin and behavior of the 4-peaks measured in the STS spectra we have studied samples that have graphene on BN which allow

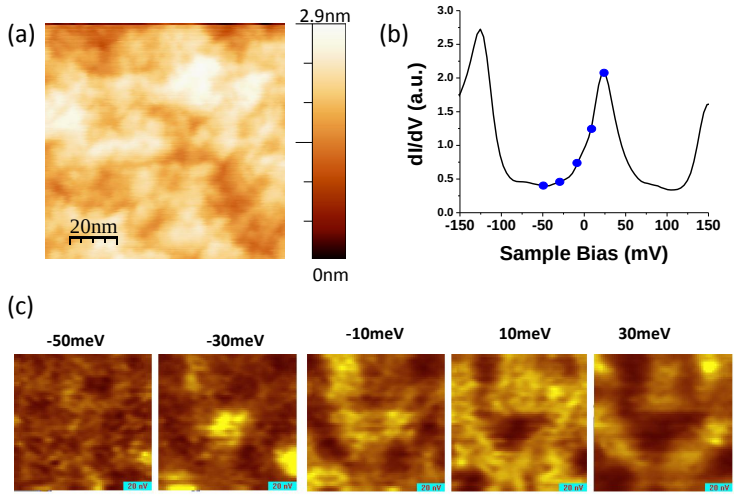

Figure 6.7: (a) Topography image of an area on the large angle twisted graphene sample which shows three close together impurities. (b) STS spectrum taken in an impurity-free region of the area in (a). The blue dots indicate the energies where the maps in (c) are taken. (a) dI/dV maps at particular energies across the area in (a) showing the presence of 3 impurities.

observation of Landau levels in high enough fields.

One question that we address is *what is the magnetic field dependence* of the 4-peaks? To this end we position the STM tip at one point and record the spectrum as a function of magnetic field. The data is summarized in Figure 6.9(a). Above $B = 4T$ the presence of pairs of 4 distinct, equidistant peaks on the negative side of the spectrum is clear. We observe more than one band of 4-peaks. Measuring the distance between the peaks for 2 different areas and plotting it as a function of the magnetic field we obtain the results in Figure 6.9(b). We notice a weak field dependence and a typical separation between peaks of $\Delta E = 20 - 30meV$.

In an area where a charge impurity is present we can also study the *behavior of the 4-peaks around a charges impurity* as presented in Figure 6.9(c). The right panel is the topographic image of an area of graphene on BN and the arrow indicates where the STS data was taken. The left panel is the map of the dI/dV spectrum as a function of position across the line in the right panel. the $N = 0$

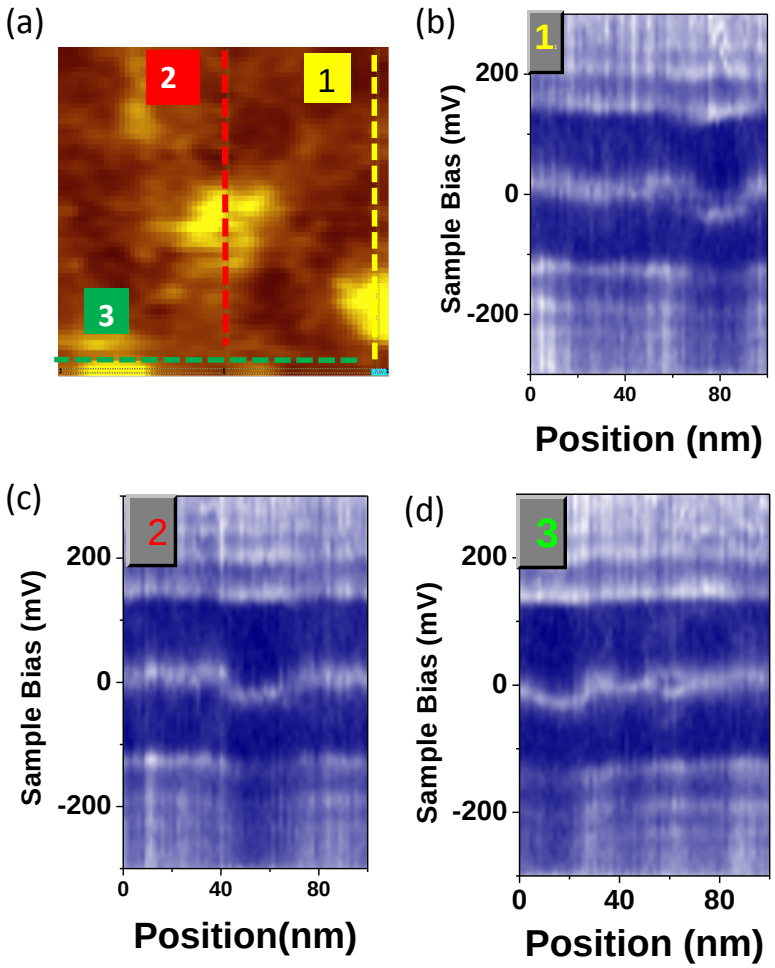

Figure 6.8: (a) dI/dV map also shown in Figure 6.7 highlighting the presence of 3 impurities at the positions of the bright yellow features. The dashed lines indicate the positions across which the data om (b),(c),(d) was taken. (b)-(d) Position dependence across the lines in (a) of the STS spectra across the 3 impurities.

LL is present at approximately the Fermi level and to the left and right end of the energy range, around $400mV$ and $-400mV$ we see a clear series of 4peaks. Interestingly they are present in the entire region and around the positions with a charge impurity they bend upwards towards more positive energies.

To gain insight into the spatial extent of the states that are responsible for the appearance for the 4-peaks, the spatial dI/dV maps were studied in the region shown in Figure 6.10(a). In Figure6.10(b), the STS spectrum was taken in the top left part of Figure 6.10(a) and was restricted to the negative energy interval

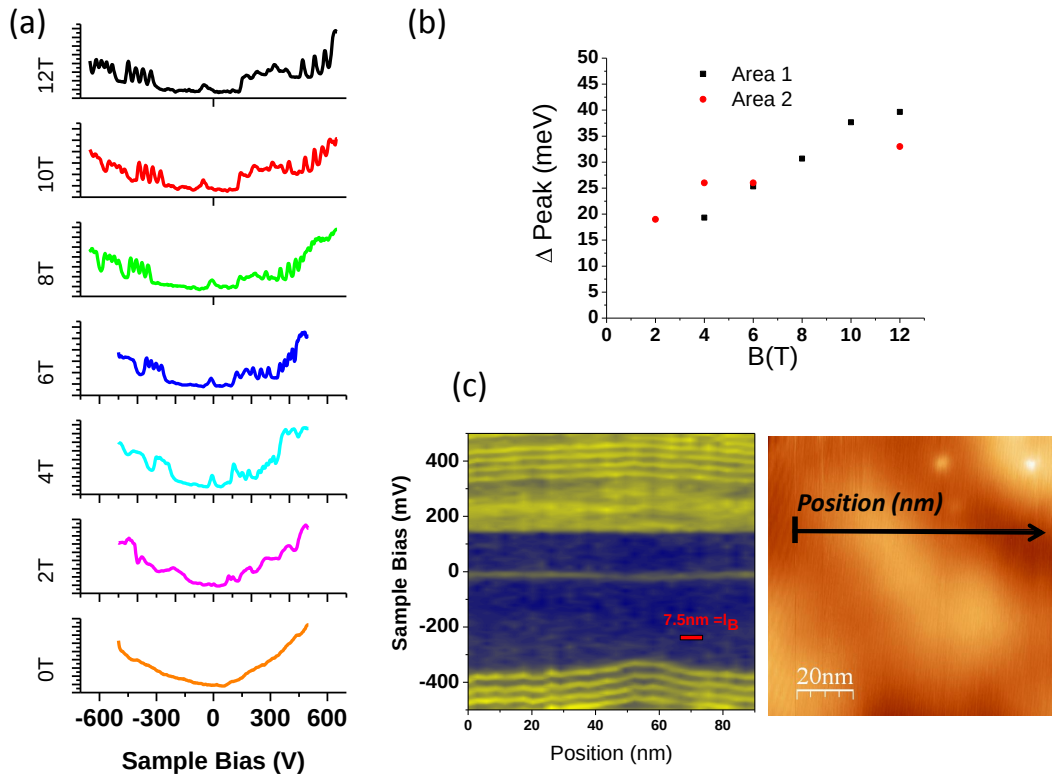

Figure 6.9: (a) Magnetic field dependence of the spectra taken at one position where the 4-peaks are pronounced. (b) The energy separation between the peaks for the area in (a) (Area 1) and a second Area 2. (c) Position dependence of the STS spectrum at 12T. The right panel shows the topography image with the black arrow indicating the region where the spectra were recorded. The left panel is the position dependence of the STS spectra.

where the 4-peaks were present.

The white dots with red contour mark the energies at which the sequence of dI/dV maps in Figure 6.10(c) were recorded (the peaks and the valley of the spectrum). Starting from $-530meV$ we observe that at energies corresponding to a valley the spatial dI/dV maps shows hollow ring, while at the peaks, the maps have opposite contrast. This repetitive pattern suggests that each of the 4 peaks has the same origin.

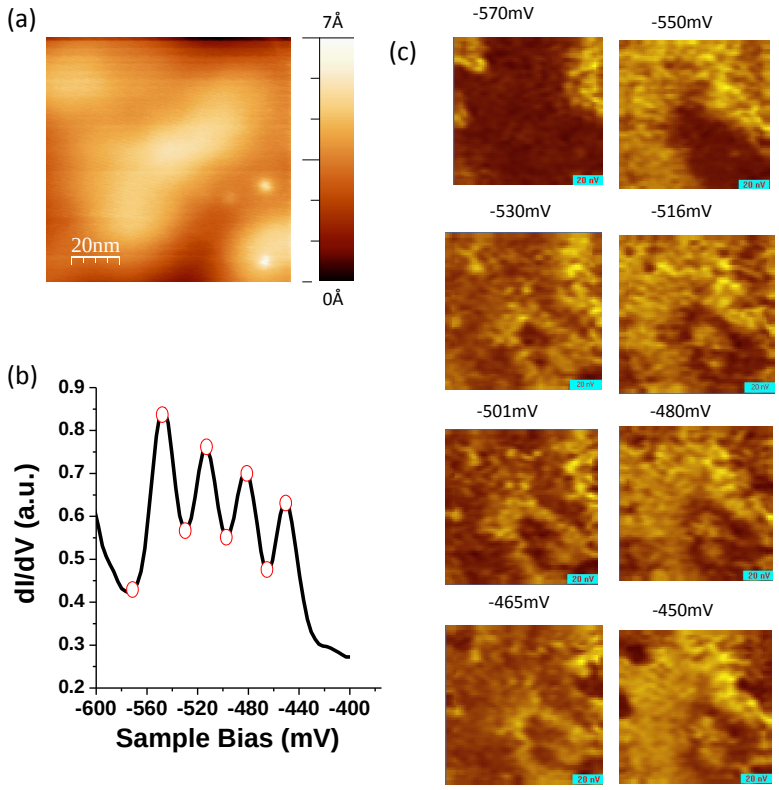

Figure 6.10: (a) Topography image where the maps in (c) were taken. (b) STS spectrum taken in the upper left corner of (a) and indicating the energies at which the maps in (c) are taken. (c) STS maps across the area in (a) at energies marked in (b).

6.3 Strain and electronic properties

Controlling strain in graphene is expected to provide new ways to tailor its electronic properties [156, 157]. Interestingly, as a result of strain in the lattice, the electrons in graphene can behave as if an external magnetic field is applied. The origin of this pseudo magnetic field is the fact that strain will introduce a gauge field in the Hamiltonian which mimics the presence of a magnetic field. In order to create a uniform field, however, the strain needs to be designed in particular configurations such as stretching graphene along three coplanar symmetric crystallographic directions [157].

Experimentally the effect of strain on the graphene spectrum was addressed by STM/STS measurements of graphene nanobubbles grown on a Platinum (111)

surface [100]. On such samples, these peaks in tunneling spectroscopy reported in [100] were interpreted as Landau levels originating from the pseudo magnetic field.

Chapter 7
Electronic properties of twisted graphene layers

Graphite is a stack of graphene layers arranged so that the A atoms of top layer sit above the B atoms of the bottom layer and the B atoms of the top layer sit on to of the center of a hexagon of the bottom layer. This type of stacking is called AB stacking or Bernal stacking. Because the band structure of graphene stacks is determined by the hoppings between neighboring carbon atoms, the stacking order plays a major role in determining the electronic properties of the these systems [123, 158, 159, 160, 161].

For a bilayer graphene one can have the situation that that A (B) atoms of the top layer sit directly above A (B) atoms of the bottom layer and this is called AA-stacking (Figure 7.1 (a)), however it is typically the case for the bilayers extracted from graphite that the stacking order is Bernal or AB-stacking (Figure 7.1 (b)) [158].

When the two layers have an infinitesimally small rotation away from Bernal stacking the system will significantly change its the electronic properties [149, 162, 163, 164]. For large angles of rotation it will mostly have properties of single layer graphene, while for small angles the properties of the twisted layers become more complex. This property opens up the possibility of an extra knob to tune the electronic properties of graphene stacks.

With the new methods of preparing graphene by chemical vapor deposition it became even more important to address questions regarding properties of rotated layers since the growth mechanism seems to favor the formation of twisted layers

[62, 61, 60].

In this chapter using scanning tunneling microscopy and spectroscopy, direct evidence for the electronic structure of twisted graphene layers is presented. The samples were suspended membranes of CVD grown graphene and graphite crystals which contain areas with various rotation angles. In topographic images the regions of twisted layers appear as superpatterns, Moiré patterns, that have periods which depend on the misorientation angle. It is found that the density of states on twisted layers develops two Van Hove singularities that flank the Dirac point at an energy that is proportional to the twist angle. In the presence of a magnetic field the density of states develops quantized Landau levels (LL) characteristic of massless Dirac fermions. From the energy and field dependence of the LL sequence the Fermi velocity is obtained and it is found to be renormalized by an amount that depends on the angle of rotation. These results are compared with theoretical predictions. Parts of this chapter follow closely the text in [33, 149, 164].

7.1 Moiré pattern

Rotational stacking faults are common and have been observed on graphite surface already in early STM studies [165, 166, 167, 168]. Their electronic properties, however have been investigated both theoretically and experimentally only recently with the discovery of graphene.

In this thesis, for studying the effect of twisting graphene layers two types of samples were used: graphite surfaces with rotational stacking defects from growth and graphene samples prepared by Chemical Vapor Deposition (CVD) (Figure 7.2) which were provided to us by Prof. Andre Geim group at Manchester University and Prof. Jing Kong at MIT.

Continuous films of large-area single to few-layer graphene were grown via

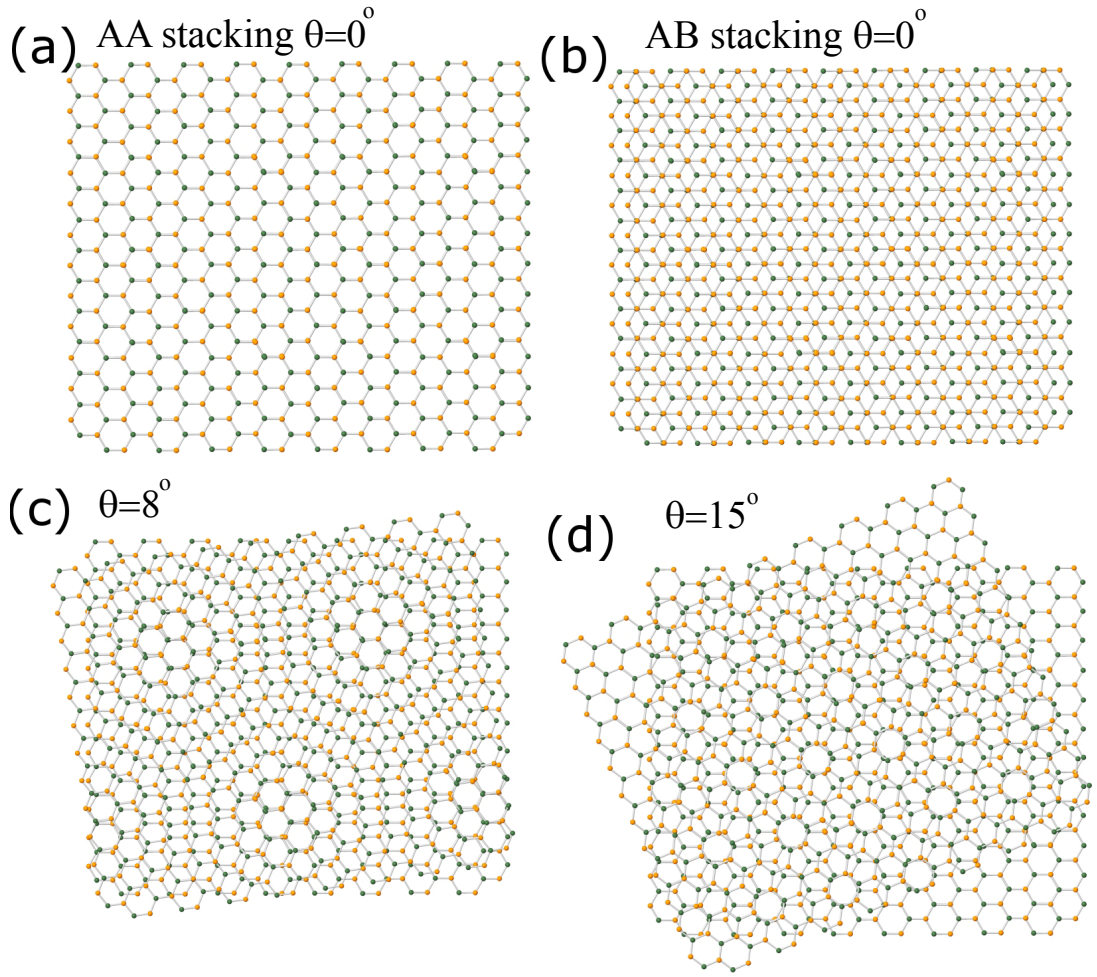

Figure 7.1: (a) Schematic of two layers of graphene superposed in AA stacking. (b) Schematic of two layers of graphene superposed in AB stacking (Bernal stacking). (c) Emergent Moiré patten when rotating two layers of graphene by $\theta = 8^o$. (d) Emergent Moire patten when rotating two layers of graphene by $\theta = 15^o$.

ambient pressure chemical vapor deposition (CVD) on polycrystalline Ni films [62]. These films were transferred from Ni to a commercially available TEM gold grid (Figure 7.2(a)). A 250nm layer of PMMA was spin-coated on graphene to provide mechanical support, after which the graphene layers with PMMA on top were released from the Ni film by etching in 1M $FeCl_3$ solution. After the release, the graphene layer covered with PMMA was transferred to a TEM grid. Acetone was used to dissolve the PMMA and to release the graphene on the gold grid. The samples were dried in a critical point dryer to prevent the membrane from

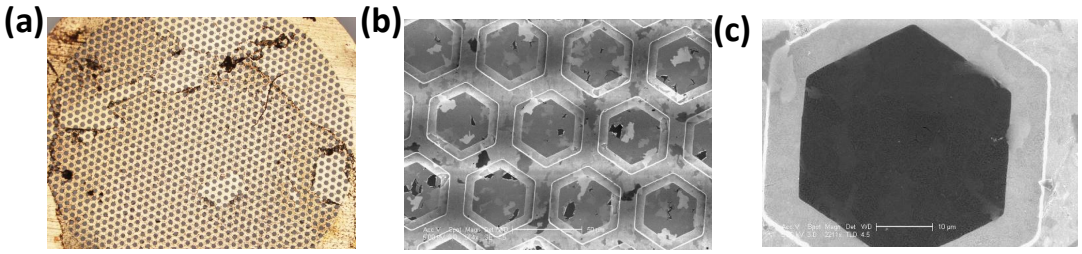

Figure 7.2: (a) Optical image of the graphene film transferred to a Au grid (3mm diameter), (c) and (d) SEM image showing fully covered graphene membrane on gold grid.

rupturing due to surface tension.

The consequence of superposing and rotating two identical periodic lattices with respect to each other is the formation of Moiré patterns. Considering two hexagonal lattices, the Moiré pattern emerging for a rotation angle $\theta = 8^o$ is illustrated in Figure 7.1(c), while for a larger twist angle, $\theta = 15^o$, the pattern becomes finer as illustrated in Figure 7.1(d). A commensurate superstructure is obtained for discrete families of angles that can be mathematically derived [163, 169, 170, 171, 172, 173]. For example, one such family of angles is given by: $cos(\theta_i) = (3i^2 + 3i + 1/2)/(3i^2 + 3i + 1)$ with $i = 0, 1, 2, ...$

The mathematical relation between the period of the superlattice created by twisting the two layers, L and the rotation angle θ is:

$$L(\theta) = \frac{a}{2sin(\frac{\theta}{2})} \tag{7.1}$$

where $a \approx 0.246nm$ is the lattice constant of graphene. From this we can see that for small rotation angles, the Moiré superperiod is very large, while for large angles the superpattern period is smaller.

STM topographic images can reveal areas where a Moiré pattern resulting from the twist of graphene layers is formed. They appear as superpatterns with triangular symmetry and periods larger than the atomic lattice of graphene such as the ones illustrated in Figure 7.3. In Figure 7.3(a) a Moiré pattern is seen in

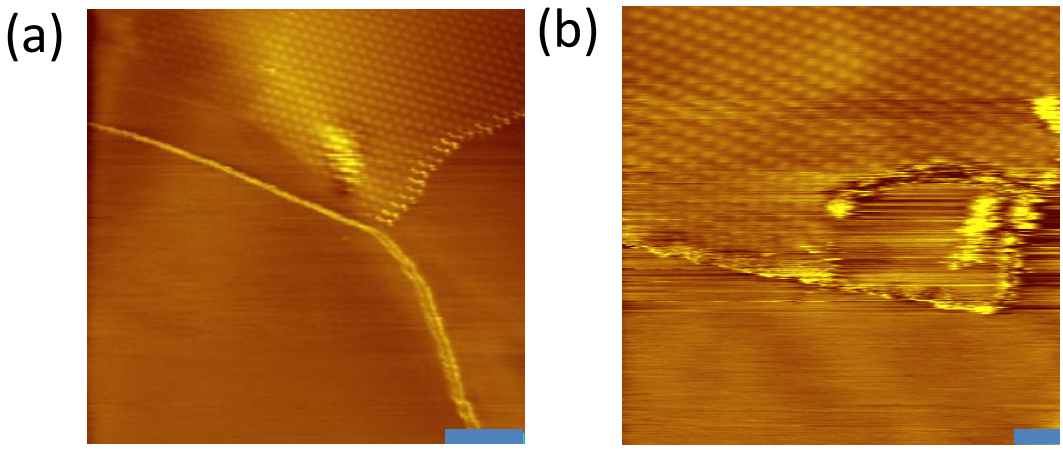

Figure 7.3: (a) STM topography image taken on the surface of graphite (V_b=300mV, I_t=20pA) showing a Moiré pattern on top. scale bar 50nm. (b) STM topography image taken on the surface of graphite (V_b=300mV, I_t=20pA) showing the border of a Moiré pattern. Scale bar 10nm.

the top part of an STM topographic image on graphite surface and in Figure 7.3 (b) a similar situation is presented for the case of a Moiré patterns found on the surface of a graphene film obtained by CVD.

Different angles will result in the formation of different patterns, as described by Eq. (7.1). Experimentally this is demonstrated by STM images showing superpatterns of different periodicity in samples with different twist angles. For example, at rotation angle $\theta = 1.79^o$ the superperiod is $L = 7.7nm$. The sequence of four topographic maps in Figure 7.4 (a)-(d) have approximately the same field of view and they correspond to rotation angles of 1.16^o, 1.79^o, 3.5^o, 21^o. For these angles the corresponding periodicities are:$L(1.16^o) = 12nm$, $L(1.79^o) = 7.7nm$, $L(3.5^o) = 4nm$, $L(21^o) = 0.7nm$. Figure 7.4 (b) (for θ= 1.79^o) illustrates the fact that the period of the atomic lattice of the graphene layer is much smaller than the Moiré pattern and can be visible on top of it. Typically the height observed in topography for the Moiré patterns is $\approx 0.1 - 0.3nm$.

To further demonstrate that the origin of the measured superpattern is the presence of a twist between the top and underlying layer of graphene one can

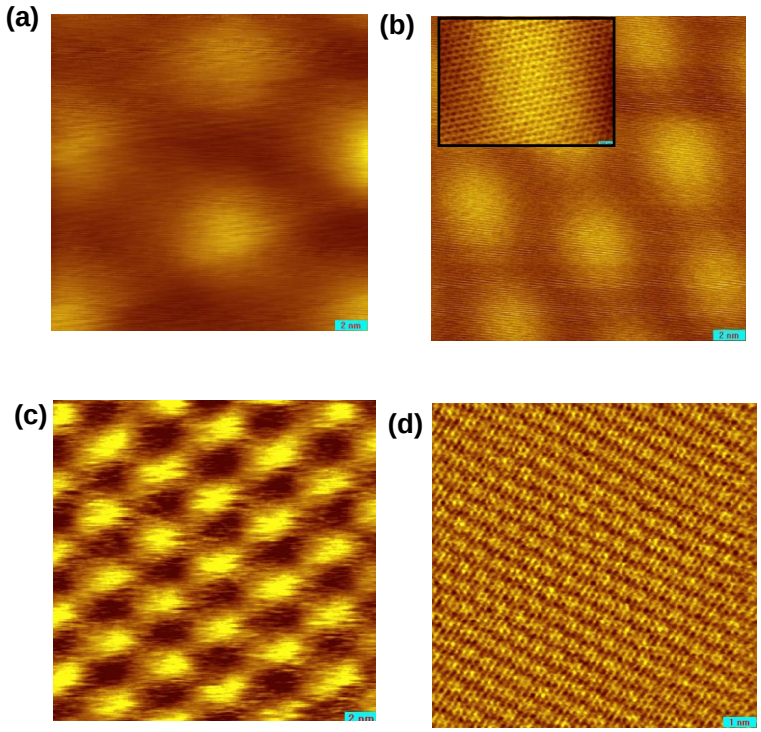

Figure 7.4: (a)(b)(c)(d) STM images for Moiré patterns corresponding to angles 1.16 ^{o},1.79^o, 3.5^o, 21^o, respectively [90, 149]. Scale bar in (a)-(c) 2nm, (d) 1nm. The inset in (b) is an STM imaged zoomed into one of the Moire maxima showing the C atoms lattice. Tunneling parameters:V_b=300mV, I_t=20pA.

compare the Fourier transform of the superpattern and the graphene pattern. In Figure 7.5 such a comparison is presented. Figures 7.5(a) and (b) show the STM images of the superpattern and zoomed in image of the C lattice within the superpattern for rotation angle θ= 1.79^o. If one takes the Fourier Transform (FT) of the Moiré pattern in Figure 7.5(a) one obtains six bright spots at the corners of a hexagon as shown in Figure 7.5(c). Similarly, for the graphene lattice in Figure 7.5(b) one obtains the FT in Figure 7.5(d). The two hexagons have different sizes, the one of the Moiré pattern is much smaller. A schematic superposition of the two is presented in Figure 7.5(e), where the FT of the Moiré pattern was magnified for clarity. The angle between the two is $30^o \pm 2^o$ consistent with the expected $30^o - \theta/2 \approx 29^o$.

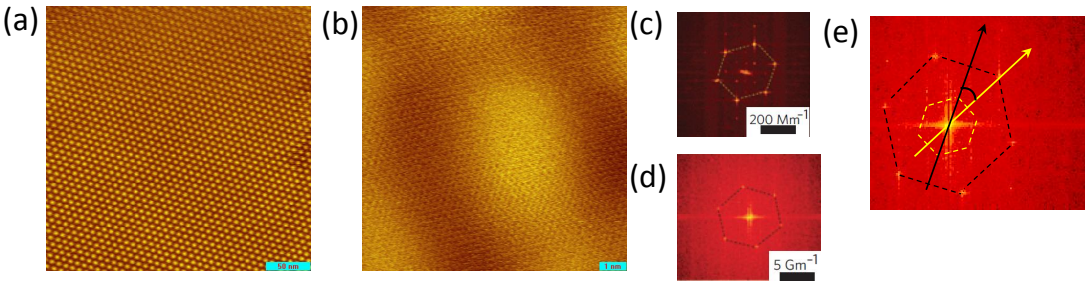

Figure 7.5: (a) STM image of a Moiré pattern corresponding to $\theta = 1.79^o$. (b) Atomic resolution zoom-in of one of the bright spot in the Moiré pattern showing the lattice of the C atoms. (c),(d) Fourier transforms of (a) and (b). (3) Sketch of the superposition of the two FT in (c) and (d) showing the angle between them $29^o \pm 2^o$.

7.2 Van-Hove singularities

In momentum space, the consequence of the twist between two graphene layers is the rotation of the corresponding Dirac cones with respect to each other as sketched in Figure 7.6(b). With the same notation as previously, the distance between the cones is given by:

$$\Delta K = \frac{4\pi}{3a} 2sin(\frac{\theta}{2}) \tag{7.2}$$

At the intersections of the two Dirac cones their bands will hybridize, resulting in the key feature of the band structure, the two saddle points in both the electron and hole side [163, 90]. The theoretical calculation of the dispersion in the case of rotation angle $\theta = 1.79^o$ is presented in Figure 7.6(a).

In general, because the DOS $\propto \frac{1}{|\nabla E(\vec{k})|}$, critical points in the band structure for which $|\nabla E(\vec{k})| = 0$ lead to diverging density of states, also known as Van Hove singularities (VHS)[17]. For twisted graphene bilayers the Van Hove singularities will not appear in the absence of interlayer coupling.

The VHS in the DOS, corresponding to the saddle points in the dispersion shown in Figure 7.6(a), are presented in Figure 7.7(a). The distance between the cones and implicitly between the saddle points is controlled by the rotation

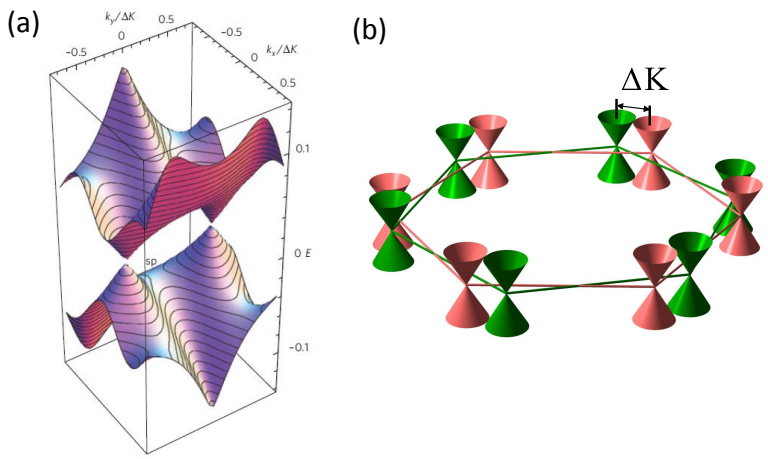

Figure 7.6: (a) Calculated dispersion for the low energy regime for θ= 1.79^o, $t_\perp$ ≈0.27eV. (b) Schematic illustration of the consequence of twist between the layers in momentum space. The cones corresponding to the two layers are separated by ΔK [90].

angle such that the distance in energy between the VHS depends monotonically on the angle. For the small angle regime, $2^o < \theta < 5^o$ the energy separation is: $\Delta E = \hbar v_F \Delta K - 2t^\theta$, where t^θ is the interlayer coupling.

Importantly, the rotation-induced VHSs are very robust and not restricted to the case of two layers. This is illustrated by the plot presented in Figure 7.7(b) where the density of states was calculated for the case of a trilayer: the top single layer of graphene is rotated above a Bernal-stacked bilayer. In this case, qualitatively the VHS are preserved. This allows observation of the VHS on multilayer graphene samples.

The theoretical curve [90] for the separation energies between the VHS is presented in Figure 7.7(c) indicating a monotonic increase with rotation angle. Experimentally, the STS taken on the Moiré patterns for different angles, 1.16^o,1.79^o, 3.5^o are presented in Figure 7.8(a),(b) and (c). The presence of two pronounced peaks is apparent and the separation between them is increasing with increasing the rotation angle, which is in good agreement with the theoretical curve as seen in Figure 7.7(c). For a given Moiré pattern the presence of the two peaks is

observed across the entire area of the sample that has the superpattern.

An interesting situation arises in the limit of small angles [90]. Figure 7.9 (a) shows the measured topography of the Moiré pattern corresponding to $\theta = 1.16^o$. The spectrum in this case is presented in Figure 7.9(c) showing the two VHSs separated by a small energy $\Delta E \approx 12meV$. It is known that when the Fermi energy is close to the VHS, interactions, however weak, are magnified by the enhanced density of states, resulting in instabilities, which can give rise to new phases of matter [174, 175, 176, 90]. This is consistent with the observation that the STS maps in Figure 7.9(b), taken at the energy of the singularity, suggest the formation of an ordered state such as charge density wave. Such localization by Moiré patterns is also predicted by theoretical calculations [169].

7.3 Renormalization of the Fermi velocity

While for sufficiently separated cones, the low energy electronic bands still describe Dirac fermions the slope of the Dirac cone is influenced by the Van Hove singularities, leading to a renormalized Fermi velocity.

Theoretically the equation describing the velocity renormalization is [163]

$$\frac{v_F(\theta)}{v_F^0} = 1 - 9(\frac{t_\perp^\theta}{\hbar v_F^0 \Delta K})^2 \tag{7.3}$$

where v_F^0 is the bare velocity, $v_F(\theta)$ is the renormalized value at an angle θ; the interlayer coupling is $t_\perp^\theta \approx 0.4t_\perp$ and $t_\perp$ is the interlayer coupling in the Bernal stacked bilayer. For large angles $\theta > 15^o$ the renormalization effect is small, but the velocity is strongly suppressed for smaller angles.

One way to probe the Fermi velocity is by measuring the quantized electronic spectrum in a magnetic field, the Landau levels. From the slope of their energy dependence on field and index [149] v_F is extracted .

Large angles

The results of STM and STS on twisted layer graphene with a large angle are presented in Figure 7.10. The topography image of the area where the pattern was identified is shown in Figure 7.10(a). The blue rectangle indicates the region where the data presented further was taken. Figure 7.10(b) shows the pattern, and the FT in the inset highlights the fact the both the superpattern and the graphene lattice are visible. In order to investigate the electronic properties of the twisted layers, the spectroscopy data as a function of magnetic field from B=2T to B=10T was taken as summarized in Figure 7.10(c). It is found that when the energies of the LL peaks are plotted as a function of the reduced parameter $sgn(N)\sqrt{|N|B}$ one obtains a linear dependence (Figure 7.10(d)). The extracted Fermi velocity is $v_F = (1.10 \pm 0.01)10^6 m/s$, which is again, consistent to a single layer graphene.

Thus, the low energy electronic properties for this system of large twist angle graphene layers are indistinguishable from those in a single layer.

Intermediate angles

Figure 7.11(a) shows the topography image on the surface of a CVD graphene film. The region highlighted is a region where the Moiré pattern in Figure 7.11(b) was identified. Two adjacent regions A and B are shown in the topography image of Figure 7.11(c). In region A, a Moiré pattern with period of $L = 4.0nm$ is resolved, while in region B, the pattern is not resolved indicating an unrotated layer (or a much smaller period not resolved within the experimental resolution). In the absence of a magnetic field, within the energy range $-600meV < E < 600meV$, STS shows two VHS in region A and a V-shaped spectrum for region B.

In magnetic field, from B=1T to B=8T in both regions STS shows LL sequences as plotted in Figure 7.12(a) and (b) for region A and B respectively. From the dependence of the LL energies on field and index (Figure 7.12(c)(d)) we see that the LL sequences are those specific to massless Dirac fermions with

different Fermi velocities: $0.87\text{x}10^6 m/s$ and $1.10\text{x}10^6 m/s$ for regions A and B respectively. This already indicates that the twist angle can have a strong effect on the electronic spectrum and can lead to renormalization of the carrier velocity.

Very small angles

The regime of very small angles, $\theta < 2^o$ is more complex since the VHSs become so dominant that massless Dirac fermions no longer describe the electronic states. Furthermore, in magnetic field, the lengthscale of the cyclotron orbits, magnetic length, becomes comparable to the size of the pattern.

Figure 7.13 presents the case of two patterns that are created by rotation angles $\theta = 1.2^o$ and $\theta = 1.8^o$. The topographic images of these two cases are shown in Figure 7.13 (a) and (b) respectively. For the case of $\theta = 1.2^o$ the separation between VHS is $\approx 12meV$. The evolution of the spectrum with magnetic field, presented in Figure 7.12 (c) shows the comparison between the bright and dark regions of the superpattern.

At higher fields, at energies near the VHSs, several peaks develop, but one cannot identify the sequence specific to the sequence expected for single layer graphene. The situation is similar for $\theta = 1.8^o$ as indicated by Figure 7.12 (d) where the field dependence of the spectrum is presented from B=0T to B=12T.

Summing up, one can now plot the theoretical curve described by Equation 7.3 together with the velocities found experimentally as shown in Figure 7.14. At large angles the velocity is not renormalized, for angles around 3^o a renormalization of $\approx 20\%$, while for smaller angles the situation is more complex.

It is important to note that the mechanism for renormalization of the Fermi velocity in the presence of VHS is different from the case of graphene flakes on graphite [69]. In the twisted layers the renormalization is a sensitive function of the misorientation angle. In contrast, the velocity renormalization observed in the the case of graphene on graphite is due to electron-phonon interaction [69].

For a more detailed analysis of the Fermi velocity one can separately calculate

v_F for the electron and hole side of the spectrum. The results for the case of large angle in Figure 7.10(d) together with the data from regions A and B of Figure 7.12 are presented in Figure 7.14(b). In all cases the electrons have a higher velocity than the holes. In the large angle case, where the averaged velocity is $1.1 \times 10^6 m/s$ we obtain a value of $1.2 \times 10^6 m/s$ for electrons and $1.02 \times 10^6 m/s$ for holes. In the case of region A, the electrons have $1.0 \times 10^6 m/s$, the holes have $0.76 \times 10^6 m/s$, and the average is $0.87 \times 10^6 m/s$. The origin of this asymmetry could be related to an enhancement of next-nearest neighbor hopping in the case of twisted layers.

In the previous discussion regarding velocity renormalization we studied the Landau quantization in the twisted layers systems below the energy scales of the VHS. Recent theoretical predictions [177, 178, 179, 180] investigate the full LL spectrum. For a given rotation angle one regime is below the energy range of the VHS. In this case it is predicted in agreement with the previous experimental findings that the LL sequence of a twisted bilayer is the one of Dirac Fermions with the renormalized Fermi velocity and double the degeneracy. Above the VHS however the degeneracy of the two layers is broken.

Experimentally for medium angles we can extend the energy range for STS to include the VHS as presented in Figure 7.15 for the regions (a) and (b) respectively of Figure 7.12 and Figure 7.11. The data is suggestive of the fact that in Figure 7.15(b) at larger energies, closer to the VHS, the LL sequence is strongly affected by the presence of the VHS. To compare with the theoretical predictions and study the degree of splitting, cleaner samples, with LL sequences well defined at lower fields are necessary.

The results obtained on Moiré patterns on CVD graphene and graphite differ from the ones on epitaxially grown graphene on SiC [99, 181] which report a single layer graphene spectrum regardless of the twist angle. One clue towards understanding these results can be found in the unusual presence of a continuous

atomic honeycomb structure across the entire Moiré superstructure in the case of epitaxial graphene. This is in contrast to Moiré patterns generated by two rotated layers where one sees a correlation between the Moiré pattern and the atomic structure which changes from triangular, to honeycomb, or in between the two, depending on the local stacking within the superpattern [168, 90].

If in addition to the twist of the top most layer, a Moiré pattern is present under the first layer (layer 2 rotated with respect to layer 3), it is expected that a complex superstructure involving several Moiré patterns will appear. This is the case in some of the experiments reported on epitaxially grown graphene on SiC [182]. In the case of the CVD graphene samples or graphite such multiple Moiré patterns were not observed. Therefore, the previously discussed features (VHS, reduction in Fermi velocity) are consequences of twisting only the top most layer with respect to the underlying single layer graphene or Bernal-stacked multilayer graphene.

Recently also Raman experiments have been used to investigate twisted layers [183, 183, 184, 185, 186] confirming the presence of VHS and renormalization of the velocity for intermediate angles.

Electrical transport in twisted bilayers [131, 130, 187] in the quantum Hall regime confirmed that in the case of large angle twist the two layers indeed decouple and behave as single layer graphene in the low energy regime.

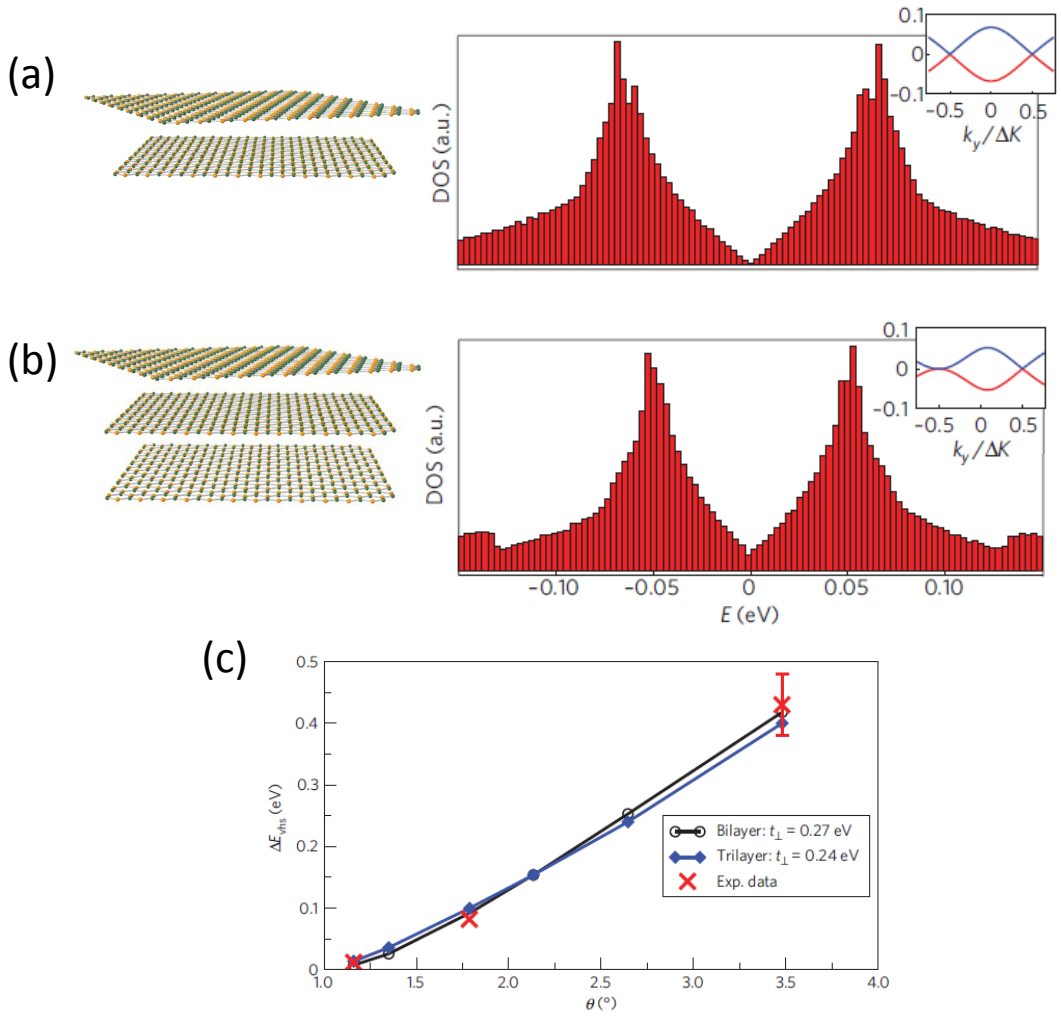

Figure 7.7: (a) DOS calculated for the dispersion in Figure 7.6(a). (b) DOS calculated for the case of single layer rotated above a bilayer. (c) Theoretical curve and experimental values for the dependence of the the energy between VHS and rotation angle [90].

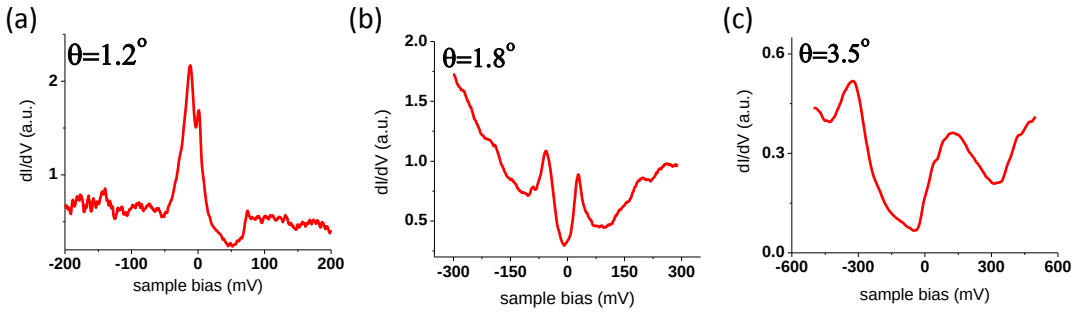

Figure 7.8: (a),(b),(c) STS curves taken on patterns for different rotation angles, 1.16^o,1.79^o, 3.5^o

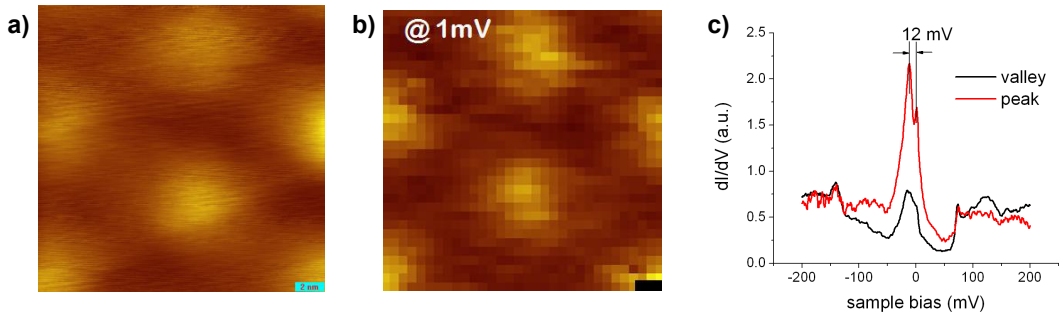

Figure 7.9: (a)Topography of a Moiré pattern corresponding to rotation angle $\theta = 1.16^o$. (b) dI/dV map taken at the area in (a) at energy E=1meV. (c) STS on the peaks and valleys of (a).

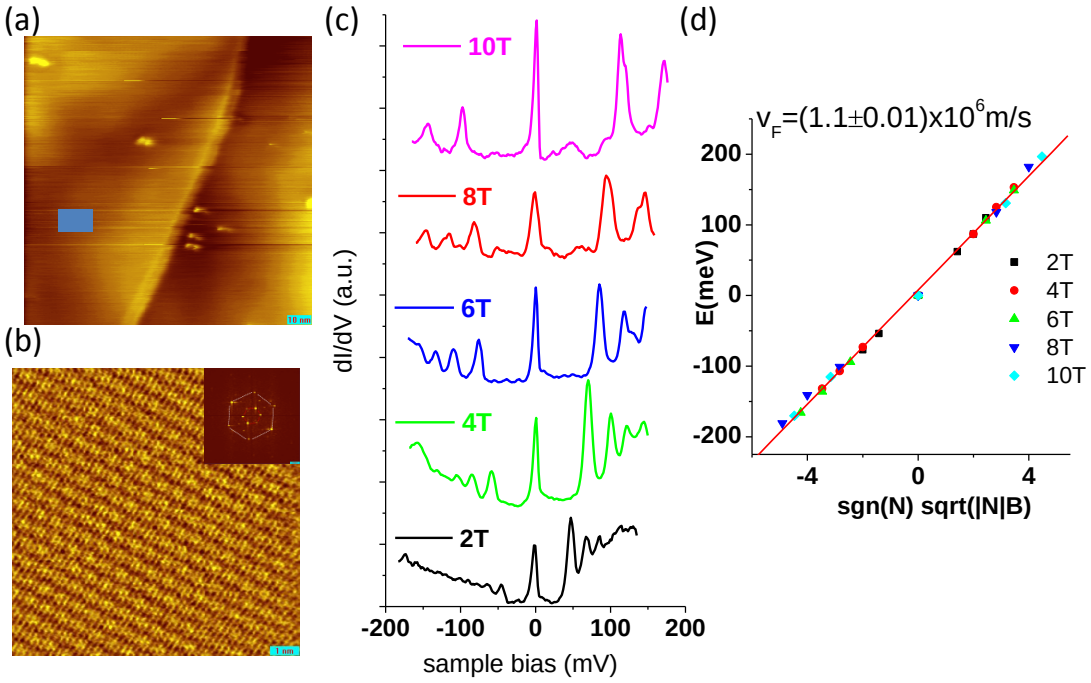

Figure 7.10: (a) STM topography of a region with a large angle Moiré pattern, $\theta = 21.8^o$. The blue rectangle indicated the position where the data in (ac) was taken. (b) Atomic resolution image of the superpattern observed in the region indicated by the blue rectangle in (a). The corresponding period is $L = 0.7nm$. Inset: Fourier Transform showing both the superlattice and the atomic lattice rotated with respect to each other (c) STS for indicated magnetic fields showing the sequence of Landau Levels measure in the point indicated in (a). d) Linear energy dependence of the LLs in (c) on the reduced parameter $sgn(N)\sqrt{|N|B}$.

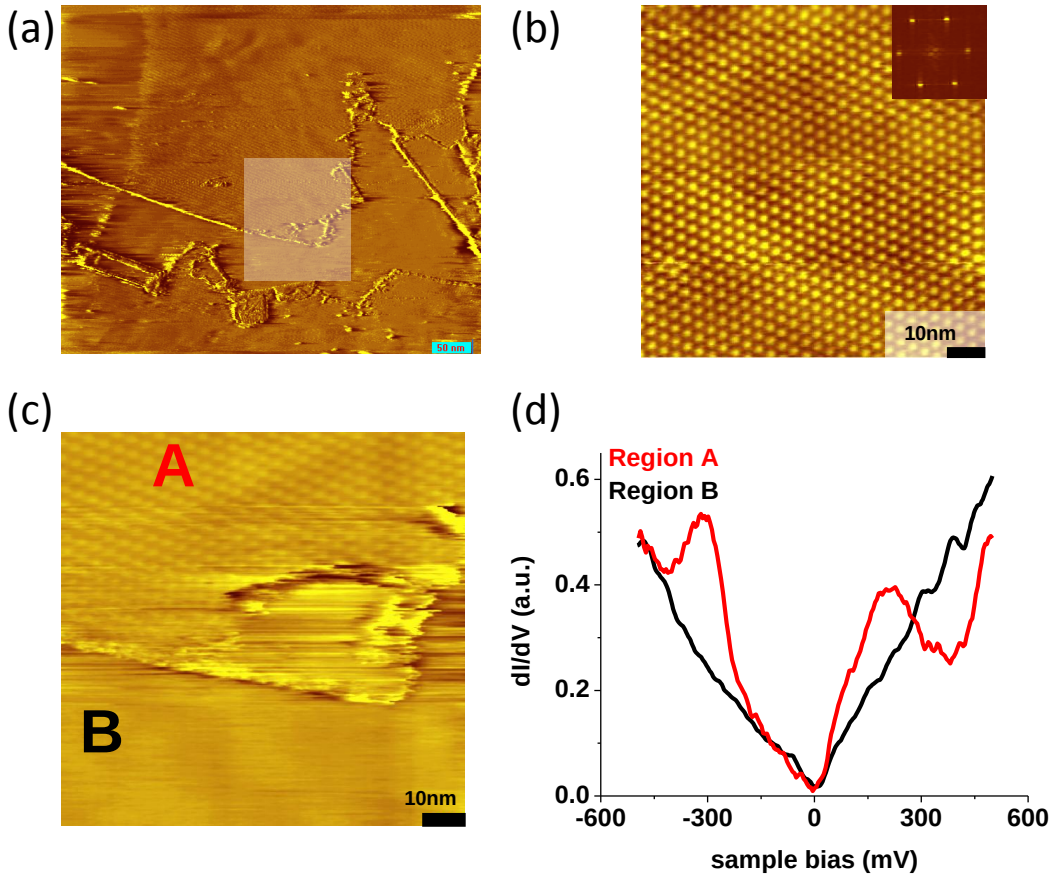

Figure 7.11: (a)STM topography image of a region where the Moiré pattern was observed in the highlighted square. (b) Topography image taken at the region with a Moiré pattern. The inset represents the FT of the patter. (c) Topography image showing the border of the superpattern , A, with another region on the graphene film, B. (d) STS comparison between the two regions; region A shows VHS.

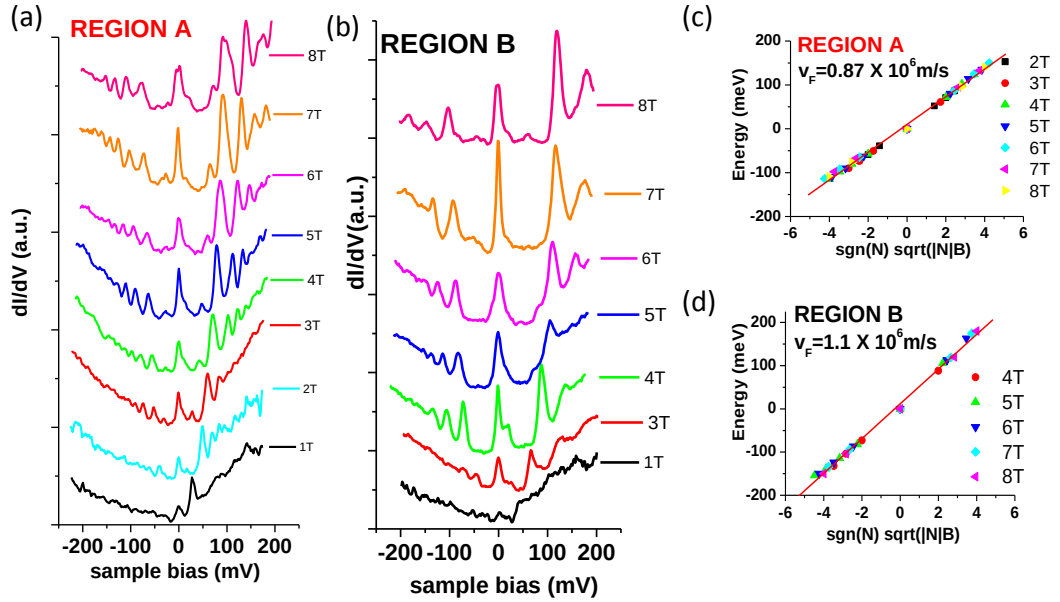

Figure 7.12: (a),(b) STS on region A and B respectively of Figure 7.11(c) in the presence of perpendicular magnetic field B=1T to B=8T. (c),(d) Energies of the LLs in (a) and (b) versus $sgn(N)\sqrt{|N|B}$

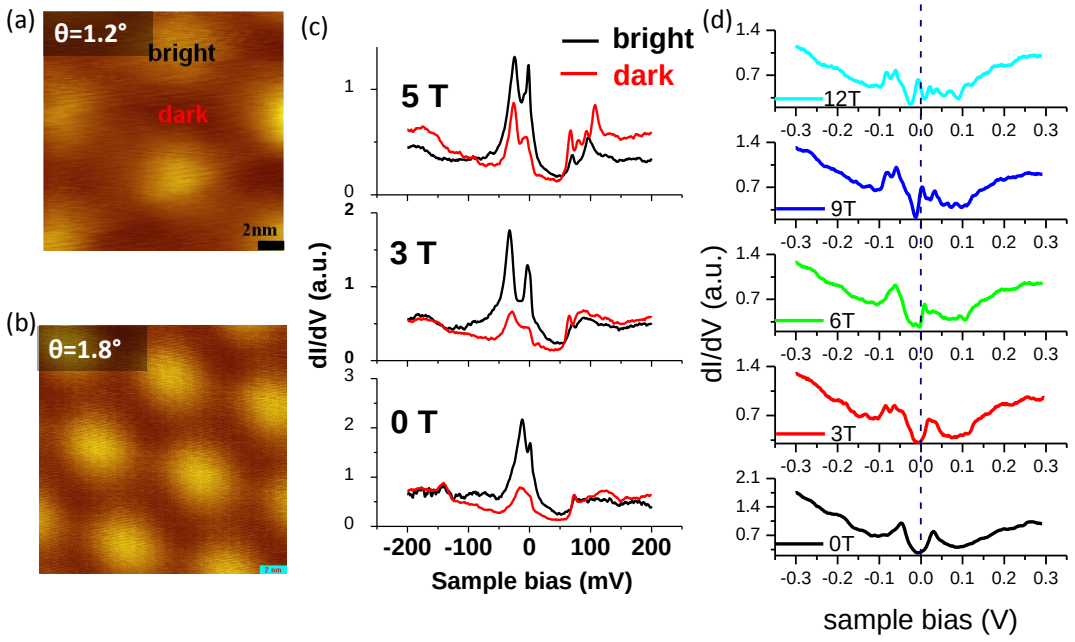

Figure 7.13: (a),(b) Topography images of superpatterns corresponding to rotation angles $\theta = 1.2^o$ and $\theta = 1.8^o$ respectively. (c) STS for increasing values of magnetic fields for the region in (a) for the two situations of bright and dark regions of the superpattern. (d) STS for increasing values of magnetic fields for taken at the region in (b).

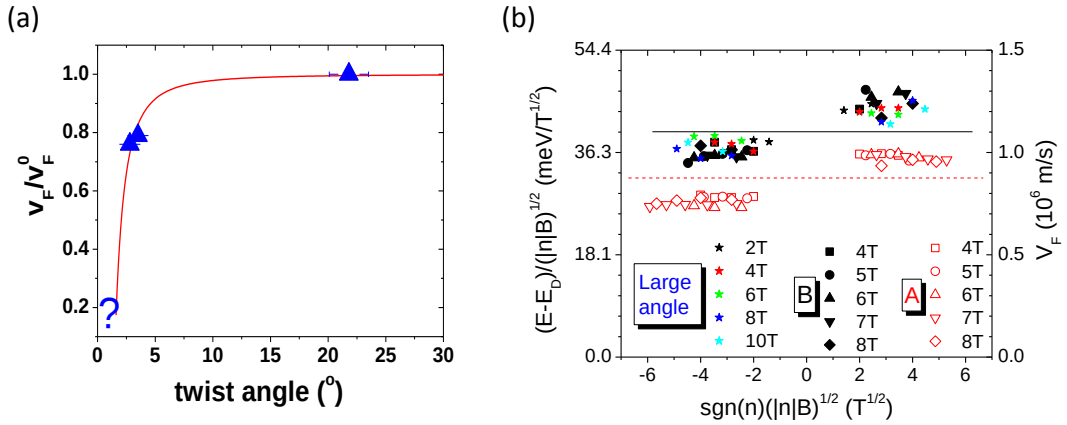

Figure 7.14: (a) Theoretical curve describing the velocity renormalization in Equation 7.3 together with experimental data (blue triangles) (b) Electron-hole asymmetry of Fermi velocity in different sample regions is independent of field or level index. Symbols are the values of the Fermi velocities.

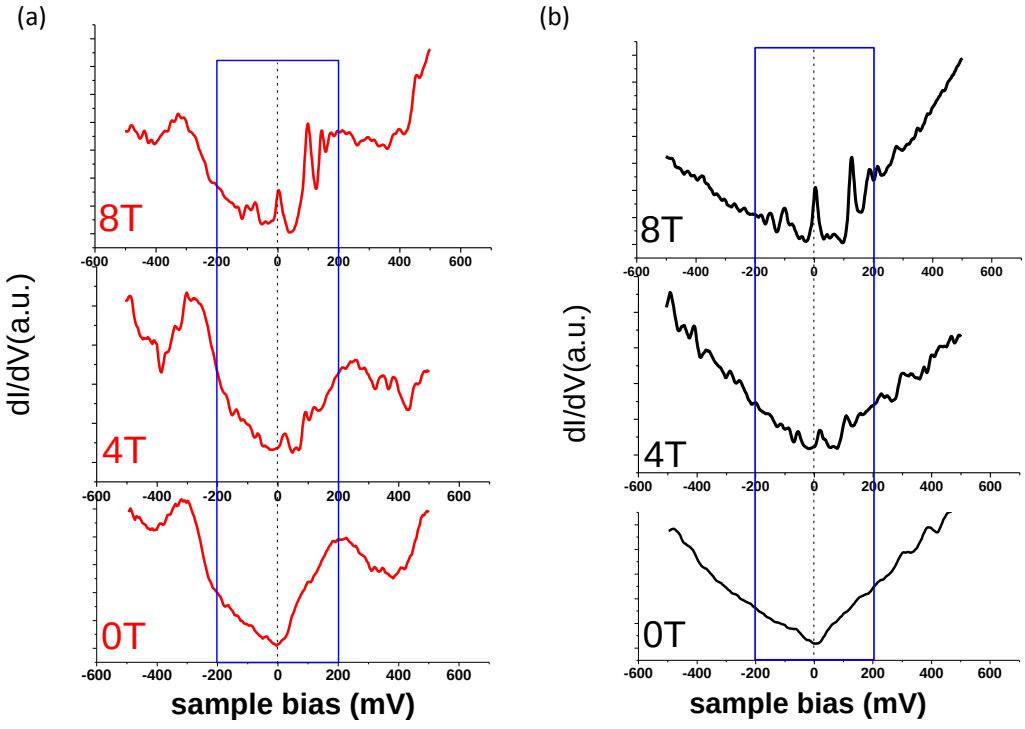

Figure 7.15: (a),(b) STS for larger energy sample bias range for regions A and B in Figure 7.12 for different magnetic fields. The energy range presented before is highlighted by the blue rectangle.

Chapter 8
Electronic properties at grain boundaries

Topological defects (ex. missing atoms, dislocations, grain boundaries etc.) are inherently present, due to growth methods, in any crystalline material such as graphite. Early STM experiments have already identified that wire-like periodic structures often observed on the graphite surface represent the boundaries between two misoriented grains of the crystal [188, 189, 190, 191, 192]. Although these studies analyzed the topography features associated with the presence of a grain boundary, only with the recent interest in graphene theoretical [193, 194, 195, 196, 197] and experimental work [198, 199, 200] addressed questions regarding the electronics properties .

Furthermore, recent experimental efforts targeted at growing wafer-size graphene found that the films grown by chemical vapor deposition method are polycrystalline. Transmission electron microscopy studies visualized the atomic details of such defects [201, 202, 203] and demonstrated that the typical sizes of the single crystal domains are several microns with a large range of misorientation angles between grains.

The presence of such grain boundaries can affect the transport properties [194, 63] and thus understanding their electronic properties is necessary. Magnetic properties can also be affected by grain boundaries in graphite/graphene films [204, 205, 199].

In this chapter Scanning Tunneling Microscopy and Spectroscopy experiments at low temperature and in magnetic field are used to characterize the electronic

states near grain boundaries on the surface of graphite. Topographic surface maps show the grain boundaries as narrow stripes within which the lattice is reconstructed into a periodic pattern whose period is determined by the relative orientation between adjacent grains. In spectroscopy the grain boundaries produce sharp peaks in the density of states at energies that are characteristic of the twist angle between adjacent grains. Spatial maps of the density of states at these peak energies show that the peaks correspond to electronic states that are localized on the grain boundaries. Measurements of these localized electronic states, their evolution with magnetic field and twist angle between grains are presented. The experimental results are also compared with theoretical density functional theory (DFT) calculations. Parts of this chapter follow closely the text in [206].

8.1 Grain boundaries on the surface of graphite

8.1.1 Topography

Grain boundaries (GB) are interfaces between two misaligned grains in a material. The family of possible grain boundaries can be theoretically classified and a sketch of one of the simplest realized grain boundaries in graphene is presented in Figure 8.1(a). This is a symmetric GB so that the left and right grains are rotated by the same amount with respect to the boundary, it is composed of sequences of alternating heptagons and hexagons and it can be thought of as an array of dislocations (denoted by T in the figure). DFT calculations [207] suggest that this is one of the most stable grain boundaries in graphene.

To characterize a GB between two graphene grains we use the following convention depicted in Figure 8.1(b): a vertical axis is drawn along the boundary and the corresponding horizontal axis is perpendicular to it. The angle corresponding to the grains to the left and right with respect to the horizontal axis are θ_L and θ_R respectively. The angle that will characterize the boundary is $\theta = \theta_L + \theta_R$

We use STM topographic images to identify a grain boundary and STS to learn about the local density of states both with and without magnetic field. In topography images, grain boundaries appear on the surface of graphite as long, continuous wires similar to the one shown in Figure 8.1(c) and (d). Note that in Figure 8.1(c) perpendicular to the boundary there are two steps in graphite which can be easily distinguished from a GB by the fact that the atomic lattice is not continuous across them.

Importantly, we can already infer from the topography images that the grain boundaries are not only restricted to the top layer of graphite. If this was not the case, we would necessarily observe a Moiré pattern to the left of right of the boundary since due to the presence of the boundary the stacking can no longer be Bernal between the top and second layer. The absence of the Moiré pattern, therefore, suggests that rather than a grain boundary at the surface one has a plane of grain boundaries going deep into the graphite crystal [199]. This could have an effect on the electronic properties of the observed boundaries and it will be discussed in a later section.

When zooming in on a GB we often find a periodic pattern as the one shown in Figure 8.1(e) which was taken on the grain boundary presented in Figure 8.1(c). In this case, the rotation angle between the grains is: $\theta = \theta_L + \theta_R \approx 11^o + 10^o \approx 21^o$. This is most likely the symmetric structure presented in Figure 8.1(a). In comparison, the theoretical calculation for the 21^o boundary considering a bias voltage $V_b = 300meV$ is presented in Figure 8.1(f) and it is in good agreement with the experimental topography.

Similarly to the case of Moiré patterns the period of the boundary pattern, D, is given by the relationship:

$$D(\theta) = \frac{a}{2sin(\frac{\theta}{2})} \tag{8.1}$$

where $a \approx 0.246nm$ is the lattice constant of graphene and θ is the angle of

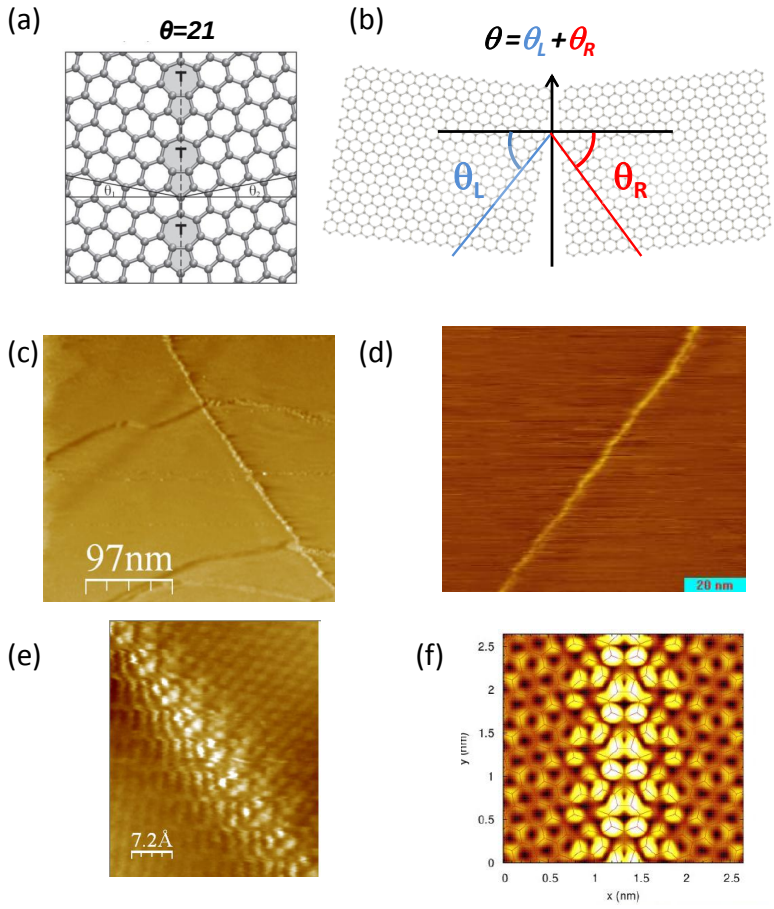

Figure 8.1: (a) Schematic of the atomic details at a grain boundary for $\theta = 21^o$ where the boundary is a sequence of heptagons and pentagons (Adapted from [207]). (b) Schematic of the convention for measuring the angle of a grain boundary. (c),(d) Topography image of a grain boundary on the surface of graphite. (e) Topography image of a grain boundary $\theta = 21^o$ (V_b=300meV, I_t=20pA). (f) The theoretical calculation for a grain boundary $\theta = 21^o$ at bias voltage $V_b = 300meV$.

the grain boundary as defined before. Thus, for small tilt angles, the periodicity is very large, while for large angles it becomes smaller.

This is observed experimentally as exemplified in Figure 8.2 where measured grain boundaries at different angles are presented together with their respective atomically resolved GB as insets. For $\theta = 10^o$ the measured grain boundary has a periodicity of $\approx (1.8 \pm 0.3)nm$ which is in agreement with the expected $D(10^o) = 1.4nm$. For $\theta = 21^o$ the experimental value $(0.7 \pm 0.3)nm$ also in good agreement with $D(21^o) = 0.6nm$. From the periodicity and rotation angle, the

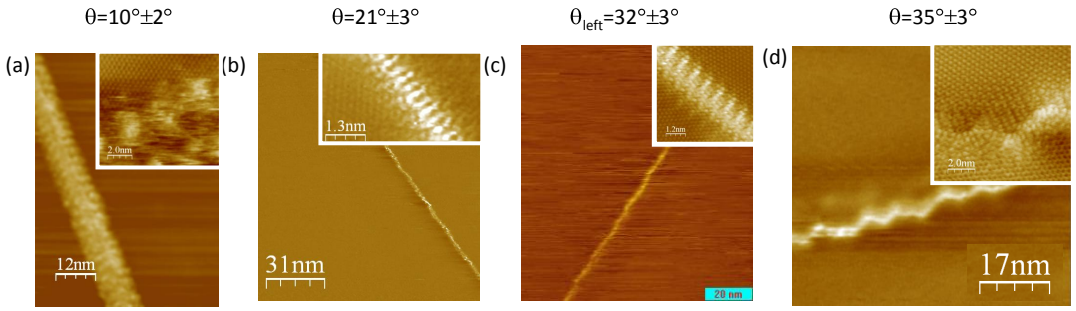

Figure 8.2: (a)-(d) STM topographs of grain boundaries on the surface of graphite for different angles as labeled. The insets are respective atomically resolved boundaries.

boundary with $\theta = 32^o$ in Figure 8.2(c) is most likely also one corresponding to an arrangement with heptagons and pentagons. This, together with the symmetric GB, $\theta = 21^o$, are predicted to be the most energetically favorable boundaries [207].

Experimentally we find that on the surface of graphite the most abundant grain boundaries are irregular such as the one in Figure 8.2(d) which appears as a zig-zag pattern. Such boundaries are referred to as amorphous and they are a result of additional disorder (such as relaxation of the lattice in the boundary) beyond the simple model of a periodic array of dislocations [195]. The relaxation of the lattice allows for for an extension of the available orientations of the grains.

Furthermore, when one images a grain boundary it is often the case that only some portions of the boundary are free of disorder, while for others the tunnel junction is not stable. This can be explained by the fact that the grain boundaries have an enhanced chemical reactivity [208].

8.1.2 Electronic properties

Previous STM/STS experiments addressing the question of electronic spectrum of grain boundaries on graphite find that typically peaks in the density of states are associated with the presence of a GB [198, 199]. However, direct evidence of

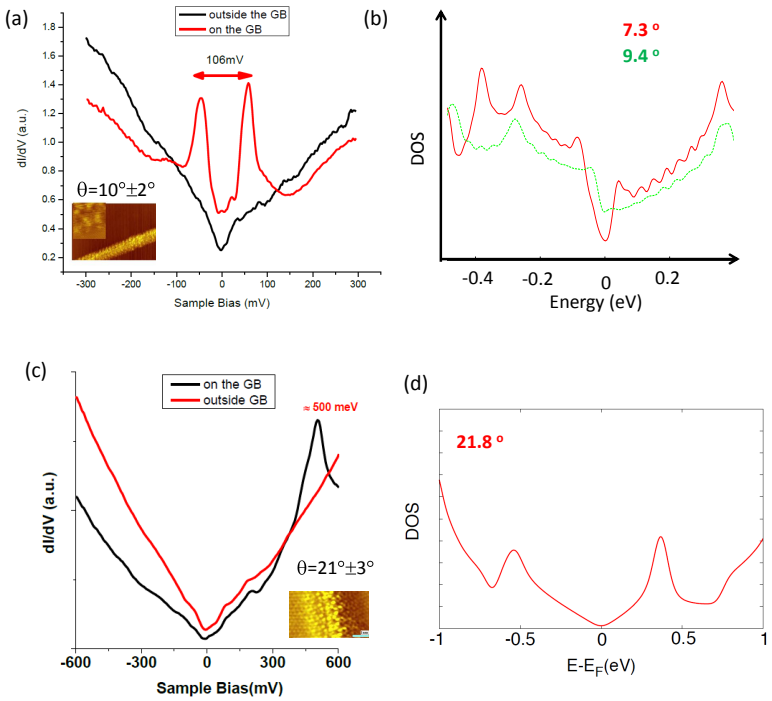

Figure 8.3: (a) STS spectra on the grain boundary (red curve) and outside the grain boundary on the graphite surface (black curve) for the grain boundary in the inset $\theta = 10^o$. The separation between the observed peaks on the grain boundary is $106meV$. (b) Theoretical calculation for the DOS versus energy in the case of grain boundaries of $\theta = 7.3^o$ (red curve) and $\theta = 9.4^o$ (green curve). (c) STS spectra on the grain boundary (black curve) and outside the grain boundary on the graphite surface (red curve) for the grain boundary in the inset $\theta = 21^o$. The peak measured on the grain boundary is situated at $\approx 500meV$. (d)(b) Theoretical calculation for the DOS versus energy in the case of grain boundaries of $\theta = 21^o$ [206].

the presence of new electronic states that are associated with the GB is lacking.

In the following we present STS results on grain boundaries of different angles and a comparison with theoretical DFT calculations.

In Figure 8.3(a) the data taken on the grain boundary in Figure 8.2(a) is presented. The spectroscopy on the grain boundary shows two very pronounced peaks separated by $E \approx 106mV$. We note in connection to the discussion regarding Van Hove singularities on Moiré patterns, that if the origin of these peaks were VHS [164] the angle would have to be much smaller, $\theta \approx 2^o$ and therefore the period of the structure much larger $\approx 10nm$. Therefore, it is the presence

of the grain boundary that is most likely responsible for the existence of the two peaks in the spectrum. In contrast, outside the grain boundary, the spectrum (black line) does not display any peaks, but it is approximately V-shaped, as is typical for a graphite surface.

Theoretical ab initio calculations for the density of states in the cases of two angles close to the measured 10^o are presented in Figure 8.3(b). The green line corresponds to $\theta = 9.4^o$ and the red line to $\theta = 7.3^o$. The two peaks close to $50 - 100meV$ resemble the experimentally measured spectrum.

The spectra on the grain boundary and off the boundary for the case of $\theta = 21^o$ are compared in Figure 8.3(c). In this case we find that while outside the grain boundary the spectrum is again typical of the graphite surface and has no peak features, on the boundary a strong peak is present on the electron side at $\approx 500meV$.

The theoretical calculation in Figure 8.3(c) does indeed show for the 21^o GB the presence of a peak at $\approx 400 - 500meV$, however the striking difference is the presence of an additional peak at the negative energy side of the spectrum. One possible explanation for the absence of this peak in experiment could be that it is located at even higher energies than $-800meV$. Another scenario could be related to the key difference between the experimental data presented and the theoretical consideration: while the experiments are performed on graphite surface, the theory only takes into account single layer graphene joined at a grain boundary. So the number of layers and the fact that the grain boundary can be layers deep could affect the electronic structure.

In order to understand what is the influence of such a more realistic scenario, a calculation of the DOS was done for a stack of 2 layers as shown in the inset in Figure 8.4. The first important observation is that it is possible to stack two grain boundaries on top of each other while preserving the Bernal stacking for graphene on both side as illustrated. The resulting DOS shown in Figure 8.4

(red), is compared to the single layer case (green). The peak on the electron side is in fact more robust than the one on the hole side. This suggests that going to larger numbers of layers, the changes in nearest neighbor hoping could result in an electron -hole asymmetry which could explain the discrepancy between experiment and theory.

In the case of the boundary $\theta = 32^o$ (Figure 8.2(c)) we also observe a peak at $\approx 500meV$ on the positive energy side of the dI/dV which is in good agreement with the theoretical calculations [207]. For this case also the spectrum is asymmetric and shows a peak on the hole side.

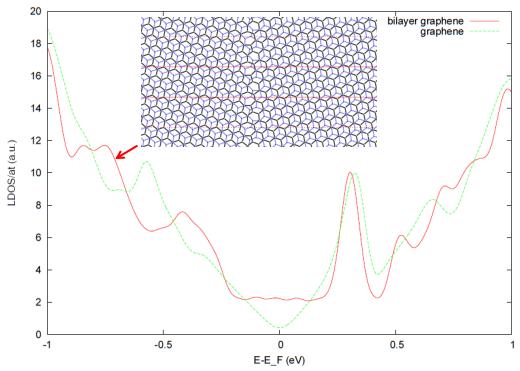

Figure 8.4: Theoretical calculation for the case of a constructed model of 21^o grain boundary in bilayer graphene. The inset is the atomic arrangement in such a system. The DOS plot compared the calculation for this bilayer case (red curve) as well as for comparison for a single layer case (green curve) [206].

To understand the spatial variation of the peak feature associated with the spectrum on the GB, local dI/dV maps were taken. The spectrum was acquired on a grid of points across the region having a grain boundary and for a given energy the value for the dI/dV was plotted. Such maps are presented in Figure 8.5 where the bright yellow represents high values of the dI/dV and dark brown represent low value.

On the hole side of the spectrum the map does not change much compared to the one presented in Figure 8.5(a) at $-400meV$. On the electron side for energies around the peak, a high intensity is developed at the region of the boundary as

seen in Figure 8.5(a) for $456meV$ and $505meV$ and it disappears at even higher energies $700meV$. This shows that the states that give rise to the peak in the DOS at $\approx 500meV$ are localized in space at the position of the grain boundary. Also this shows that the peak feature is indeed present across the entire grain boundary.

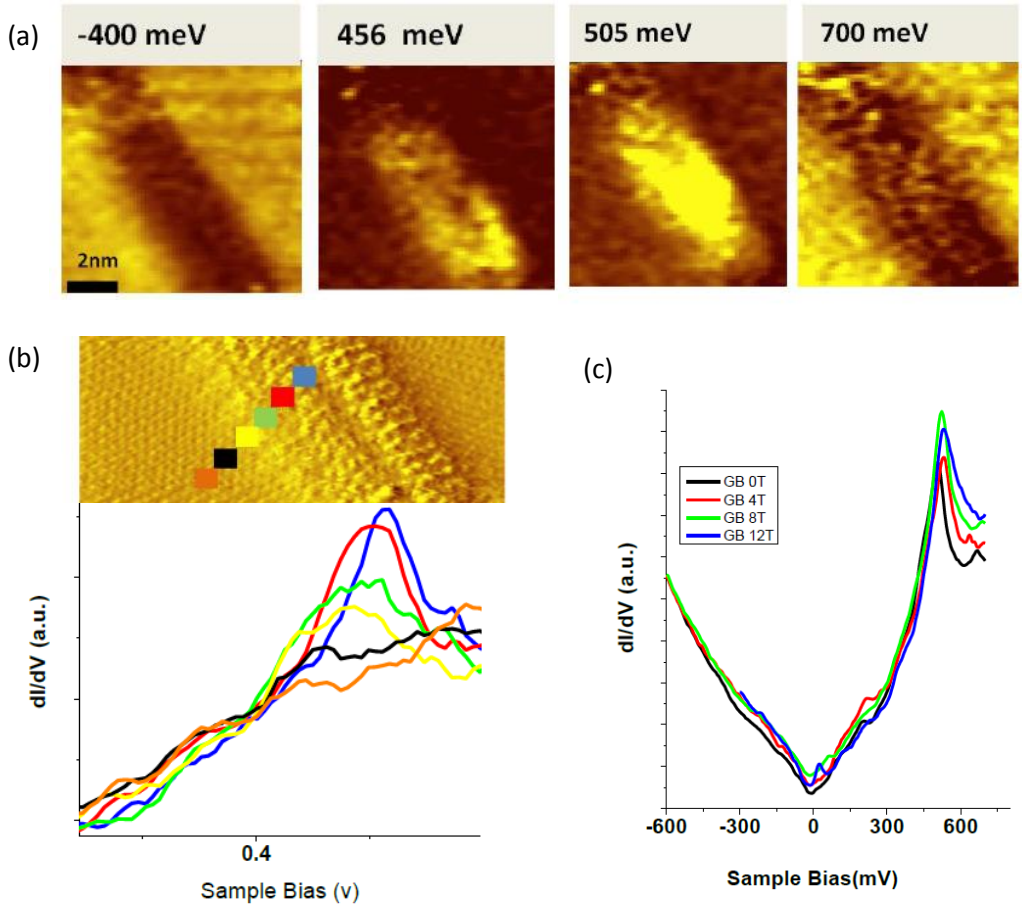

Figure 8.5: (a) dI/dV maps for the grain boundary $\theta = 21^o$ at the corresponding energies. (b) Dependence of the STS spectrum on the distance away from the boundary. The topographic image shows the location of the boundary together with the points where the spectra were taken. The corresponding dI/dV spectra are shown below. (c) Dependence of the STS spectra at the grain boundary on magnetic field for $B = 0T, 4T, 8T, 12T$

In addition we can look at the peak intensity as a function of position with respect to the boundary as shown in Figure 8.5(b). The topographic image shows the grain boundary together with the points where the STS was recorded away

from the boundary and close to the boundary. The colors of the STS curves presented match the color in the topographic map. We find that the intensity of the peak is decreasing away from the grain boundary on length scales of nm which is also consistent with the fact that the peak in only localized at the boundary (Figure 8.5(a)).

Theoretical predictions suggest that the peak should decay exponentially away from the boundary [207, 195] and this is consistent with our observation: within $1-2nm$ the peak corresponding to the grain boundary completely disappears in the graphite regions. We note that such localized states were observed also on the more irregular grain boundaries of Figure 8.2(d), however for a particular energy only patches of the irregular boundary will have localized states. This is likely the due to the fact that different sections of the GB have different tilt angle and thus localized states at different energies corresponding to the respective angle.

Motivated by some theoretical [209, 210, 211] and experimental [199] evidence hinting at the presence of magnetism in graphene due to defects, adatoms etc. is also interesting to investigate what happens in magnetic fields to the electronic spectrum in grain boundaries.

The STS spectra obtained for magnetic fields 4T, 8T, 12 T are presented in Figure 8.5(c). Within the experimental resolution ($\approx 20meV$), we find no change in the spectrum, the major feature remains, for all fields, the discussed peak around the energy $500meV$.

In summary, STM/STS was used to characterize the electronic properties of grain boundaries on the surface of graphite. Using topography images the grain boundaries are identifies as narrow structures that have, when zooming in, periodic patterns with period determined by the relative orientation of the adjacent grains. Using STS we find that the signature of the grain boundaries are sharp peaks at energies specific to the angle characterizing the GB. The position in energy of such states is in agreement with the theoretical predictions. The

fact that the states that produce the peaks in the DOS are localized at the grain boundaries is demonstrated experimentally by measuring the spatial maps of the density of states. Understanding the electronic properties of the grain boundaries is important for predicting the transport properties of large scale graphene films grown by chemical methods and potentially open new opportunities for the design of graphene based electronic devices.

Chapter 9
Concussions and outlook

In summary, the experiments described in this thesis are aimed at understanding the electronic properties of graphene using scanning tunneling microscopy and spectroscopy both without and in the presence of a magnetic field.

Electronic properties of graphene with different degree of disorder

Directly relevant to understanding electronic devices are graphene samples on insulating substrate where, due to substrate-induced potential fluctuations, it is found that the electronic properties are affected by disorder. The surface of graphene is rippled, follows the corrugations of the substrate, and the density of states deviates from a perfect V-shape. In magnetic field, the quantized energy levels are well defined only above a critical field which corresponds to a magnetic length smaller than the typical disorder lengthscale.

We were able to access the carrier density dependence of the spectrum and we have observed pinning of the Fermi level within the LL which was filled. These experiments give access to the physics of graphene in the quantum Hall effect regime beyond the states at the Fermi level as is the case in transport experiments.

In addition, in areas where the charged impurities are isolated we investigated their effect on the LL spectrum. We find that the Coulomb potential created by charged impurities can lift the degeneracy of the Landau levels. Using the back-gate voltage we tune the strength of the impurity potential.

Reducing the substrate-induced disorder allows one to explore intrinsic graphene

physics. Towards this goal, currently we have fabricated graphene devices placed on hexagonal boron nitride flakes which are less intrusive.

On a minimally intrusive substrate, decoupled graphene flakes on graphite, we observed a distinctive signature of massless Dirac fermion quasiparticles: a V shaped density of states that vanishes at the Dirac point, and in magnetic field a sequence of sharp quantized Landau level sequence that is characteristic of massless Dirac fermions. In this system we were able to determine the effect of interlayer coupling in regions where the graphene flakes are weakly coupled to the substrate.

One of the biggest challenges for doing STM on graphene devices is finding micron size samples without optical microscope access at low temperatures. That was overcome by developing a method based on capacitance signal between tip and sample.

Electronic properties of twisted graphene layers.

Both in graphite and in graphene grown by chemical vapor deposition (CVD) one can find Moiré superpatterns created by the rotation of the top graphene layer with respect to the rest. STM/STS allowed characterizing the influence of the twist between layers on the band structure by measuring both the angle (from the period of the pattern) as well as the density of states.

The Dirac cones corresponding to the two twisted layers will rotate with respect to each other in momentum space and will hybridize at to two saddle points. These saddle points will give rise to two Van Hove singularities in the density of states. We experimentally demonstrate their existence and their monotonic increase in energy separation as a function of rotation angle.

Moreover, when measured in the presence of magnetic field, from the spacing and field dependence of the LL, the Fermi velocity is found to depend strongly on the twist angle. For intermediate angles the velocity is renormalized, for angles close to 30° the velocity is unchanged. An interesting regime is reached at very

small rotation angle ($<2^\circ$) where the spectra are dominated by twist-induced van Hove singularities.

Electronic states near grain boundaries on the surface of graphite were characterized. Topographic surface maps show the grain boundaries as narrow stripes within which the lattice is reconstructed into a periodic pattern whose period is determined by the relative orientation between adjacent grains. In spectroscopy the grain boundaries produce sharp peaks in the density of states at energies that are characteristic of the misorientation angle between adjacent grains. Spatial maps of the density of states at these peak energies show that the peaks correspond to electronic states that are localized on the grain boundaries. We present measurements of these localized electronic states, their evolution with magnetic field and misorientation angle between grains. The experimental results are compared with theoretical calculations.

Outlook

Following up on the ideas of the results presented above, the immediate interesting questions that need to be addressed are related to striving to minimize the effects of disorder and probing intrinsic properties of graphene.

Mechanically exfoliated graphene samples onto Si/SiO_2 can be significantly improved by removing the oxide under graphene as demonstrated by transport experiments [87]. Such clean samples would unveil electron correlation effects in graphene. Lifting the degeneracies of the Landau levels (LL) leads to formation of intriguing broken-symmetry states which so far have only been addressed by electrical transport measurement and a clear understanding of their nature is missing. To complement the transport techniques, by spatially resolving the density of states and the wave functions of the LL, STM/STS would give more insight into the origin of the correlated electronic states.

The gapless band structure of graphene is protected by the lattice symmetries and therefore any local modifications of the lattice will locally break the

symmetry and alter the band structure. Hence, vacancies, adatoms, edges, grain boundaries, etc. are likely to induce the formation of various interesting electronic states. In particular of great importance to the physics of the Quantum hall effect are **graphene edges**. The two high symmetry crystallographic directions in graphene are armchair and zigzag. These two types of edges have different properties due to the different boundary conditions that they impose on the wave function. For the zigzag case the wave function vanishes on one sublattice, while for the armchair it vanishes on both sublattices. The zigzag edges have attracted attention because they are expected to have localized surface electronic states Using combined STM and magneto-transport, one can envision a method to control and study graphene edges in the following way. It was observed that upon current annealing of graphene devices (passing a large current through the graphene device) their quality can improve significantly. Often, by scanning electron microscope investigations, the change in quality was linked to edge reconstruction [212].

New experimental developments described in the previous chapters make it possible to create stacked **heterostructures of 2D materials** that can have novel properties. Thus far, this direction is both theoretically and experimentally in its infancy. One simple example is depositing graphene layers of different thicknesses on a superconducting material With the use of nanofabrication techniques, these stacks can be made into gated devices introducing an extra knob, the charge carrier density. The heterostructures offer a very large parameter space and therefore are very promising for the design of materials with unique physical properties.

The novel findings in this thesis about **tuning the electronic properties of graphene stacks** by twisting them away from Bernal stacking together with the experimental possibility of fabricating heterostructures, open up interesting possibilities of exploring the properties of such new systems. In particular the

presence of Van Hove singularities at energies that are within reach using electrostatic gating, are particularly promising for observing new states of matter (superconductivity, charge density waves etc.) in graphene.

Chapter 10
List of abbreviations

AFM Atomic Force Microscope

ARPES Angle Resolved Photoemission Spectroscopy

BN Boron Nitride

CVD Chemical Vapor Deposition

CNP Charge Neutrality Point

DOS Density Of States

DFT Density Functional Theory

DP Dirac Point

FT Fourier Transform

IQHE Integer Quantum Hall Effect

FQHE Fractional Quantum Hall Effect

HOPG Highly Oriented Pyrolitic Graphite

LDOS Local Density Of States

PMMA Poly(methyl methacrylate)

PVA Polyvinyl alcohol

STM Scanning Tunneling Microscopy

STS Scanning Tunneling Spectroscopy

SG Suspended Graphene

TEM Transmission Electron Microscope

References

[1] K. S. Novoselov. Nobel lecture: Graphene: Materials in the flatland. *Rev. Mod. Phys.*, 83:837–849, Aug 2011.

[2] H. Brody. Graphene. *Nature*, 483(7389):S29–S29, 2012.

[3] Tsuneya Ando, Alan B. Fowler, and Frank Stern. Electronic properties of two-dimensional systems. *Rev. Mod. Phys.*, 54:437–672, Apr 1982.

[4] E.Y. Andrei. *Two-dimensional electron systems on helium and other cryogenic substrates*, volume 19. Kluwer Academic Pub, 1997.

[5] M.F. Crommie, C.P. Lutz, and D.M. Eigler. Confinement of electrons to quantum corrals on a metal surface. *Science*, 262(5131):218, 1993.

[6] OE Dial, RC Ashoori, LN Pfeiffer, and KW West. High-resolution spectroscopy of two-dimensional electron systems. *Nature*, 448(7150):176–179, 2007.

[7] M. Stone. *Quantum Hall Effect*. World Scientific Pub Co Inc, 1992.

[8] R.E. Prange, S.M. Girvin, ME Cage, K. von Klitzing, D. Thouless, A. Pruisken, R. Laughlin, A. Chang, and FM Haldane. *The quantum Hall effect*. New York, 1987.

[9] T. Chakraborty and P. Pietiläinen. *The quantum Hall effects: integral and fractional*. Springer-verlag, 1995.

[10] A. H. Castro Neto, F. Guinea, N. M. R. Peres, K. S. Novoselov, and A. K. Geim. The electronic properties of graphene. *Rev. Mod. Phys.*, 81(1):109–162, Jan 2009.

[11] DSL Abergel, V. Apalkov, J. Berashevich, K. Ziegler, and T. Chakraborty. Properties of graphene: a theoretical perspective. *Advances in Physics*, 59(4):261–482, 2010.

[12] P. R. Wallace. The band theory of graphite. *Phys. Rev.*, 71:622–634, May 1947.

[13] R. Saito, G. Dresselhaus, M.S. Dresselhaus, et al. *Physical properties of carbon nanotubes*, volume 35. World Scientific, 1998.

[14] S. Reich, J. Maultzsch, C. Thomsen, and P. Ordejón. Tight-binding description of graphene. *Phys. Rev. B*, 66:035412, Jul 2002.

[15] MI Katsnelson, KS Novoselov, and AK Geim. Chiral tunnelling and the klein paradox in graphene. *Nature Physics*, 2(9):620–625, 2006.

[16] G. Grosso and G.P. Parravicini. *Solid State Physics*. Academic Press, 2000.

[17] L. Van Hove. The occurrence of singularities in the elastic frequency distribution of a crystal. *Physical Review*, 89(6):1189, 1953.

[18] M. O. Goerbig. Electronic properties of graphene in a strong magnetic field. *Rev. Mod. Phys.*, 83:1193–1243, Nov 2011.

[19] G.W. Semenoff. Condensed-matter simulation of a three-dimensional anomaly. *Physical Review Letters*, 53(26):2449–2452, 1984.

[20] II Rabi. Das freie elektron im homogenen magnetfeld nach der diracschen theorie. *Zeitschrift für Physik A Hadrons and Nuclei*, 49(7):507–511, 1928.

[21] A.K. Geim and K.S. Novoselov. The rise of graphene. *Nature materials*, 6(3):183–191, 2007.

[22] M.I. Katsnelson. Graphene: carbon in two dimensions. *Materials today*, 10(1):20–27, 2007.

[23] A.K. Geim. Graphene: status and prospects. *science*, 324(5934):1530–1534, 2009.

[24] A.K. Geim and P. Kim. Carbon wonderland. *Scientific American*, 298(4):90–97, 2008.

[25] N. Savage. Materials science: Super carbon. *Nature*, 483(7389):S30–S31, 2012.

[26] J.S. Bunch, A.M. Van Der Zande, S.S. Verbridge, I.W. Frank, D.M. Tanenbaum, J.M. Parpia, H.G. Craighead, and P.L. McEuen. Electromechanical resonators from graphene sheets. *Science*, 315(5811):490–493, 2007.

[27] C. Lee, X. Wei, J.W. Kysar, and J. Hone. Measurement of the elastic properties and intrinsic strength of monolayer graphene. *Science*, 321(5887):385–388, 2008.

[28] J.S. Bunch, S.S. Verbridge, J.S. Alden, A.M. Van Der Zande, J.M. Parpia, H.G. Craighead, and P.L. McEuen. Impermeable atomic membranes from graphene sheets. *Nano letters*, 8(8):2458–2462, 2008.

[29] A.A. Balandin, S. Ghosh, W. Bao, I. Calizo, D. Teweldebrhan, F. Miao, and C.N. Lau. Superior thermal conductivity of single-layer graphene. *Nano Letters*, 8(3):902–907, 2008.

[30] Z. Sun, Z. Yan, J. Yao, E. Beitler, Y. Zhu, and J.M. Tour. Growth of graphene from solid carbon sources. *Nature*, 468(7323):549–552, 2010.

[31] F. Schedin, AK Geim, SV Morozov, EW Hill, P. Blake, MI Katsnelson, and KS Novoselov. Detection of individual gas molecules adsorbed on graphene. *Nature materials*, 6(9):652–655, 2007.

[32] G. Li, A. Luican, and E.Y. Andrei. Self-navigation of a scanning tunneling microscope tip toward a micron-sized graphene sample. *Review of Scientific Instruments*, 82:073701, 2011.

[33] Adina Luican-Mayer and Eva Y. Andrei. Probing dirac fermions in graphene by scanning tunneling probes. *preprint*, 2012.

[34] G. Binnig, H. Rohrer, Ch. Gerber, and E. Weibel. Surface studies by scanning tunneling microscopy. *Phys. Rev. Lett.*, 49(1):57–61, Jul 1982.

[35] J. Tersoff and D. R. Hamann. Theory and application for the scanning tunneling microscope. *Phys. Rev. Lett.*, 50:1998–2001, Jun 1983.

[36] J. Tersoff and D. R. Hamann. Theory of the scanning tunneling microscope. *Phys. Rev. B*, 31(2):805–813, Jan 1985.

[37] C.J. Chen. *Introduction to scanning tunneling microscopy*, volume 4. Oxford University Press, USA, 1993.

[38] J.A. Stroscio and W.J. Kaiser. *Scanning tunneling microscopy*, volume 27. Academic Pr, 1993.

[39] R. Wiesendanger. *Scanning probe microscopy and spectroscopy: methods and applications*. Cambridge Univ Pr, 1994.

[40] S. H. Pan, E. W. Hudson, and J. C. Davis. [sup 3]he refrigerator based very low temperature scanning tunneling microscope. *Review of Scientific Instruments*, 70(2):1459–1463, 1999.

[41] CR Dean, AF Young, I. Meric, C. Lee, L. Wang, S. Sorgenfrei, K. Watanabe, T. Taniguchi, P. Kim, KL Shepard, et al. Boron nitride substrates for high-quality graphene electronics. *Nature nanotechnology*, 5(10):722–726, 2010.

[42] Ke Xu, Peigen Cao, and James R. Heath. Scanning tunneling microscopy characterization of the electrical properties of wrinkles in exfoliated graphene monolayers. *Nano Letters*, 9(12):4446–4451, 2009. PMID: 19852488.

[43] E. Stolyarova, K.T. Rim, S. Ryu, J. Maultzsch, P. Kim, L.E. Brus, T.F. Heinz, M.S. Hybertsen, and G.W. Flynn. High-resolution scanning tunneling microscopy imaging of mesoscopic graphene sheets on an insulating surface. *Proceedings of the National Academy of Sciences*, 104(22):9209, 2007.

[44] V. Geringer, M. Liebmann, T. Echtermeyer, S. Runte, M. Schmidt, R. Rückamp, M. C. Lemme, and M. Morgenstern. Intrinsic and extrinsic corrugation of monolayer graphene deposited on sio_2. *Phys. Rev. Lett.*, 102(7):076102, Feb 2009.

[45] M. Ishigami, JH Chen, WG Cullen, MS Fuhrer, and ED Williams. Atomic structure of graphene on SiO2. *Nano Lett*, 7(6):1643–1648, 2007.

[46] Adina Luican, Guohong Li, and Eva Y. Andrei. Quantized landau level spectrum and its density dependence in graphene. *Phys. Rev. B*, 83:041405, Jan 2011.

[47] KS Novoselov, D. Jiang, F. Schedin, TJ Booth, VV Khotkevich, SV Morozov, and AK Geim. Two-dimensional atomic crystals. *Proceedings of the National Academy of Sciences of the United States of America*, 102(30):10451, 2005.

[48] Y. Zhang, Y.W. Tan, H.L. Stormer, and P. Kim. Experimental observation of the quantum Hall effect and Berry's phase in graphene. *Nature*, 438(7065):201–204, 2005.

[49] J. Martin, N. Akerman, G. Ulbricht, T. Lohmann, JH Smet, K. Von Klitzing, and A. Yacoby. Observation of electron–hole puddles in graphene using a scanning single-electron transistor. *Nature Physics*, 4(2):144–148, 2007.

[50] Y. Zhang, V.W. Brar, C. Girit, A. Zettl, and M.F. Crommie. Origin of spatial charge inhomogeneity in graphene. *Nature Physics*, 5(10):722–726, 2009.

[51] JH Chen, C. Jang, MS Fuhrer, ED Williams, and M. Ishigami. Charged impurity scattering in graphene. *Arxiv preprint arXiv:0708.2408*, 2007.

[52] CR Dean, AF Young, P. Cadden-Zimansky, L. Wang, H. Ren, K. Watanabe, T. Taniguchi, P. Kim, J. Hone, and KL Shepard. Multicomponent fractional quantum hall effect in graphene. *Arxiv preprint arXiv:1010.1179*, 2010.

[53] C.H. Lui, L. Liu, K.F. Mak, G.W. Flynn, and T.F. Heinz. Ultraflat graphene. *Nature*, 462(7271):339–341, 2009.

[54] S. Hattendorf, A. Georgi, V. Geringer, M. Liebmann, and M. Morgenstern. Graphene on mica probed by scanning tunneling microscopy: networks of aba and abc stacked graphene and corrugation of the monolayer. *Arxiv preprint arXiv:1207.5427*, 2012.

[55] A. Luican, G. Li, and E.Y. Andrei. Scanning tunneling microscopy and spectroscopy of graphene layers on graphite. *Solid State Communications*, 149(27-28):1151–1156, 2009.

[56] P. Neugebauer, M. Orlita, C. Faugeras, A.L. Barra, and M. Potemski. How perfect can graphene be? *Physical review letters*, 103(13):136403, 2009.

[57] C. Berger, Z. Song, T. Li, X. Li, A.Y. Ogbazghi, R. Feng, Z. Dai, A.N. Marchenkov, E.H. Conrad, N. Phillip, et al. Ultrathin epitaxial graphite: 2d electron gas properties and a route toward graphene-based nanoelectronics. *The Journal of Physical Chemistry B*, 108(52):19912–19916, 2004.

[58] AJ Van Bommel, JE Crombeen, and A. Van Tooren. Leed and auger electron observations of the sic (0001) surface. *Surface Science*, 48(2):463–472, 1975.

[59] I. Forbeaux, J.-M. Themlin, and J.-M. Debever. Heteroepitaxial graphite on $6h - \mathrm{SiC}(0001)$: interface formation through conduction-band electronic structure. *Phys. Rev. B*, 58:16396–16406, Dec 1998.

[60] K.S. Kim, Y. Zhao, H. Jang, S.Y. Lee, J.M. Kim, K.S. Kim, J.H. Ahn, P. Kim, J.Y. Choi, and B.H. Hong. Large-scale pattern growth of graphene films for stretchable transparent electrodes. *Nature*, 457(7230):706–710, 2009.

[61] Xuesong Li, Weiwei Cai, Jinho An, Seyoung Kim, Junghyo Nah, Dongxing Yang, Richard Piner, Aruna Velamakanni, Inhwa Jung, Emanuel Tutuc, Sanjay K. Banerjee, Luigi Colombo, and Rodney S. Ruoff. Large-area synthesis of high-quality and uniform graphene films on copper foils. *Science*, 324(5932):1312–1314, 2009.

[62] A. Reina, X. Jia, J. Ho, D. Nezich, H. Son, V. Bulovic, M.S. Dresselhaus, and J. Kong. Large area, few-layer graphene films on arbitrary substrates by chemical vapor deposition. *Nano letters*, 9(1):30–35, 2008.

[63] Q. Yu, L.A. Jauregui, W. Wu, R. Colby, J. Tian, Z. Su, H. Cao, Z. Liu, D. Pandey, D. Wei, et al. Control and characterization of individual grains and grain boundaries in graphene grown by chemical vapour deposition. *Nature Materials*, 10(6):443–449, 2011.

[64] S. Marchini, S. Günther, and J. Wintterlin. Scanning tunneling microscopy of graphene on ru(0001). *Phys. Rev. B*, 76:075429, Aug 2007.

[65] P.W. Sutter, J.I. Flege, and E.A. Sutter. Epitaxial graphene on ruthenium. *Nature materials*, 7(5):406–411, 2008.

[66] Alpha T. N'Diaye, Sebastian Bleikamp, Peter J. Feibelman, and Thomas Michely. Two-dimensional ir cluster lattice on a graphene moiré on ir(111). *Phys. Rev. Lett.*, 97:215501, Nov 2006.

[67] Elena Loginova, Shu Nie, Konrad Thürmer, Norman C. Bartelt, and Kevin F. McCarty. Defects of graphene on ir(111): Rotational domains and ridges. *Phys. Rev. B*, 80:085430, Aug 2009.

[68] Peter Sutter, Jerzy T. Sadowski, and Eli Sutter. Graphene on pt(111): Growth and substrate interaction. *Phys. Rev. B*, 80:245411, Dec 2009.

[69] Guohong Li, Adina Luican, and Eva Y. Andrei. Scanning tunneling spectroscopy of graphene on graphite. *Phys. Rev. Lett.*, 102(17):176804, Apr 2009.

[70] A. Fasolino, JH Los, and MI Katsnelson. Intrinsic ripples in graphene. *Nature Materials*, 6(11):858–861, 2007.

[71] N.D. Mermin and H. Wagner. Absence of ferromagnetism or antiferromagnetism in one-or two-dimensional isotropic heisenberg models. *Physical Review Letters*, 17(22):1133–1136, 1966.

[72] MI Katsnelson and AK Geim. Electron scattering on microscopic corrugations in graphene. *Philosophical Transactions of the Royal Society A: Mathematical, Physical and Engineering Sciences*, 366(1863):195, 2008.

[73] J.C. Meyer, AK Geim, MI Katsnelson, KS Novoselov, TJ Booth, and S. Roth. The structure of suspended graphene sheets. *Arxiv preprint cond-mat/0701379*, 2007.

[74] J. Xue, J. Sanchez-Yamagishi, D. Bulmash, P. Jacquod, A. Deshpande, K. Watanabe, T. Taniguchi, P. Jarillo-Herrero, and B.J. LeRoy. Scanning tunnelling microscopy and spectroscopy of ultra-flat graphene on hexagonal boron nitride. *Nature Materials*, 2011.

[75] R. Decker, Y. Wang, V.W. Brar, W. Regan, H.Z. Tsai, Q. Wu, W. Gannett, A. Zettl, and M.F. Crommie. Local electronic properties of graphene on a bn substrate via scanning tunneling microscopy. *Nano Letters*, 2011.

[76] A. Deshpande, W. Bao, F. Miao, CN Lau, and BJ LeRoy. Spatially resolved spectroscopy of monolayer graphene on SiO_ {2}. *Physical Review B*, 79(20):205411, 2009.

[77] S. Jung, G.M. Rutter, N.N. Klimov, D.B. Newell, I. Calizo, A.R. Hight-Walker, N.B. Zhitenev, and J.A. Stroscio. Evolution of microscopic localization in graphene in a magnetic field from scattering resonances to quantum dots. *Nature Physics*, 2011.

[78] K. S. Novoselov, A. K. Geim, S. V. Morozov, D. Jiang, Y. Zhang, S. V. Dubonos, I. V. Grigorieva, and A. A. Firsov. Electric field effect in atomically thin carbon films. *Science*, 306(5696):666–669, 2004.

[79] V. Geringer, D. Subramaniam, AK Michel, B. Szafranek, D. Schall, A. Georgi, T. Mashoff, D. Neumaier, M. Liebmann, and M. Morgenstern. Electrical transport and low-temperature scanning tunneling microscopy of microsoldered graphene. *Applied Physics Letters*, 96:082114, 2010.

[80] Y. Zhang, V.W. Brar, F. Wang, C. Girit, Y. Yayon, M. Panlasigui, A. Zettl, and M.F. Crommie. Giant phonon-induced conductance in scanning tunnelling spectroscopy of gate-tunable graphene. *Nature Physics*, 4(8):627–630, 2008.

[81] ML Teague, AP Lai, J. Velasco, CR Hughes, AD Beyer, MW Bockrath, CN Lau, and N.C. Yeh. Evidence for strain-induced local conductance modulations in single-layer graphene on SiO2. *Nano letters*, 9(7):2542–2546, 2009.

[82] Liuyan Zhao, Rui He, Kwang Taeg Rim, Theanne Schiros, Keun Soo Kim, Hui Zhou, Christopher Gutirrez, S. P. Chockalingam, Carlos J. Arguello, Lucia Plov, Dennis Nordlund, Mark S. Hybertsen, David R. Reichman, Tony F. Heinz, Philip Kim, Aron Pinczuk, George W. Flynn, and Abhay N. Pasupathy. Visualizing individual nitrogen dopants in monolayer graphene. *Science*, 333(6045):999–1003, 2011.

[83] G. M. Rutter, J. N. Crain, N. P. Guisinger, T. Li, P. N. First, and J. A. Stroscio. Scattering and interference in epitaxial graphene. *Science*, 317(5835):219–222, 2007.

[84] John H. Davies. *The physics of low-dimensional semiconductors: an introduction*. Cambridge Univ Pr, 1998.

[85] KS Novoselov, AK Geim, SV Morozov, D. Jiang, M.I.K.I.V. Grigorieva, SV Dubonos, and AA Firsov. Two-dimensional gas of massless Dirac fermions in graphene. *Nature*, 438(7065):197–200, 2005.

[86] K. v. Klitzing, G. Dorda, and M. Pepper. New method for high-accuracy determination of the fine-structure constant based on quantized hall resistance. *Phys. Rev. Lett.*, 45:494–497, Aug 1980.

[87] X. Du, I. Skachko, F. Duerr, A. Luican, and E.Y. Andrei. Fractional quantum Hall effect and insulating phase of Dirac electrons in graphene. *Nature*, 462(7270):192–195, 2009.

[88] K.I. Bolotin, F. Ghahari, M.D. Shulman, H.L. Stormer, and P. Kim. Observation of the fractional quantum Hall effect in graphene. *Nature*, 462(7270):196–199, 2009.

[89] D. C. Tsui, H. L. Stormer, and A. C. Gossard. Two-dimensional magnetotransport in the extreme quantum limit. *Phys. Rev. Lett.*, 48:1559–1562, May 1982.

[90] G. Li and E.Y. Andrei. Observation of Landau levels of Dirac fermions in graphite. *Nature Physics*, 3(9):623–627, 2007.

[91] T. Matsui, H. Kambara, Y. Niimi, K. Tagami, M. Tsukada, and Hiroshi Fukuyama. Sts observations of landau levels at graphite surfaces. *Phys. Rev. Lett.*, 94:226403, Jun 2005.

[92] K. Hashimoto, C. Sohrmann, J. Wiebe, T. Inaoka, F. Meier, Y. Hirayama, R. A. Römer, R. Wiesendanger, and M. Morgenstern. Quantum hall transition in real space: From localized to extended states. *Phys. Rev. Lett.*, 101:256802, Dec 2008.

[93] Z. Jiang, EA Henriksen, LC Tung, Y.J. Wang, ME Schwartz, MY Han, P. Kim, and HL Stormer. Infrared spectroscopy of Landau levels of graphene. *Physical review letters*, 98(19):197403, 2007.

[94] R. S. Deacon, K.-C. Chuang, R. J. Nicholas, K. S. Novoselov, and A. K. Geim. Cyclotron resonance study of the electron and hole velocity in graphene monolayers. *Phys. Rev. B*, 76:081406, Aug 2007.

[95] ML Sadowski, G. Martinez, M. Potemski, C. Berger, and WA De Heer. Landau level spectroscopy of ultrathin graphite layers. *Physical review letters*, 97(26):266405, 2006.

[96] J. Martin, N. Akerman, G. Ulbricht, T. Lohmann, K. Von Klitzing, JH Smet, and A. Yacoby. The nature of localization in graphene under quantum Hall conditions. *Nature Physics*, 5(9):669–674, 2009.

[97] L. A. Ponomarenko, R. Yang, R. V. Gorbachev, P. Blake, A. S. Mayorov, K. S. Novoselov, M. I. Katsnelson, and A. K. Geim. Density of states and zero landau level probed through capacitance of graphene. *Phys. Rev. Lett.*, 105(13):136801, Sep 2010.

[98] J.M. Pereira Jr, FM Peeters, and P. Vasilopoulos. Landau levels and oscillator strength in a biased bilayer of graphene. *Physical Review B*, 76(11):115419, 2007.

[99] D.L. Miller, K.D. Kubista, G.M. Rutter, M. Ruan, W.A. De Heer, et al. Observing the quantization of zero mass carriers in graphene. *Science*, 324(5929):924, 2009.

[100] N. Levy, S. A. Burke, K. L. Meaker, M. Panlasigui, A. Zettl, F. Guinea, A. H. Castro Neto, and M. F. Crommie. Strain-induced pseudomagnetic fields greater than 300 tesla in graphene nanobubbles. *Science*, 329(5991):544–547, 2010.

[101] P. Cheng, C. Song, T. Zhang, Y. Zhang, Y. Wang, J.F. Jia, J. Wang, Y. Wang, B.F. Zhu, X. Chen, et al. Landau quantization of topological surface states in bi2se3. *Physical review letters*, 105(7):76801, 2010.

[102] T. Hanaguri, K. Igarashi, M. Kawamura, H. Takagi, and T. Sasagawa. Momentum-resolved landau-level spectroscopy of dirac surface state in bi2se3. *Phys. Rev. B*, 82:081305, Aug 2010.

[103] H. Wang, Y. Wu, C. Cong, J. Shang, and T. Yu. Hysteresis of electronic transport in graphene transistors. *ACS nano*.

[104] X. Du, I. Skachko, A. Barker, and E.Y. Andrei. Approaching ballistic transport in suspended graphene. *Nature Nanotechnology*, 3(8):491–495, 2008.

[105] KI Bolotin, KJ Sikes, Z. Jiang, M. Klima, G. Fudenberg, J. Hone, P. Kim, and HL Stormer. Ultrahigh electron mobility in suspended graphene. *Solid State Communications*, 146(9-10):351–355, 2008.

[106] N.N. Klimov, S. Jung, S. Zhu, T. Li, C.A. Wright, S.D. Solares, D.B. Newell, N.B. Zhitenev, and J.A. Stroscio. Electromechanical properties of graphene drumheads. *science*, 336(6088):1557–1561, 2012.

[107] P. Balk. The si-sio2 system. *Materials science monographs*, 32, 1988.

[108] Y.B. Park and S.W. Rhee. Microstructure and interfacial states of silicon dioxide film grown by low temperature remote plasma enhanced chemical vapor deposition. *Journal of applied physics*, 86:1346, 1999.

[109] Y.B. Park and S.W. Rhee. Effects of chlorine addition on the silicon dioxide properties deposited with remote plasma enhanced chemical vapor deposition at low temperatures. *Applied physics letters*, 66:3477, 1995.

[110] JC Alonso, A. Ortiz, and C. Falcony. Low temperature sio2 films deposited by plasma enhanced techniques. *Vacuum*, 43(8):843–847, 1992.

[111] T. Ando and Y. Uemura. Theory of quantum transport in a two-dimensional electron system under magnetic fields. i. characteristics of level broadening and transport under strong fields. *Journal of the Physical Society of Japan*, 36:959, 1974.

[112] N. M. R. Peres, F. Guinea, and A. H. Castro Neto. Electronic properties of disordered two-dimensional carbon. *Phys. Rev. B*, 73:125411, Mar 2006.

[113] W. Zhu, Q. W. Shi, X. R. Wang, J. Chen, J. L. Yang, and J. G. Hou. Shape of disorder-broadened landau subbands in graphene. *Phys. Rev. Lett.*, 102:056803, Feb 2009.

[114] Cheol-Hwan Park, Feliciano Giustino, Marvin L. Cohen, and Steven G. Louie. Velocity renormalization and carrier lifetime in graphene from the electron-phonon interaction. *Phys. Rev. Lett.*, 99:086804, Aug 2007.

[115] J. González, F. Guinea, and MAH Vozmediano. Marginal-fermi-liquid behavior from two-dimensional coulomb interaction. *Physical Review B*, 59(4):2474–2477, 1999.

[116] Y.J. Song, A.F. Otte, Y. Kuk, Y. Hu, D.B. Torrance, et al. High-resolution tunnelling spectroscopy of a graphene quartet. *Nature*, 467(7312):185–189, 2010.

[117] T. Mashoff, M. Pratzer, V. Geringer, TJ Echtermeyer, MC Lemme, M. Liebmann, and M. Morgenstern. Bistability and oscillatory motion of natural nanomembranes appearing within monolayer graphene on silicon dioxide. *Nano letters*, 10(2):461–465, 2010.

[118] J. Gonzalez, F. Guinea, and MAH Vozmediano. Marginal-Fermi-liquid behavior from two-dimensional Coulomb interaction. *Physical Review B*, 59(4):2474–2477, 1999.

[119] M. Polini, R. Asgari, Y. Barlas, T. Pereg-Barnea, and AH MacDonald. Graphene: A pseudochiral Fermi liquid. *Solid State Communications*, 143(1-2):58–62, 2007.

[120] DC Elias, RV Gorbachev, AS Mayorov, SV Morozov, AA Zhukov, P. Blake, KS Novoselov, AK Geim, and F. Guinea. Dirac cones reshaped by interaction effects in suspended graphene. *Arxiv preprint arXiv:1104.1396*, 2011.

[121] OE Dial, RC Ashoori, LN Pfeiffer, and KW West. Anomalous structure in the single particle spectrum of the fractional quantum hall effect. *Nature*, 464(7288):566–570, 2010.

[122] Edward McCann. Asymmetry gap in the electronic band structure of bilayer graphene. *Phys. Rev. B*, 74:161403, Oct 2006.

[123] F. Guinea, A. H. Castro Neto, and N. M. R. Peres. Electronic states and landau levels in graphene stacks. *Phys. Rev. B*, 73:245426, Jun 2006.

[124] Y. Zhang, T.T. Tang, C. Girit, Z. Hao, M.C. Martin, A. Zettl, M.F. Crommie, Y.R. Shen, and F. Wang. Direct observation of a widely tunable bandgap in bilayer graphene. *Nature*, 459(7248):820–823, 2009.

[125] R. T. Weitz, M. T. Allen, B. E. Feldman, J. Martin, and A. Yacoby. Broken-symmetry states in doubly gated suspended bilayer graphene. *Science*, 330(6005):812–816, 2010.

[126] A. S. Mayorov, D. C. Elias, M. Mucha-Kruczynski, R. V. Gorbachev, T. Tudorovskiy, A. Zhukov, S. V. Morozov, M. I. Katsnelson, V. I. Falko, A. K. Geim, and K. S. Novoselov. Interaction-driven spectrum reconstruction in bilayer graphene. *Science*, 333(6044):860–863, 2011.

[127] B.E. Feldman, J. Martin, and A. Yacoby. Broken-symmetry states and divergent resistance in suspended bilayer graphene. *Nature Physics*, 5(12):889–893, 2009.

[128] A. Deshpande, W. Bao, Z. Zhao, C.N. Lau, and BJ LeRoy. Mapping the dirac point in gated bilayer graphene. *Applied Physics Letters*, 95:243502, 2009.

[129] G.M. Rutter, S. Jung, N.N. Klimov, D.B. Newell, N.B. Zhitenev, and J.A. Stroscio. Microscopic polarization in bilayer graphene. *Nature Physics*, 2011.

[130] Javier D. Sanchez-Yamagishi, Thiti Taychatanapat, Kenji Watanabe, Takashi Taniguchi, Amir Yacoby, and Pablo Jarillo-Herrero. Quantum hall effect, screening, and layer-polarized insulating states in twisted bilayer graphene. *Phys. Rev. Lett.*, 108:076601, Feb 2012.

[131] Dong Su Lee, Christian Riedl, Thomas Beringer, A. H. Castro Neto, Klaus von Klitzing, Ulrich Starke, and Jurgen H. Smet. Quantum hall effect in twisted bilayer graphene. *Phys. Rev. Lett.*, 107:216602, Nov 2011.

[132] Babak Fallahazad, Yufeng Hao, Kayoung Lee, Seyoung Kim, R. S. Ruoff, and E. Tutuc. Quantum hall effect in bernal stacked and twisted bilayer graphene grown on cu by chemical vapor deposition. *Phys. Rev. B*, 85:201408, May 2012.

[133] HA Mizes and JS Foster. Long-range electronic perturbations caused by defects using scanning tunneling microscopy. *Science*, 244(4904):559, 1989.

[134] D. V. Khveshchenko. Coulomb-interacting dirac fermions in disordered graphene. *Phys. Rev. B*, 74:161402, Oct 2006.

[135] Vitor M. Pereira, Johan Nilsson, and A. H. Castro Neto. Coulomb impurity problem in graphene. *Phys. Rev. Lett.*, 99:166802, Oct 2007.

[136] J.H. Chen, C. Jang, S. Adam, MS Fuhrer, ED Williams, and M. Ishigami. Charged-impurity scattering in graphene. *Nature Physics*, 4(5):377–381, 2008.

[137] T. O. Wehling, S. Yuan, A. I. Lichtenstein, A. K. Geim, and M. I. Katsnelson. Resonant scattering by realistic impurities in graphene. *Phys. Rev. Lett.*, 105:056802, Jul 2010.

[138] Cristina Bena. Local density of states in the presence of impurity scattering in graphene at high magnetic field. *Phys. Rev. B*, 81:045409, Jan 2010.

[139] S. Das Sarma, Shaffique Adam, E. H. Hwang, and Enrico Rossi. Electronic transport in two-dimensional graphene. *Rev. Mod. Phys.*, 83:407–470, May 2011.

[140] P. K. Pyatkovskiy and V. P. Gusynin. Dynamical polarization of graphene in a magnetic field. *Phys. Rev. B*, 83:075422, Feb 2011.

[141] Yuhui Zhang, Yafis Barlas, and Kun Yang. Coulomb impurity under magnetic field in graphene: A semiclassical approach. *Phys. Rev. B*, 85:165423, Apr 2012.

[142] Markus Morgenstern. Scanning tunneling microscopy and spectroscopy of graphene on insulating substrates. *Physica Status Solidi B*, 248(11):2423–2434, 2011.

[143] Eva Y Andrei, Guohong Li, and Xu Du. Electronic properties of graphene: a perspective from scanning tunneling microscopy and magnetotransport. *Reports on Progress in Physics*, 75(5):056501, 2012.

[144] D. Yoshioka. Local density of states around an impurity in a strong magnetic field. i. a two-dimensional system with parabolic dispersion. *J. Phys. Soc. Jpn.*, 76:024718, 2007.

[145] Y. Niimi, H. Kambara, and Hiroshi Fukuyama. Localized distributions of quasi-two-dimensional electronic states near defects artificially created at graphite surfaces in magnetic fields. *Phys. Rev. Lett.*, 102:026803, Jan 2009.

[146] D.L. Miller, K.D. Kubista, G.M. Rutter, M. Ruan, W.A. de Heer, M. Kindermann, et al. Real-space mapping of magnetically quantized graphene states. *Nature Physics*, 6(10):811–817, 2010.

[147] Y. Okada, W. Zhou, C. Dhital, D. Walkup, Y. Ran, Z. Wang, S.D. Wilson, and V. Madhavan. Visualizing landau levels of dirac electrons in a one dimensional potential. *Arxiv preprint arXiv:1205.6230*, 2012.

[148] Adina Luican-Mayer, Maxim Kharitonov, Chih-Pin Lu Guohong Li, Alem-Mar Goncalves, and Eva Y. Andrei. Observation of quantized impurity states and their screening in the quantum hall regime in graphene. *preprint*, 2012.

[149] A. Luican, Guohong Li, A. Reina, J. Kong, R. R. Nair, K. S. Novoselov, A. K. Geim, and E. Y. Andrei. Single-layer behavior and its breakdown in twisted graphene layers. *Phys. Rev. Lett.*, 106:126802, Mar 2011.

[150] B. Trauzettel, D.V. Bulaev, D. Loss, and G. Burkard. Spin qubits in graphene quantum dots. *Nature Physics*, 3(3):192–196, 2007.

[151] A.V. Rozhkov, G. Giavaras, Yury P. Bliokh, Valentin Freilikher, and Franco Nori. Electronic properties of mesoscopic graphene structures: Charge confinement and control of spin and charge transport. *Physics Reports*, 503(23):77 – 114, 2011.

[152] J. Guttinger, C. Stampfer, S. Hellmuller, F. Molitor, T. Ihn, and K. Ensslin. Charge detection in graphene quantum dots. *Applied Physics Letters*, 93(21):212102–212102, 2008.

[153] C. Stampfer, E. Schurtenberger, F. Molitor, J. Guttinger, T. Ihn, and K. Ensslin. Tunable graphene single electron transistor. *Nano letters*, 8(8):2378–2383, 2008.

[154] LA Ponomarenko, F. Schedin, MI Katsnelson, R. Yang, EW Hill, KS Novoselov, and AK Geim. Chaotic dirac billiard in graphene quantum dots. *Science*, 320(5874):356–358, 2008.

[155] T. Ihn, J. Güttinger, F. Molitor, S. Schnez, E. Schurtenberger, A. Jacobsen, S. Hellmüller, T. Frey, S. Dröscher, C. Stampfer, et al. Graphene single-electron transistors. *Materials Today*, 13(3):44–50, 2010.

[156] V.M. Pereira and AH Castro Neto. Strain engineering of graphenes electronic structure. *Physical review letters*, 103(4):46801, 2009.

[157] F. Guinea, MI Katsnelson, and AK Geim. Energy gaps and a zero-field quantum hall effect in graphene by strain engineering. *Nature Physics*, 6(1):30–33, 2009.

[158] Edward McCann and Vladimir I. Fal'ko. Landau-level degeneracy and quantum hall effect in a graphite bilayer. *Phys. Rev. Lett.*, 96:086805, Mar 2006.

[159] T. Taychatanapat, K. Watanabe, T. Taniguchi, and P. Jarillo-Herrero. Quantum hall effect and landau-level crossing of dirac fermions in trilayer graphene. *Nature Physics*, 7(8):621–625, 2011.

[160] W. Bao, L. Jing, J. Velasco Jr, Y. Lee, G. Liu, D. Tran, B. Standley, M. Aykol, SB Cronin, D. Smirnov, et al. Stacking-dependent band gap and quantum transport in trilayer graphene. *Nature Physics*, 7(12):948–952, 2011.

[161] F. Guinea, A.H.C. Neto, and NMR Peres. Electronic states and landau levels in graphene stacks. *Physical Review B*, 73(24):245426, 2006.

[162] A.H. MacDonald and R. Bistritzer. Materials science: Graphene moire mystery solved? *Nature*, 474(7352):453–454, 2011.

[163] J. M. B. Lopes dos Santos, N. M. R. Peres, and A. H. Castro Neto. Graphene bilayer with a twist: Electronic structure. *Phys. Rev. Lett.*, 99:256802, Dec 2007.

[164] G. Li, A. Luican, J.M.B.L. Dos Santos, A.H.C. Neto, A. Reina, J. Kong, and EY Andrei. Observation of van hove singularities in twisted graphene layers. *Nature Physics*, 6(2):109–113, 2009.

[165] Zhao Y. Rong and Pieter Kuiper. Electronic effects in scanning tunneling microscopy: Moiré pattern on a graphite surface. *Phys. Rev. B*, 48:17427–17431, Dec 1993.

[166] J. Xhie, K. Sattler, M. Ge, and N. Venkateswaran. Giant and supergiant lattices on graphite. *Phys. Rev. B*, 47:15835–15841, Jun 1993.

[167] Katsuyoshi Kobayashi. Moiré pattern in scanning tunneling microscopy of monolayer graphite. *Phys. Rev. B*, 50:4749–4755, Aug 1994.

[168] W.T. Pong and C. Durkan. A review and outlook for an anomaly of scanning tunnelling microscopy (stm): superlattices on graphite. *Journal of Physics D: Applied Physics*, 38:R329, 2005.

[169] G. Trambly de Laissardie‘re, D. Mayou, and L. Magaud. Localization of dirac electrons in rotated graphene bilayers. *Nano Letters*, 10(3):804–808, 2010. PMID: 20121163.

[170] E. J. Mele. Commensuration and interlayer coherence in twisted bilayer graphene. *Phys. Rev. B*, 81:161405, Apr 2010.

[171] Rafi Bistritzer and Allan H. MacDonald. Moir bands in twisted double-layer graphene. *Proceedings of the National Academy of Sciences*, 108(30):12233–12237, 2011.

[172] S. Shallcross, S. Sharma, E. Kandelaki, and O. A. Pankratov. Electronic structure of turbostratic graphene. *Phys. Rev. B*, 81:165105, Apr 2010.

[173] S. Shallcross, S. Sharma, and O. A. Pankratov. Quantum interference at the twist boundary in graphene. *Phys. Rev. Lett.*, 101:056803, Aug 2008.

[174] Marcus Fleck, Andrzej M. Oleś, and Lars Hedin. Magnetic phases near the van hove singularity in *s*- and *d*-band hubbard models. *Phys. Rev. B*, 56:3159–3166, Aug 1997.

[175] J. González. Kohn-luttinger superconductivity in graphene. *Phys. Rev. B*, 78:205431, Nov 2008.

[176] T. M. Rice and G. K. Scott. New mechanism for a charge-density-wave instability. *Phys. Rev. Lett.*, 35:120–123, Jul 1975.

[177] R. de Gail, M. O. Goerbig, F. Guinea, G. Montambaux, and A. H. Castro Neto. Topologically protected zero modes in twisted bilayer graphene. *Phys. Rev. B*, 84:045436, Jul 2011.

[178] Pilkyung Moon and Mikito Koshino. Energy spectrum and quantum hall effect in twisted bilayer graphene. *Phys. Rev. B*, 85:195458, May 2012.

[179] Min-Young Choi, Young-Hwan Hyun, and Yoonbai Kim. Angle dependence of the landau level spectrum in twisted bilayer graphene. *Phys. Rev. B*, 84:195437, Nov 2011.

[180] M. Kindermann and E. J. Mele. Landau quantization in twisted bilayer graphene: The dirac comb. *Phys. Rev. B*, 84:161406, Oct 2011.

[181] J. Hicks, M. Sprinkle, K. Shepperd, F. Wang, A. Tejeda, A. Taleb-Ibrahimi, F. Bertran, P. Le Fèvre, W. A. de Heer, C. Berger, and E. H. Conrad. Symmetry breaking in commensurate graphene rotational stacking: Comparison of theory and experiment. *Phys. Rev. B*, 83:205403, May 2011.

[182] David L. Miller, Kevin D. Kubista, Gregory M. Rutter, Ming Ruan, Walt A. de Heer, Phillip N. First, and Joseph A. Stroscio. Structural analysis of multilayer graphene via atomic moiré interferometry. *Phys. Rev. B*, 81:125427, Mar 2010.

[183] P. Poncharal, A. Ayari, T. Michel, and J.-L. Sauvajol. Raman spectra of misoriented bilayer graphene. *Phys. Rev. B*, 78:113407, Sep 2008.

[184] Robin W. Havener, Houlong Zhuang, Lola Brown, Richard G. Hennig, and Jiwoong Park. Angle-resolved raman imaging of interlayer rotations and interactions in twisted bilayer graphene. *Nano Letters*, 12(6):3162–3167, 2012.

[185] Zhenhua Ni, Yingying Wang, Ting Yu, Yumeng You, and Zexiang Shen. Reduction of fermi velocity in folded graphene observed by resonance raman spectroscopy. *Phys. Rev. B*, 77:235403, Jun 2008.

[186] Kwanpyo Kim, Sinisa Coh, Liang Z. Tan, William Regan, Jong Min Yuk, Eric Chatterjee, M. F. Crommie, Marvin L. Cohen, Steven G. Louie, and A. Zettl. Raman spectroscopy study of rotated double-layer graphene: Misorientation-angle dependence of electronic structure. *Phys. Rev. Lett.*, 108:246103, Jun 2012.

[187] H. Schmidt, T. Lüdtke, P. Barthold, and R. J. Haug. Mobilities and scattering times in decoupled graphene monolayers. *Phys. Rev. B*, 81:121403, Mar 2010.

[188] C.R. Clemmer and T.P. Beebe Jr. Graphite: a mimic for dna and other biomolecules in scanning tunneling microscope studies. *Science*, 251(4994):640–642, 1991.

[189] WM Heckl and G. Binnig. Domain walls on graphite mimic dna. *Ultramicroscopy*, 42:1073–1078, 1992.

[190] C. Daulan, A. Derré, S. Flandrois, J. Roux, H. Saadaoui, et al. Stm observations at the atomic scale of a tilt grain sub-boundary on highly oriented pyrolytic graphite. *Journal de Physique I*, 5(9):1111–1117, 1995.

[191] TR Albrecht, HA Mizes, J. Nogami, S. Park, and CF Quate. Observation of tilt boundaries in graphite by scanning tunneling microscopy and associated multiple tip effects. *Applied physics letters*, 52(5):362–364, 1988.

[192] P. Simonis, C. Goffaux, PA Thiry, LP Biro, P. Lambin, and V. Meunier. Stm study of a grain boundary in graphite. *Surface science*, 511(1):319–322, 2002.

[193] O.V. Yazyev. Polycrystalline graphene: Atomic structure, energetics and transport properties. *Solid State Communications*, 2012.

[194] O.V. Yazyev and S.G. Louie. Electronic transport in polycrystalline graphene. *Nature materials*, 9(10):806–809, 2010.

[195] A. Mesaros, S. Papanikolaou, CFJ Flipse, D. Sadri, and J. Zaanen. Electronic states of graphene grain boundaries. *Physical Review B*, 82(20):205119, 2010.

[196] D. Gunlycke and C.T. White. Graphene valley filter using a line defect. *Physical Review Letters*, 106(13):136806, 2011.

[197] S. Malola, H. Häkkinen, and P. Koskinen. Structural, chemical, and dynamical trends in graphene grain boundaries. *Physical Review B*, 81(16):165447, 2010.

[198] J. Červenka and C. F. J. Flipse. Structural and electronic properties of grain boundaries in graphite: Planes of periodically distributed point defects. *Phys. Rev. B*, 79:195429, May 2009.

[199] J. Červenka, MI Katsnelson, and CFJ Flipse. Room-temperature ferromagnetism in graphite driven by two-dimensional networks of point defects. *Nature Physics*, 5(11):840–844, 2009.

[200] J. Lahiri, Y. Lin, P. Bozkurt, I.I. Oleynik, and M. Batzill. An extended defect in graphene as a metallic wire. *Nature nanotechnology*, 5(5):326–329, 2010.

[201] K. Kim, Z. Lee, B.D. Malone, K.T. Chan, B. Alemán, W. Regan, W. Gannett, MF Crommie, M.L. Cohen, and A. Zettl. Multiply folded graphene. *Physical Review B*, 83(24):245433, 2011.

[202] P.Y. Huang, C.S. Ruiz-Vargas, A.M. van der Zande, W.S. Whitney, M.P. Levendorf, J.W. Kevek, S. Garg, J.S. Alden, C.J. Hustedt, Y. Zhu, et al. Grains and grain boundaries in single-layer graphene atomic patchwork quilts. *Nature*, 469(7330):389–392, 2011.

[203] J. An, E. Voelkl, J.W. Suk, X. Li, C.W. Magnuson, L. Fu, P. Tiemeijer, M. Bischoff, B. Freitag, E. Popova, et al. Domain (grain) boundaries and evidence of twinlike structures in chemically vapor deposited grown graphene. *ACS nano*, 5(4):2433, 2011.

[204] O.V. Yazyev. Magnetism in disordered graphene and irradiated graphite. *Physical review letters*, 101(3):37203, 2008.

[205] O.V. Yazyev. Emergence of magnetism in graphene materials and nanostructures. *Reports on Progress in Physics*, 73:056501, 2010.

[206] Adina Luican-Mayer, Guohong Li, Gabriel Autes, Oleg Yazyev, and Eva Y. Andrei. Localized states at grain boundaries in graphite. *preprint*, 2012.

[207] O.V. Yazyev and S.G. Louie. Topological defects in graphene: Dislocations and grain boundaries. *Physical Review B*, 81(19):195420, 2010.

[208] B. Wang, Y. Puzyrev, and S.T. Pantelides. Strain enhanced defect reactivity at grain boundaries in polycrystalline graphene. *Carbon*, 49(12):3983–3988, 2011.

[209] PO Lehtinen, AS Foster, Y. Ma, AV Krasheninnikov, and RM Nieminen. Irradiation-induced magnetism in graphite: a density functional study. *Physical review letters*, 93(18):187202, 2004.

[210] O.V. Yazyev and L. Helm. Defect-induced magnetism in graphene. *Physical Review B*, 75(12):125408, 2007.

[211] Y.H. Kim, J. Choi, KJ Chang, and D. Tománek. Defective fullerenes and nanotubes as molecular magnets: An ab initio study. *Physical Review B*, 68(12):125420, 2003.

[212] X. Jia, M. Hofmann, V. Meunier, B.G. Sumpter, J. Campos-Delgado, J.M. Romo-Herrera, H. Son, Y.P. Hsieh, A. Reina, J. Kong, et al. Controlled formation of sharp zigzag and armchair edges in graphitic nanoribbons. *Science*, 323(5922):1701, 2009.